Developing Asymmetries in AGB Stars: Occurrence, Morphology and Polarization of Circumstellar Masers

Developing Asymmetries in AGB Stars: Occurrence, Morphology and Polarization of Circumstellar Masers

PROEFSCHRIFT

ter verkrijging van
de graad van Doctor aan de Universiteit Leiden,
op gezag van de Rector Magnificus prof. mr. P. F. van der Heijden,
volgens besluit van het College voor Promoties
te verdedigen op woensdag 26 oktober 2011
klokke 13.45 uur

door

Nikta Amiri
geboren te Mashhad, Iran
in 1983

Promotiecommissie

Contents

Contents

Introduction

1

1.1   Outline

The aim of the research presented in this thesis is to probe the asymmetries in the circumstellar envelopes of Asymptotic Giant Branch (AGB) and post-AGB stars which will likely evolve into asymmetric Planetary Nebulae (PNe) at the end of their life. I present the observations and modeling of astrophysical masers which occur in the outflows from evolved stars. The masers provide excellent tracers of the outflows at various distances from the central AGB stars. In this introduction I explain the AGB phase which is the last stage of stellar evolution. This is followed by an overview of the asymmetric PNe problem. Then I discuss the circumstellar masers which occur in the outflow from evolved stars. Next, I will explain how we use masers as astronomical tools to probe the magnetic fields and morphology of the outflow in the CSEs. Finally, I will present the main goals and the outline of the chapters of the thesis.

1.2   Asymptotic Giant Branch Phase

After a star leaves the main sequence, it evolves through several evolutionary stages, including the red giant branch, the horizontal branch and the AGB phase (Fig. 1.1). The last phase of the evolution for low to intermediate mass stars (1-8 $M_\odot$) is the AGB phase. In this stage, the star is left with a core of carbon and oxygen and two burning layers of Hydrogen and Helium surround the core. More than 90% of the stars including our Sun will evolve into the AGB phase. These stars will become >3000 times more luminous than our Sun. An extensive review of AGB stars is given by Habing (1996).

In the AGB phase the stars lose significant amounts of their mass to the interstellar medium in the form of stellar winds. The outflows form the circumstellar envelopes (CSEs) around the AGB stars (Fig. 1.2). In regular AGB stars, the CSEs are generally thought to be spherically symmetric. However, departures from spherical symmetry likely occurs in the late AGB or early post-AGB stage. AGB stars are known to be variable at visual and infrared wavelengths. Mira variables have periods of 100 days or more.

For a long time, OH/IR stars were thought to represent more evolved AGB stars (e.g. Bedijn 1987), although there is evidence that OH/IR stars come from a distinct higher mass population (e.g. Whitelock et al. 1994, Chen et al. 2001). The CSEs of these stars are denser and larger than those of Mira variables. The average expansion velocity in the CSEs is in the range 5-15 km s^{-1}. The mass loss rate ranges from 10^{-8} to 10^{-4} M$_\odot$/yr. Such a high mass loss rate could result in the situation that the central AGB star is highly obscured and therefore the emission radiated from the photosphere at infrared and optical wavelengths will be absorbed by the dust and re-emitted at longer wavelengths. The dust shell constitutes about one percent of the total mass of the CSEs. However, it likely plays a major role in driving the wind through the radiation pressure effect. In this scenario, the dust particles absorb the radiation and gain momentum. The particles transfer the momentum to the gas by friction, which governs the mass loss.

After the mass loss stops in the AGB phase, the star will evolve into the post-AGB and probably PNe phases.
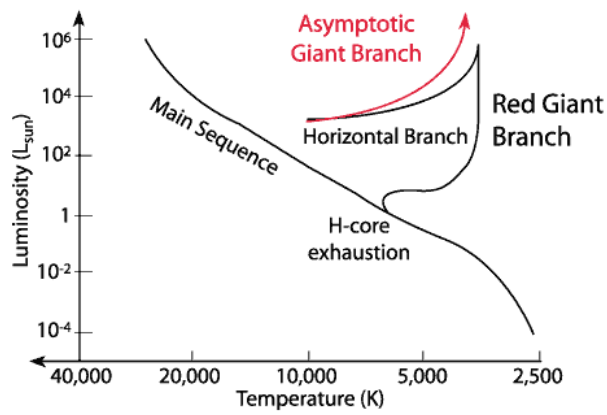
Figure 1.1 – Hertzsprung-Russell Diagram (HRD) which shows the evolutionary track of stars.
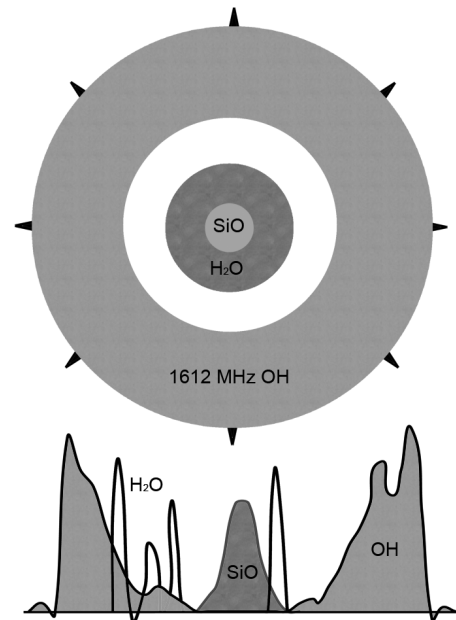
Figure 1.2 – A schematic view of the CSE of a typical oxygen-rich AGB star. SiO masers occur close to the photosphere and show single peak profiles. H_2O masers occur at intermediate distances and exhibit irregular profiles. The 1612 MHz OH masers emit at the outer part of the CSE and display double peak profiles, which corresponds to the front and back side of the shell. Asphericity likely occurs in the late AGB or early post-AGB stage. Credit: Lor*á*nt Sjouwerman.

3

1.2.1 Planetary Nebulae

After the nuclear burning stops in the H and He burning shells, the central AGB star becomes a hot white dwarf with a surface temperature of ~30,000 K or more. The remnant CSE ejected previously in the AGB phase becomes a PN where the ultraviolet radiation from the central white dwarf ionizes the gas. The majority of the observed PNe exhibit a range of complex morphologies (e.g. Manchado et al. 2000, Balick et al. 1987), whereas their progenitor AGB stars are generally observed to be spherically symmetric (e.g. Bowers et al. 1983). Fig. 1.3 shows the observed shapes of PNe obtained by the Hubble Space Telescopes (HST). PNe are thought to form as a result of the interaction between the fast post-AGB wind (~1000 km s^{-1}) and an asymmetric dense and cool AGB wind (e.g. Kwok et al. 1978, Balick et al. 1987). HST imaging of a sample of proto-PNe candidates has shown a wide variety of morphologies including bipolar structures (Sahai et al. 2007). Collimated outflows which operate in the early proto-PNe stage have been proposed as responsible agents for the formation of bipolar PNe (Sahai & Trauger 1998). The mechanisms for producing fast and collimated outflows could result from the presence of a binary companion (e.g. Morris 1987). Alternatively, theoretical models by García-Segura et al. (2005) show that magnetic fields could have an important role in collimating the jets.

The a-spherical shapes of PNe could indicate that departure from spherical symmetry occurs during the transition from the AGB phase to the PNe stage, the so called proto-PNe phase. Therefore, probing asymmetries even in the earlier stage represented by the CSEs of AGB stars is essential to understand the origin of complex morphologies observed in PNe. The CSEs of AGB stars harbor molecular and atomic species as well as the dust.

1.3 Circumstellar Envelopes

The main tracers of the properties of the CSEs are the atomic and molecular lines ranging from the cm to μm wavelength (radio to infrared), as well as sub-mm to infrared continuum and spectral features of the dust. In particular the CSEs harbor various *maser* species at different distances from the central stars:

1.3.1 What is a Maser?

Maser stands for microwave amplification by stimulated emission of radiation. The essential property of a maser transition is the population inversion, where the population of the upper energy level is higher than the lower level population. A Laser is the equivalent of a Maser, which occurs at higher frequencies in the ultraviolet or visible region of the electromagnetic spectrum.

The fundamental physical mechanism for maser emission is stimulated emission which was first introduced by Einstein in 1917. Fig. 1.4 shows the principle of maser emission schematically. Masers occur naturally in space and different molecular species can exhibit maser emission. This implies that there are regions in space, in which the physical

4
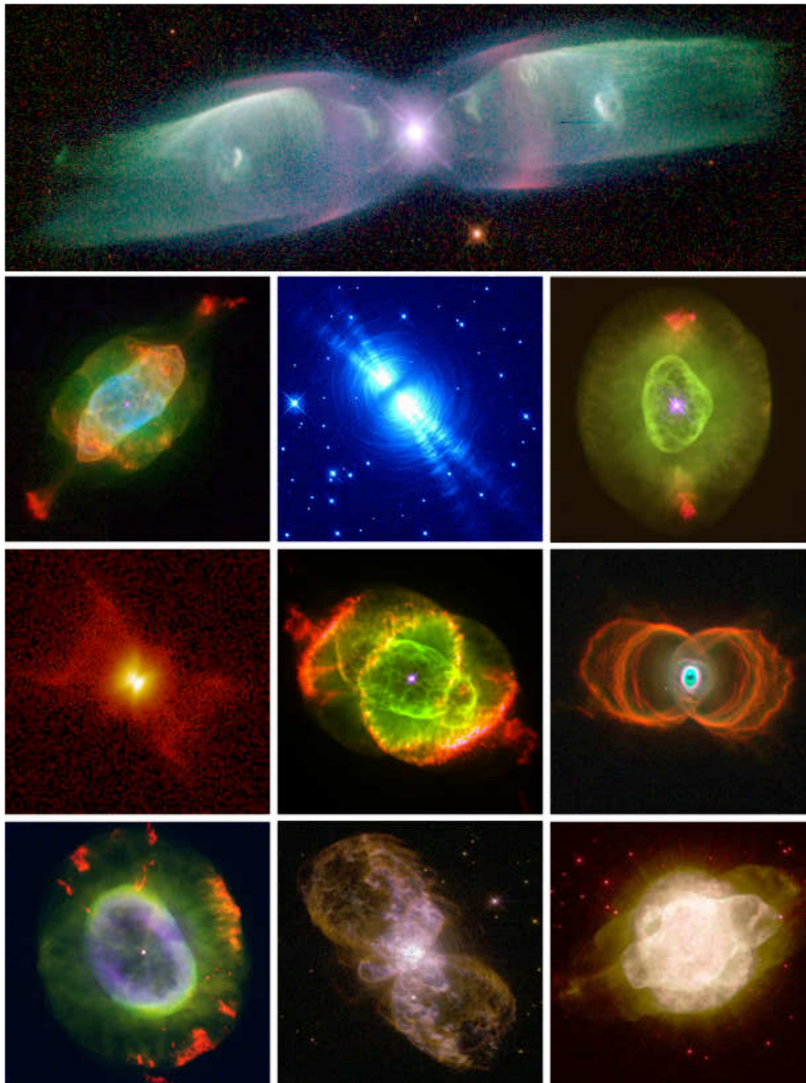
Figure 1.3 – A montage of Planetary Nebulae observed with the Hubble Space Telescope. Credit: NASA-Bruce Balick.
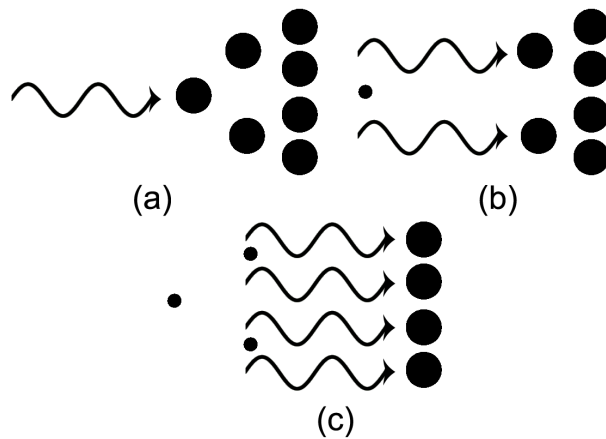
Figure 1.4 – Principle of maser emission: In all frames, the large circles show molecules excited to the upper energy state by a pump. The small circles indicate the molecules in the low energy state. 'a' panel: the molecule in the excited energy state is stimulated by a photon of wavelength λ. 'b' panel: The molecule absorbs the photon and re-emits two photons instead to return to the low energy state. These two photons hit the next two excited molecules, which results in 4 photons (panel 'c'). This process continues and as the radiation propagates through the medium, the maser amplifies the radiation exponentially at wavelength λ, as long as it is unsaturated.

conditions are such that deviations from local thermodynamic equilibrium (LTE) are common. For the population inversion to occur, a pumping mechanism is required. Typical pumping mechanisms for astronomical masers include infrared radiation or collision with other molecules. The other necessary condition for masers is velocity coherence along the amplification path. This implies that the radiation is not amplified if the velocity gradient along the amplification path is higher than the thermal line width.

In the CSEs of oxygen-rich AGB stars, three maser species are common: SiO, H_2O and OH masers. The SiO masers occur in the near circumstellar environment in a region between the stellar photosphere and the dust formation zone. The H_2O and OH masers are found progressively at further distances. Fig. 1.2 displays a schematic view of the locations and spectra of maser species in the CSEs. Below, we describe the properties of each maser species. A detailed description of the masers is presented by Elitzur (1992).

1.3.1.1 OH Masers

The OH masers occur at the outer part of the CSEs at distances between 100-10000 AU from the central AGB star. The typical brightness temperature of the masers is in the range $10^8 - 10^{10}$ K. The masers are predominantly observed in the rotational ground level which has the highest population. The ground level transition is split into 2×2 levels by Λ-doubling and hyperfine interaction (Fig. 1.5, Wilson et al. 1990). The masers are

observed at both satellite line (1612 MHz) as well as the main line (1667 and 1665 MHz) transitions. The pumping mechanism for the 1612 MHz transition is known to be due to the infrared dust radiation at 35μ and 53μ. However, the pumping of the main line transitions is more complex.

As shown in Fig. 1.2, the OH masers are emitted from the outer part of oxygen-rich CSEs, in a region where the photodissociation of the H_2O molecules produces OH. At these distances the gas has reached the terminal velocity and therefore the velocity coherent path length is longest along the radial direction. The observed properties of the main line transitions are somewhat different from the satellite lines, which could imply a different physical mechanism and location of the masers in the CSEs. The 1612 MHz OH masers exhibit a double peak profile separated by 20-50 km s^{-1}. This characteristic profile can be explained by an expanding shell where there is no radial acceleration. The blue- and red-shifted peaks correspond to the emission from the front and back side of the shell. The expansion velocity is half the velocity separation between the two peaks and the middle point between the two peaks corresponds to the stellar velocity.

1.3.1.2 H_2O Masers

The $(6_{16} - 5_{23})$ H_2O maser transition occurs at 22.23508 GHz. The occurrence of H_2O masers is common in the CSEs of evolved stars. The observed brightness temperature of the masers is in the range $10^{11} - 10^{12}$ K. The pumping mechanism for the masers is thought to stem from collisions with other molecules.

The H_2O masers occur at intermediate distances from the central stars at distances between 5-100 AU from the photosphere. This is a region which experiences significant radial acceleration. Unlike the double peak profile commonly observed for the 1612 MHz OH masers, the H_2O masers do not show regular spectral patterns. In Mira variables the masers usually show emission close to the stellar velocity due to tangential beaming from rapidly accelerating winds (e.g. Chapman & Cohen 1985). However, in higher mass loss OH/IR stars the masers usually exhibit double peak profiles. This could indicate that the masers occur somewhat at further distances from the central star where the masers are mostly radially amplified (e.g. Engels & Lewis 1996).

1.3.1.3 SiO Masers

SiO masers occur in a region between the stellar photosphere and the dust formation zone at distances of 5-10 AU from the central AGB star. Therefore, the masers are excellent tracers of the kinematics and dynamics in regions close to the central star. The SiO molecule exhibits a range of maser spectral profiles; vibrational energy levels up to v=3 and rotational transitions as high as J=8-7 are reported for the masers (e.g. Jewell et al. 1987, Cernicharo et al. 1993, Humphreys et al. 1997). In particular the v=1, J=1→0 and v=1, J=2→1 transitions are known to be more prevalent in the CSEs.

The masers show complex profile structures which spread over a velocity range of ~10-15 km s^{-1} around the stellar velocity. The observed profiles of the masers indicate significant variability in profile shape and brightness temperature. The variability of the
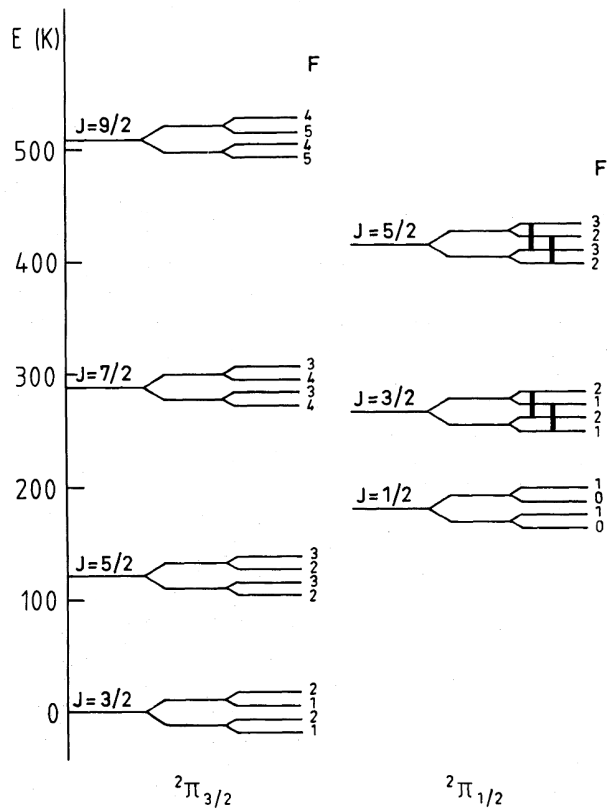
Figure 1.5 – The rotational levels of the OH molecule within 500 K of the ground state (Wilson et al. 1990). The Λ doubling and hyperfine splitting cause each rotational energy level to split into four groups of lines.

masers is thought to be related to the pulsation of the central AGB star. The typical brightness temperature of the masers is in the range 10^9-10^{10} K. The masers are confined in compact, high brightness spots and Very Long Baseline Interferometry observations around Mira variables reveal ring shape morphologies (Cotton et al. 2008, 2006, Diamond et al. 1994).

1.4 Masers as Tools to Probe the Stellar Evolution

The circumstellar masers which occur in the CSEs of evolved stars are useful tracers of the outflow at various distances from the central AGB stars. The masers exhibit very high brightness temperatures ($\sim 10^9$ K or higher), providing spectacular targets for interferometry and in particular for Very Long Baseline Interferometry (VLBI) observations. In my research I used various interferometer arrays including the European VLBI Network (EVN), the Very Long Baseline Array (VLBA), the Expanded Very Large Array (E-VLA) and the UK Multi-Element Radio Linked Interferometer Network (MERLIN) to map the circumstellar masers up to 0.5 mas resolution. Additionally, we performed single dish observations of the circumstellar masers using the radio telescopes including the Effelsberg Telescope and the Green Bank Telescope (GBT). Below, I explain the main goals of performing these observations:

1.4.1 Morphology of the CSEs

Interferometric observations of the masers enable us to obtain the spatial distribution of the masers in different regions of the CSEs in AGB and post-AGB stars. This helps us to study the asymmetries that already start in the AGB/ post-AGB phase which will evolve into a-spherical PNe. Furthermore, high resolution maps of maser spots enable us to compare the maser emission mechanism in different classes of evolved stars including Mira variables and higher mass loss OH/IR stars and in particular to understand how the distribution of the masers changes as the stars evolve through the AGB phase.

In particular, a class of proto-PNe candidates have been discovered, which exhibit high velocity H_2O maser jets ($\sim$200 km s^{-1} or more), much larger than the OH maser velocity extent (Likkel et al. 1992). VLBI observations of the H_2O masers of the so-called water fountain sources have shown collimated H_2O maser outflows (e.g. Imai et al. 2002, Boboltz & Marvel 2005). The observed spatial distribution and spectral characteristics of this class of sources is not consistent with those of regular AGB stars. An archetype of this class of objects is W43A. Fig. 1.6 displays the elongated dust emission of this star at 12.8 μm obtained with the Very Large Telescope (VLT) spectrometer and imager for the mid–infrared (VISIR, Lagadec et al. 2011). Overlaid are the H_2O and OH maser features obtained from high resolution interferometric observations. The dust image is clearly elongated in the direction of the H_2O maser jet. This could indicate that during the post-AGB phase the jets carve out the CSEs and leave an imprint which manifests itself as asymmetric PNe at the later stage in the evolution. This implies that other regions of the CSEs of these objects (e.g. OH and SiO maser regions), may also show deviation

9
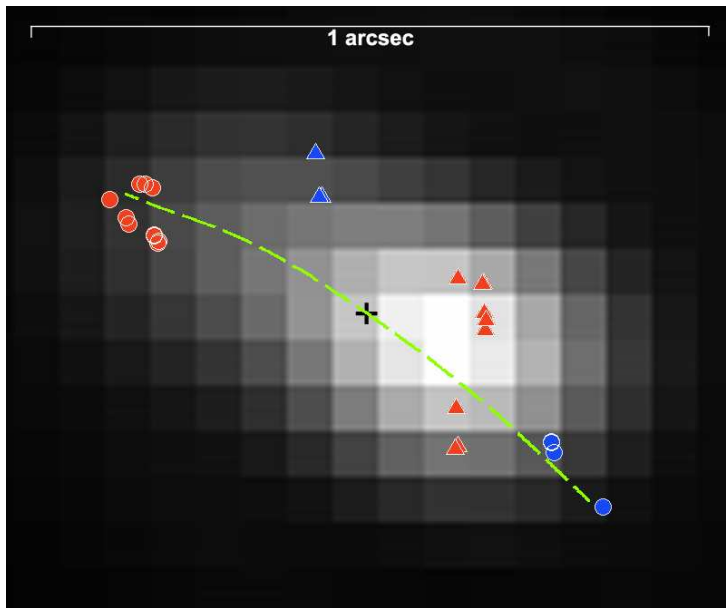
Figure 1.6 – The 12.8 μm dust image of W43A obtained with the Very Large Telescope (VLT) spectrometer and imager for the mid–infrared (VISIR, Lagadec et al. 2011). The overlaid circles and triangles show the H_2O and OH maser features of this star. The dashed line shows the direction of the precessing H_2O maser jet.

from spherical expansion. Therefore, studying the CSEs of this class of objects using high resolution observations of other maser species at different distances from the central AGB star is essential to understand the evolution of asymmetries as the star climbs the AGB phase.

1.4.2 Polarization of Masers

Polarimetric observations of masers are the best probes of magnetic fields in the CSEs, which enable us to understand the role of the magnetic fields in shaping the CSEs throughout the AGB evolution. The Zeeman splitting measurement of maser species is the most direct way to determine the magnetic field strength and morphology in the CSEs. In the presence of an external magnetic field, the energy levels of the maser transition are split into 2L+1 magnetic sub-levels, where L is the orbital angular momentum quantum number (Fig. 1.7). This implies that the ground state does not split in the magnetic field. The measured Zeeman splitting is related to the molecular structure, the strength of the magnetic field and the angle between the line of sight through the maser and the direction of the magnetic field. While single dish polarimetric observations can in principle only yield the overall field strength and morphology, polarimetric interferometry observations

10
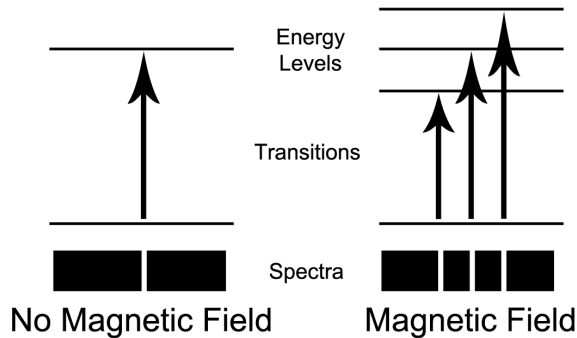
Figure 1.7 – Zeeman effect. In the presence of an external magnetic field, each spectral line is split into 2L+1 sub-levels, where L is the orbital angular momentum quantum number. Therefore, the ground state does not split in the magnetic field.

of circumstellar masers enable us to determine the field strength and morphology for the individual maser features.

Such circular polarization observations revealed significant field strengths in the CSEs. The observations of SiO masers have revealed a field strength of ~3.5 G for a sample of evolved stars (e.g. Herpin et al. 2006). The observed field for OH and H_2O masers is in the range 0.1-10 mG and 0.2-4 G, respectively (e.g Etoka & Diamond 2004, Vlemmings et al. 2002, 2005). Fig. 1.8 displays the magnetic field strength in different regions of the CSEs probed by maser polarization measurements. The figure shows that there is a clear relation between the field strength and the distance from the central star.

Additionally, the linear polarization measurements of the masers can probe the direction of the magnetic field projected on the plane of the sky. For regular masers in the CSEs, SiO masers typically exhibit high fractional linear polarization up to 100%. OH masers show polarization fractions up to tens of percent. However, H_2O maser observations do not indicate significant linear polarization.

The polarization analysis of the circumstellar masers is somewhat complex and alternative effects have been introduced which prohibit one to interpret the observed polarization as a measure of the magnetic field strength and morphology. The maser radiative transport can introduce preferred asymmetries not necessarily due to the magnetic effects. Therefore, this requires careful consideration of non-Zeeman mechanisms in order to reliably measure the magnetic fields. For OH and H_2O masers the non-Zeeman effects are not significant (Amiri et al. 2010, Vlemmings et al. 2005), while in the case of SiO masers it is not possible to distinguish between the Zeeman and non-Zeeman mechanisms.
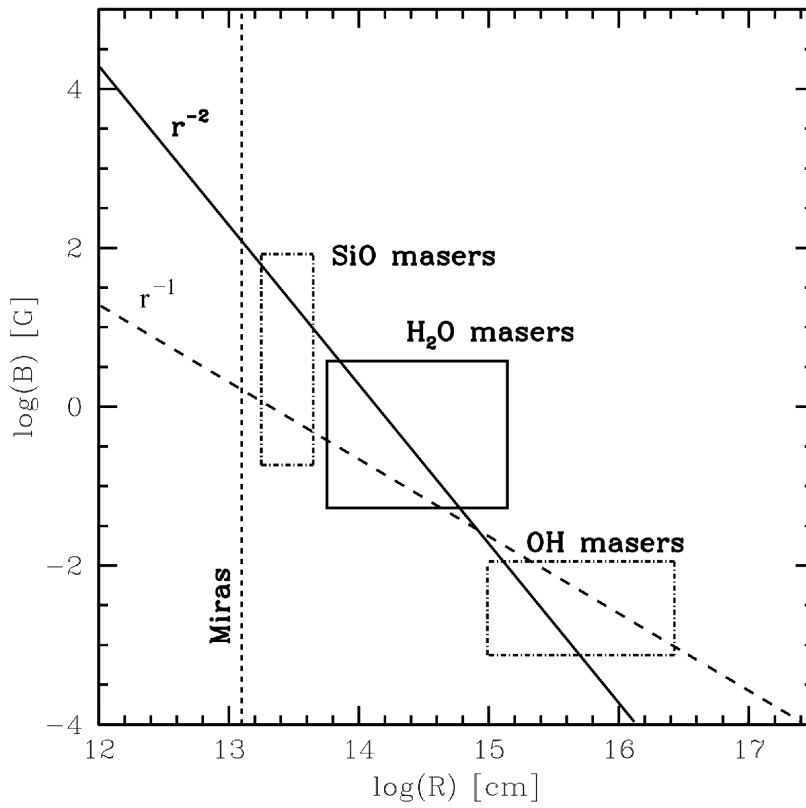
Figure 1.8 – The magnetic field strength (B) as a function of distance, R, from the center of the star. The boxes indicate the observed field strength obtained from polarimetric measurements of masers. The thick solid and dashed lines display an r^{-2} solar-type and r^{-1} toroidal magnetic field morphology. The vertical dashed line shows the stellar surface (Vlemmings et al. 2005).

1.4.3   Variability of the Masers

The circumstellar masers, in particular H_2O and SiO masers, are known to be variable in flux density and spectral profile. The lifetime of the individual maser features is a few months to years and the flux density may vary by as much as 2 orders of magnitude. The variability of the masers is thought to be related to the stellar pulsation as well as the changes in physical conditions in the environment in which masers occur. For example, H_2O masers are located in a region where shock waves driven by stellar pulsation are propagating through the H_2O maser zone (Rudnitskii & Chuprikov 1990, Shintani et al. 2008).

By single dish monitoring observations of the masers, we can study the variability statistics of the masers. This helps us to understand how rapidly the physical conditions in the CSEs change in time. Some masers show decrease in flux density and it is not clear however, if the masers that show deviation and in particular a decline in flux density, continuously lose flux until they fade away, or they rise up again.

1.5   This Thesis

The research in this thesis is focused on observations of masers around evolved stars. The observations include the use of radio interferometers as well as single dish telescopes. The aim of the the research is to address several key questions:

1. What is the role of the magnetic field in shaping the circumstellar environment of AGB stars?

2. Are strong magnetic fields common in different classes of AGB stars?

3. Is the occurrence of a-spherical morphologies common in the CSEs of evolved stars?

4. Are water fountain sources commonly found among post-AGB candidates?

In this thesis, Chapters 2, 3, 4 and 6 address questions 1, 2 and, while Chapter 5 focuses on question 4.

1.5.1   Outline of the Thesis & Main Results

- *Chapter 2&3*

  In chapters 2&3, we present the OH maser polarimetric observations of three water fountain sources (W43A, OH 12.8-0.9 and OH 37.1-0.8) with the UK MERLIN interferometer. The main goal of the observations is to understand whether large scale magnetic fields exist in the circumstellar environment of these stars.

  In Chapter 2, we report an average magnetic field of 100 μG measured for the OH maser region of W43A. Additionally, we present the polarimetric observations

of the H_2O maser jet of this star with the Green Bank Telescope. From the observations we measured a magnetic field of 30 mG for the red-shifted lobe of the H_2O maser jet. Interestingly, we found that the measured field for the OH masers of W43A is consistent with that extrapolated from the H_2O maser measurements. Therefore, our measurements show that the magnetic fields likely play an important role in shaping the entire circumstellar environment of this star.

In Chapter 3, for the first time, we present the spatial distribution of the OH maser features of OH 12.8-0.9 and OH 37.1-0.8. We found that the OH maser of both sources shows signs of a-spherical expansion. Additionally, we performed kinematical re-construction of the masers assuming a uniform distribution in the CSEs. The aim is to understand the distribution of the OH masers in water fountain sources with respect to the H_2O maser jet. In this class of objects, the jet-like outflows transform the spherically symmetric CSEs into a-spherical morphologies. We developed software which calculates the velocity coherent path length along the line of sight. Comparison of the OH maser observations (spectral profile and spatial distribution) with the reconstruction results shows that the OH masers of W43A are likely located in the equatorial region of the outflow, whereas for OH 12.8-0.9 the OH masers are likely located in a biconical outflow surrounding the H_2O maser jet. Additionally, we found that the H_2O maser jet of this star is located inside the OH maser shell. This could indicate that this source is still in the AGB phase and the jet has recently launched in this star.

- *Chapter 4*

  In Chapter 4, we present H_2O maser polarimetric observations of a sample of evolved stars. While previous measurements show significant field strength in Mira variables, it is not clear whether the occurrence of such strong magnetic fields is common in different classes of AGB stars. We observed three Mira variables and three higher mass loss OH/IR stars with the Green Bank Telescope. Even though the measured field strength is underestimated in single dish measurements due to the spectral blending, the observations measure the overall field strength in stars which are not strong enough for VLBI observations.

  From the observations we measured a magnetic field of 18.9 ± 3.8 mG for the H_2O maser region of the OH/IR star IRAS 19422+3506, and for the rest of the sources in the sample we only place upper limits on the magnetic field in the range 10-800 mG. Interestingly, we observe a striking double peak profile with emission close to the stellar velocity, which could indicate the presence of a bipolar outflow in this star, as previously observed in water fountain sources.

- *Chapter 5*

  In Chapter 5, we present multi-epoch observations of the H_2O masers of a sample of post-AGB candidates with the Effelsberg telescope. The aim of the observations was mainly to identify more water fountain sources to create a statistically significant sample of these important transition objects. We found six water fountain

candidates with striking double peak profiles which could hint that the masers are occurring in bipolar outflows. Follow up high resolution observations are essential to clarify this.

Additionally, multi-epoch observations enabled us to study the variability statistics and the change in the profile structure of the masers. We found that for a large number of sources the masers show significant deviation in flux density up to an order of magnitude. This could imply significant change in the physical conditions of the circumstellar environment. Furthermore, we found that ten sources which were detected in single dish observations 20 years ago (Engels & Lewis 1996), have now disappeared in our multi-epoch observations. This could imply a limited lifetime of the masers in the AGB phase (~60 years). Additionally, the statistical analysis indicate good correlation between the stellar pulsation and the H_2O maser variability.

Furthermore, we detected the H_2O masers of the supposedly dead OH/IR star IRAS 18455+0448. This object is considered as a prototype of a dead OH/IR star after the rapid disappearance of the 1612 MHz OH masers (Lewis et al. 2001). We performed follow up OH maser observations of this star at 1612, 1665, 1667 MHz. The observations showed that the 1612 MHz OH masers have not reappeared together with the H_2O masers, and importantly, that the 1665 and 1667 MHz OH masers have now also decreased dramatically in strength.

- *Chapter 6*

  In Chapter 6, we present the first SiO maser map of an OH/IR star at high angular resolution. We observed the v=1, J=1→0 transition of the SiO masers of OH 44.8-2.3 with the VLBA. The observations show a circular ring pattern at a radius of 5.4 AU from the photosphere, assuming a distance of 1.13 kpc previously measured using the phase lag method. Furthermore, we found that the SiO masers of this star are located at ~1.9 stellar radii which is similar to the location of SiO masers in Mira variables.

  The observations show that the SiO maser features of OH 44.8-2.3 show significant linear polarization up to 100%. While the linear polarization vectors are consistent with a dipole field morphology, we can not rule out other complex field morphologies including toroidal or solar type fields. Additionally, the circular polarization analysis shows a tentative detection of circular polarization at ~0.7% for the brightest maser feature in the modest spectral resolution data set. Due to the increased noise we can not confirm the detection in the high spectral resolution data set. The measured circular polarization corresponds to a magnetic field of 1.5±0.3 G.

  Additionally, we processed the 1612 MHz OH maser observations of OH 44.8-2.3 from the VLA archive. The OH masers exhibit an elongated morphology in the direction where there is a gap in the SiO maser emission. However, the OH masers occur at much larger distance (~1471 AU) from the photosphere than the SiO masers (~5.4 AU). Therefore, it is not clear whether both asymmetries are related. Assuming they are, this shows that there is a global mechanism which modifies the CSEs

15

on many scales. Furthermore, according to the polarization theory for SiO masers, the direction of the magnetic field is either parallel or perpendicular to the preferred direction of the outflow. This could indicate the possible role of the magnetic field in shaping the circumstellar environment of this object.

1.5.2 Conclusions and Outlook

The results presented in this thesis have shown that observations of astrophysical masers at high angular resolution provide a unique tool to study the morphology of the CSEs in different classes of AGB stars. This helped us to better understand the evolution of asymmetries in the CSEs throughout the AGB phase. Our observations have shown that asymmetries can occur in different classes of evolved stars. In particular, polarimetric observations of the masers provide the most direct method to determine the magnetic field strength and morphology at various distances from the central evolved stars. The polarization studies presented in this thesis show that magnetic fields could have a significant role in shaping the circumstellar environment.

Despite the significant progress in the field, a number of crucial questions remained to be answered. For example, the upgraded instruments (EVLA and eMERLIN) will provide the unique opportunity to obtain the position of maser features with respect to the central star more accurately. Together with polarization measurements, this helps us to determine the magnetic field strength and morphology of the CSEs throughout the AGB evolution.

Furthermore, the Atacama Large Millimeter Array (ALMA) will provide an unprecedented sensitivity and angular resolution to study the circumstellar environment of evolved stars in the sub-millimeter regime. Observations of the cold dust and in particular the polarimetric observations enable us to study the morphology and magnetic fields. Additionally, ALMA will open up new horizons to perform high resolution observations of high frequency maser lines for various maser species and in particular high angular resolution and polarimetric observations of HCN and SiS masers in carbon-rich AGB stars.

16

The magnetic field of the evolved star W43A

N. Amiri, W. H. T. Vlemmings, H. J. van Langevelde

Abstract

The majority of the observed planetary nebulae exhibit elliptical or bipolar structures. Recent observations have shown that asymmetries already start during the last stages of the AGB phase. Theoretical modeling has indicated that magnetically collimated jets may be responsible for the formation of the non-spherical planetary nebulae. Direct measurement of the magnetic field of evolved stars is possible using polarization observations of different maser species occurring in the circumstellar envelopes around these stars. The aim of this project is to measure the Zeeman splitting caused by the magnetic field in the OH and H_2O maser regions occurring in the circumstellar envelope and bipolar outflow of the evolved star W43A. We compare the magnetic field obtained in the OH maser region with the one measured in the H_2O maser jet. We used the UK Multi-Element Radio Linked Interferometer Network (MERLIN) to observe the polarization of the OH masers in the circumstellar envelope of W43A. Likewise, we used the Green Bank Telescope (GBT) observations to measure the magnetic field strength obtained previously in the H_2O maser jet. We report a measured magnetic field of approximately 100 μG in the OH maser region of the circumstellar envelope around W43A. The GBT observations reveal a magnetic field strength $B_{\parallel}$ of ∼30 mG changing sign across the H_2O masers at the tip of the red-shifted lobe of the bipolar outflow. We also find that the OH maser shell shows no sign of non-spherical expansion and that it probably has an expansion velocity that is typical for the shells of regular OH/IR stars. The GBT observations confirm that the magnetic field collimates the H_2O maser jet, while the OH maser observations show that a strong large scale magnetic field is present in the envelope surrounding the W43A central star. The magnetic field in the OH maser envelope is consistent with the one extrapolated from the H_2O measurements, confirming that magnetic fields play an important role in the entire circumstellar environment of W43A.

2.1 Introduction

At the end of their evolution, low mass stars undergo a period of high mass loss ($\dot{M} \propto 10^{-4} - 10^{-7}$ $M_\odot$/yr) that is important for enriching the interstellar medium with processed molecules. During this stage the star climbs up the asymptotic giant branch (AGB) in the Hertzsprung-Russell (H-R) diagram. AGB stars are generally observed to be spherically symmetric (Griffin 2004). However, planetary nebulae (PNe), supposedly formed out of the ejected outer envelopes of AGB stars, often show large departures from spherical symmetry. The origin and development of these asymmetries is not clearly understood. Observations of collimated jets and outflows of material in a number of PNe have been reported (e.g Sahai & Trauger 1998, Miranda et al. 2001, Alcolea et al. 2001). Sahai & Trauger (1998) propose that the precession of these jets is responsible for the observed asymmetries. These jets are likely formed when the star leaves the AGB and undergoes a transition to become a PN (e.g. Sahai & Trauger 1998, Imai et al. 2002, Miranda et al. 2001).

Magnetic fields can play an important role in shaping the circumstellar envelope (CSE) of evolved stars and can produce asymmetries during the transition from a spherical symmetric star into a non-spherical PN. They are also possible agents for collimating the jets around these sources (García-Segura et al. 2005). It is not clear how stars can maintain a significant magnetic field throughout the giant phases, as the drag of a large scale magnetic field would brake any stellar dynamo if no additional source of angular momentum is present (e.g. Soker 1998). However, theoretical models have shown that AGB stars can generate the magnetic field through a dynamo interaction between the fast rotating core and the slow rotating envelope (Blackman et al. 2001). Alternatively, the presence of a heavy planet or a binary companion as the additional source of angular momentum can maintain the magnetic field (e.g. Frank & Blackman 2004).

Polarization observations of different maser species in the CSE of these stars provide a unique tool for understanding the role of the magnetic field in the process of jet collimation. Strong magnetic fields have been observed throughout the entire CSE of these stars for different molecular species (e.g. Etoka & Diamond 2004, Vlemmings et al. 2006, Herpin et al. 2006 using OH, H_2O and SiO masers, respectively).

Likkel et al. (1992) introduced a separate class of post-AGB sources where H_2O maser velocity range exceeds that of OH maser in the CSE. High resolution H_2O maser observations trace highly collimated jets in the inner envelopes of these objects. These objects, the so-called water fountain sources, are thought to be in the transition stage to PNe. An archetype of this class is W43A, located at a distance of 2.6 kpc from the sun (Diamond et al. 1985), for which the H_2O masers have been shown to occur at the tips of a strongly collimated and precessing bipolar jet (Imai et al. 2002). Polarization observations of the H_2O masers of W43A reveal a strong magnetic field apparently collimating the jet (Vlemmings et al. 2006).

Here we describe observations of the Zeeman splitting of OH masers in the CSE and H_2O masers in the jet of W43A. Our aim is to investigate the magnetic field strength and morphology in the low density region of the CSE of this object, which is in transition to become a PN and confirm the magnetic field in the H_2O maser jet. The observations are described in §2.2 and the results of the observed spectra and the measured Zeeman splitting are presented in §2.3. The results are discussed in §2.4, where we investigate the observed Zeeman splitting and the significance of other non-Zeeman effects. This is followed by conclusions in §2.5.

19

2.2 Observations and Data Analysis

2.2.1 MERLIN Observations

We used the UK Multi-Element Radio Linked Interferometer Network (MERLIN) on 4 June 2007 to observe the 1612 MHz OH masers of the evolved star W43A. We included the Lovel telescope to achieve a higher sensitivity in this experiment. The longest baseline (217 km) resulted in a beam size of 0.3×0.2 arcsec. The observations were performed in full polarization spectral line mode with the maximum possible 256 spectral channels and a bandwidth of 0.25 MHz, covering a velocity width of 44 km/s, this gives a channel width of 0.2 km/s.

The observations of W43A were interleaved with observations of the phase reference source, 1904 + 013, in wide-band mode in order to obtain an optimal signal-to-noise-ratio. 3C286 was observed as primary flux calibrator and polarization angle calibrator. 3C84 was observed both in narrow band and wide band modes in order to apply band pass calibration and a phase offset correction. The full track of observations of W43A was 10 hours.

We performed the initial processing of the raw MERLIN data and conversion to FITS using the local d-programs at Jodrell Bank. The flux density of the amplitude calibrator, 3C84, was determined using the flux density of the primary flux calibrator, 3C286; we obtained a flux density of 18.94 Jy for 3C84. The rest of the calibration, editing and reduction of the data were performed in the Astronomical Image Processing Software Package (AIPS). Since the wide and narrow band data cover different frequency ranges and use different electronics, there may be a phase offset between the wide-band and narrow-band data; this offset was measured using the difference in phase solutions for 3C84 and was applied to correct the phase solutions from the phase reference source. The phase reference source, 1904+013, was used to obtain phase and amplitude solutions, which were applied to the target data set. The polarization calibration for leakage was done using 3C84, and the R and L phase offset corrections were performed on 3C286. Image cubes were created for stokes I, Q, U and V. The resulting noise in the emission free channels was 6.5 mJy/Beam. For the brightest feature we are limited to a dynamic range of ~650. A linearly polarized data cube was made using the stokes Q and U.

2.2.2 GBT Observations

The observations of the H_2O masers in the bipolar outflow of W43A were carried out at the NRAO[1] GBT at Oct 14 2006 as part of a project aimed at detecting additional water fountain sources. At 22.2 GHz the full-width at half maximum (FWHM) beamwidth of the GBT is $\sim 33''$, while the H_2O maser emission is located within $\sim 1''$. The GBT spectrometer was used with a bandwidth of 200 MHz and 16,384 spectral channels, providing a channel spacing of 0.164 km/s and a total velocity coverage of 2700 km/s, centered on $V_{LSR} = 34$ km/s. Furthermore, the data were taken with the dual-polarization receiver of the lower K-band using the total power nod observing mode. The two beams have a fixed separation of $178.8''$ in the azimuth direction and a cycle time of 2 minutes was sufficient to correct for atmospheric variations. As a result, one beam of the telescope was always pointing at the source while the other beam was used for baseline correction. As W43A

---

[1] The National Radio Astronomy Observatory (NRAO) is a facility of the National Science Foundation operated under cooperative agreement by Associated Universities, Inc.

was only observed as a test for the spectral line setup, the total on source observing time was just 6 minutes. Pointing and focus observations were done on J0958+655. This source, and 3C286, were also used as flux calibrator, providing flux calibration accurate to $\sim$ 10%. For data reduction we used the GBT IDL[2] software package. The total intensity spectrum of the W43A H_2O masers from these observations is shown in Fig. 2.1.

2.2.3 Determining Zeeman Splitting

The Zeeman effect causes a velocity shift between the left circular polarization (LCP) and the right circular polarization (RCP) spectra. For OH masers the separation is often larger than the line width, but for the H_2O molecule the splitting is small. The cross-correlation introduced by Modjaz et al. (2005) is an effective technique for measuring the Zeeman splitting without forming the stokes V spectrum. In this method, the RCP and LCP spectra are cross-correlated to determine the velocity offset. This method can even work for complex spectra, assuming that the velocity offset is the same over the spectrum; which means the magnetic field strength and direction is constant in the masing region. The sensitivity of this method is comparable to the S-curve method, where the stokes V spectrum is directly used for measuring the magnetic field (e.g. Vlemmings et al. 2001, Fiebig & Guesten 1989), but has the advantage of being less susceptible to calibration errors in the RCP and LCP absolute flux level determination.

2.3 Results

Fig. 2.1 shows the spectrum of the OH and H_2O maser regions of W43A obtained from MERLIN and GBT observations, respectively. For W43A, the velocity range for the OH (27 to 43 km/s) is much less than for H_2O (-53 to 126 km/s). The figure illustrates the water fountain nature of this source where H_2O masers occur outside the OH maser region in a much larger velocity range. The W43A OH masers have previously been observed by Bowers (1978) with a bandwidth of $\sim$ 400 km/s, who reported the OH emission to be confined to a similar velocity range.

The OH velocity profiles of the integrated flux of each channel in the I (total intensity), V (circular polarization) and P (linear polarization intensity) data are shown in Figure 2.2. The brightest peak is red-shifted and the blue-shifted peak has a much lower brightness; only $\sim$ 3% of the red-shifted brightness. There is little emission detected between the two peaks. Most of the emission in the total intensity profile was also detected in the linear and circular polarization spectra. For the circular and linear polarization profiles, the emission is dominated by the red-shifted peak. The peaks in the polarization intensity and circular polarization spectra are 10% linearly and 12% circularly polarized.

Using the AIPS task SAD, OH maser features with peaks higher than three times the rms noise in the emission free channel were identified and fitted with a Gaussian in the total intensity image cube; the results of which are shown in Table 2.1. The maser line width for each feature (Δv_l), was obtained by fitting a Gaussian distribution to the I spectra. The Zeeman splitting (Δv_z) is the velocity shift between the right and left circular polarizations for each maser feature obtained from the cross correlation method. B is the value of magnetic field measured by converting the velocity

---

[2] http://gbtidl.sourceforge.net
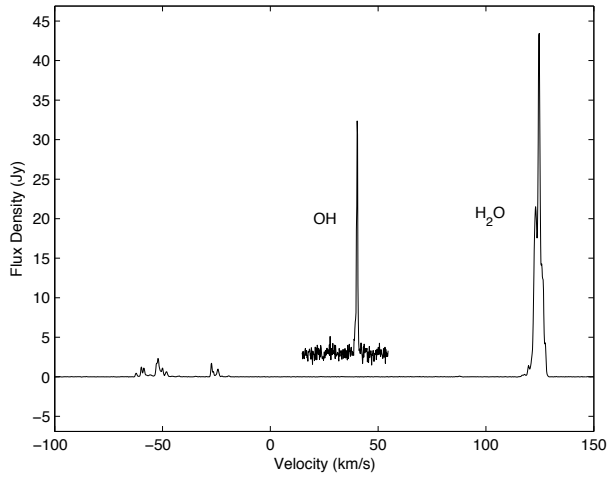
Figure 2.1 – The OH and H$_2$O maser spectra of W43A. The OH maser emission spectrum is shifted upward by 2 Jy for the purpose of illustration. The H$_2$O maser emission at 22 GHz is obtained from the GBT observations.
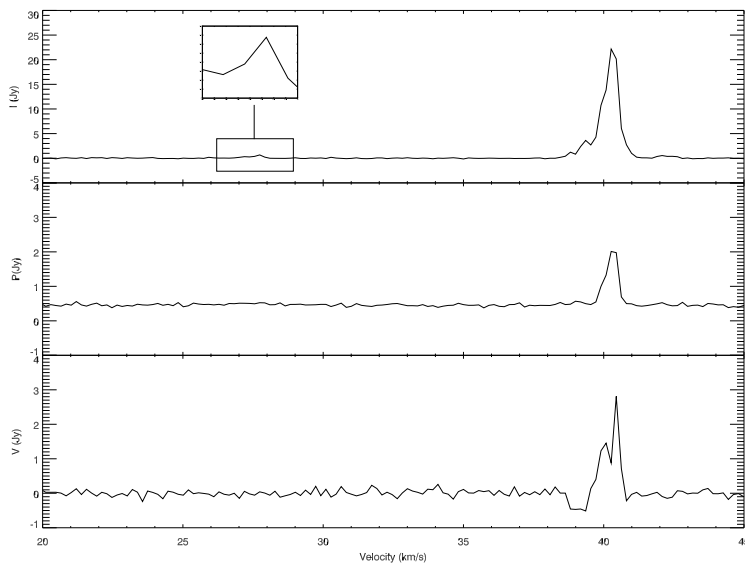
Figure 2.2 – The 1612 MHz spectra for total intensity (I), linear polarization (P) and circular polarization (V) data.
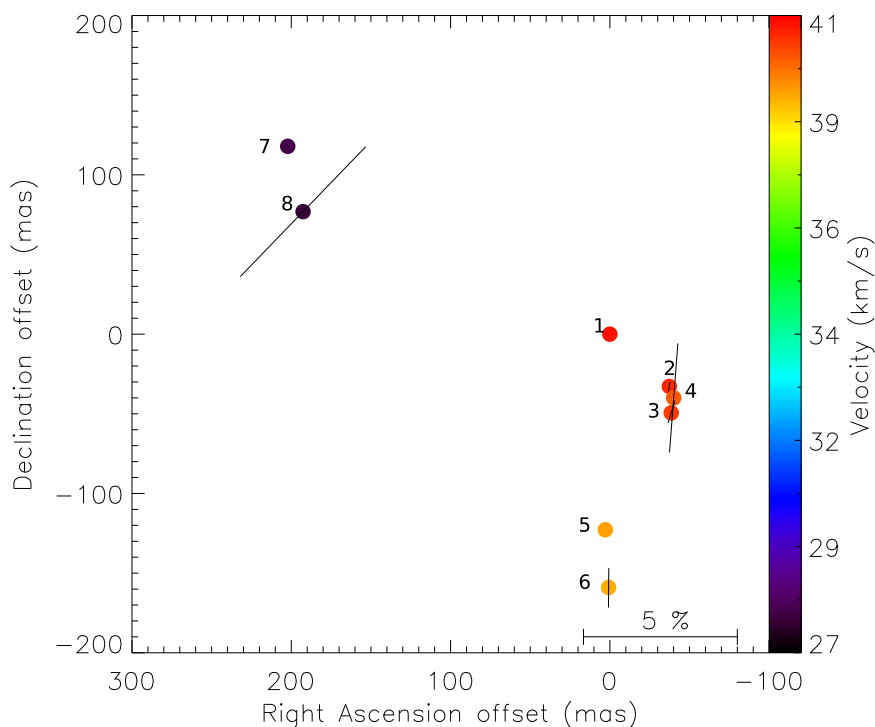
Figure 2.3 – The OH maser region of W43A. The offset positions are with respect to the maser reference feature. The maser spots are color-coded according to radial velocity. The vectors show the polarization angles, scaled logarithmically according to the linear polarization fraction m_l (Table 2.1).

splitting into the magnetic field strength using the Zeeman splitting coefficient of the OH maser line taken from the literature (236 km s^{-1} G^{-1}; Davies 1974). The errors in field determination and Zeeman splitting depend on the rms in the channels with bright emission. As the noise in channels with bright emission increases by a factor of ∼5, we have conservatively determined the errors by the increased rms in the channels with strong maser signal. The robustness of the errors determined from this against measurement uncertainties has been discussed in depth by Modjaz et al. (2005). The fractional linear (m_l) and circular (m_c) polarizations were obtained from the polarization intensity and circular polarization spectra and χ denotes the polarization angle.

Fig. 2.3 shows the OH maser spots (red-shifted and blue-shifted). The OH maser features detected for W43A are color coded according to their radial velocity (Table 2.1). The vectors indicate the polarization angle scaled logarithmically according to fractional linear polarization. The weighted average of the red-shifted vectors is ∼ -6.4° while the polarization angle for the blue-shifted feature is -44 °.

For illustration, following Fig. 2 of Imai et al. (2002), Fig. 2.4 shows the spatial distribution of the OH maser features of W43A together with H$_2$O maser positions (Vlemmings et al. 2006). Since no

Feature	RA 18 47	Dec -1 05	Peak Flux (Jy beam^{-1})	V_{rad} (km s^{-1})	Δv_l (km s^{-1})	Δv_z (m s^{-1})	B (μG)	m_l %	m_c %	χ deg
1	41.15933	11.4200	1.08 ± 0.01	41.0	0.59	11.9 ± 0.2	50±4	-	4.6 ± 0.9	-
2	41.15684	11.4500	2.18 ± 0.01	40.8	0.59	13.0 ± 0.2	55±4	1.1 ± 0.3	11.5 ± 0.4	-11±1
3	41.15676	11.4694	5.20 ± 0.01	40.6	0.59	13.9 ± 0.3	59±6	0.8 ± 0.2	5.0 ± 0.2	-17±7
4	41.15666	11.4600	21.04 ± 0.03	40.2	0.58	13.9 ± 0.2	59±4	3.13 ± 0.05	3.9 ± 0.1	-4.3±0.4
5	41.15952	11.5428	1.97 ± 0.01	39.5	0.62	20.1 ± 0.5	85±11	-	2.6 ± 0.5	-
6	41.15938	11.5790	3.33 ± 0.01	39.3	1.54	39.1 ± 1.1	166±24	1.5 ± 0.3	14.7 ± 0.3	-0.44±5.7
7	41.17281	11.3021	0.20 ± 0.01	27.9	0.43	-	-	-	-	-
8	41.17217	11.3431	0.60 ± 0.01	27.7	0.60	-	-	6.6 ± 1.32	-	-44±7

Table 2.1 – OH maser Results

24

accurate astrometry was available for H_2O masers, the maps were aligned on the respective centers of the maser distribution.

2.4 Discussion

2.4.1 OH maser polarization

The linear and circular polarization that we measure (as illustrated in Table 2.1), is consistent with marginal detections reported from earlier observations (Wilson & Barrett 1972). They found $4\pm2\%$ linear polarization for the masers at ~40.5 km/s, with a polarization angle of 10 ± 20 degrees. This is consistent with our finding of 0.8-3.2% linear polarization and an average polarization angle of ~-7 degrees for the masers around that velocity. Additionally, they measured a peak circular polarization of $30 \pm 10\%$ at ~ 39 km/s, decreasing to $10\pm5\%$ towards 40 km/s, which is consistent with our observations.

The Zeeman splitting for the OH is larger than that for H_2O. The split energy is determined by the following equation:

$$\Delta W = -\mu_0 \, g \, m_F \, B \quad\quad\quad (2.1)$$

For the OH molecule μ_0 is the Bohr magneton ($\mu_B = \frac{e\hbar}{2m_e c}$), and for the H_2O molecule μ_0 is the Nuclear magneton ($\mu_N = \frac{e\hbar}{2m_n c}$). As the Bohr magneton is almost 3 orders of magnitudes larger than the Nuclear magneton, the OH Zeeman splitting is correspondingly larger. However, the observed Zeeman splitting in the OH maser region of W43A is considerably still less than the maser line width by a factor of 50 (Table 2.1). We obtained an average magnetic field of 100 μ G in the OH maser region of W43A, using the cross correlation between the LCP and RCP spectra. The measured magnetic field is an order of magnitude lower than those often found in OH maser regions of evolved stars (e.g. Etoka & Diamond 2004, Bains et al. 2003). However, Zell & Fix (1991) reported magnetic field on micro-gauss level in the envelopes of a number of OH/IR stars. They also argue that there is convincing evidence that the smoothness of the line profile is consistent with models in which there are a few thousand individual emitting elements, with 5 or 10 individual elements within the spectral resolution. This implies that the spectral blending could decrease the observed polarization by as much as a factor of 2-3. Likewise, a comparison between high- and low spatial resolution circular polarization observations of other maser species also indicates that the blending of maser features typically decreases the magnetic field measured at low angular resolution by a factor of 2 (e.g. Sarma et al. 2001). Interferometric observations with higher spatial and spectral resolution are required to explore this effect further. Unfortunately, many of the masers may be resolved out due to their extended structure. Alternatively, OH polarization could originate from non-Zeeman effects. Although our measured magnetic field strength is similar to what is reported in OH/IR envelopes (Zell & Fix 1991), we investigate below to what level these effects could be contributing to our polarization measurements.

2.4.1.1 Non-Zeeman effects

A possible source of intensity dependent circular polarization occurs because of the rotation of the axis of symmetry for the molecular quantum states (Nedoluha & Watson 1994). This stems from the competition between the magnetic field (B) and the rate of stimulated emission (R). While

25

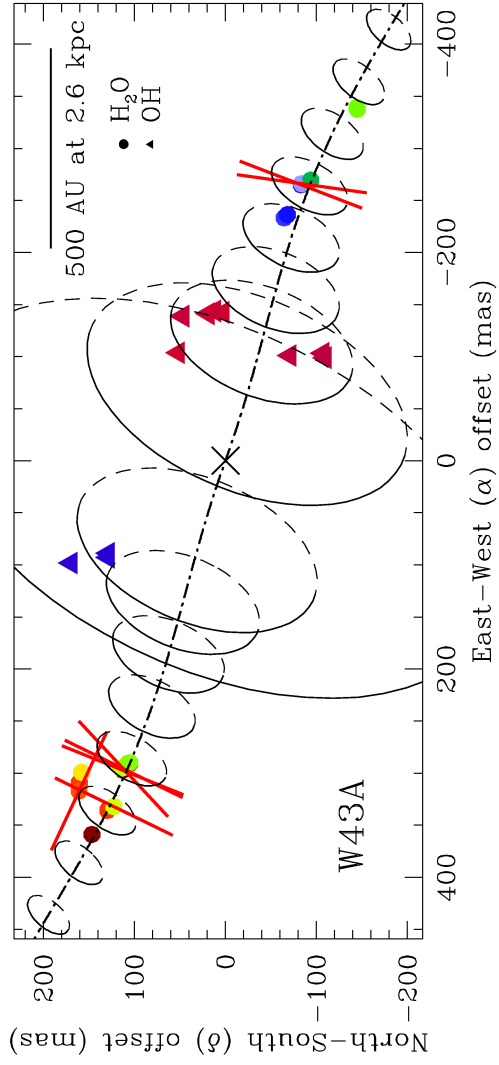**Figure 2.4** – Spatial distribution of OH and H$_2$O maser features. The offset positions are with respect to the maser reference feature. H$_2$O maser features are indicated by filled circles. OH maser features are shown as triangles. Red and blue colors show the red-shifted and blue-shifted features.

$g\Omega \geq R$, the magnetic field is the quantization axis. However, as the maser saturates and the rate of stimulated emission becomes larger, the molecule interacts more strongly with the stimulated emission and the axis of the symmetry of the molecule changes toward the direction of the maser beam. For the 1612 MHz OH maser the Zeeman splitting is 1.308 MHz G^{-1} (Davies 1974). For a magnetic field of B $\geq$ 10 μG, the Zeeman frequency shift becomes $g\Omega \geq$ 13.08 s^{-1}. The rate of stimulated emission is:

$$R \simeq A \, K \, T_b \, \Delta\Omega \,/\, 4 \, \pi \, h \, \nu. \qquad (2.2)$$

Here A is the Einstein coefficient for maser transition which is 1.3×10^{-11} s^{-1} for the 1612 MHz OH maser emission (Destombes et al. 1977). K and h are the Boltzmann and Planck constants respectively. T_b denotes the brightness temperature and for the 1612 MHz OH maser the maximum value is 10^{11} K (Reid & Moran 1981). $\Delta\Omega$ is the maser beaming angle. For a typical angle of 10^{-2} sr, the maser stimulated emission rate becomes 0.013 s^{-1}. Therefore, even for the largest value of R, the Zeeman frequency shift ($g\Omega$) is higher than the stimulated emission rate. The imposed change of the symmetry axis due to stimulated emission can thus not explain the circular polarization observed in the OH maser region of W43A.

Alternatively, the propagation of a strong linear polarization can create circular polarization if the magnetic field orientation changes along the maser propagation direction (Wiebe & Watson 1998). In the unsaturated regime with a fractional linear polarization up to 50%, the generated circular polarization is $\frac{m_l^2}{4}$ when the magnetic field rotates 1 rad along the maser path. In this case, the linear polarization fraction observed in the OH maser region of W43A ($m_l \sim$ 10 %), implies a generated circular polarization ($m_c \leq$ 0.25 %), which is much less than the measured circular polarization. Thus it is highly unlikely that the observed circular polarization is created in this way in the OH shell of W43A.

Thirdly, Fish & Reid (2006) discuss an observational effect which may generate velocity shift between RCP and LCP in the presence of a large linear polarization fraction, which could be falsely attributed to Zeeman splitting. They consider an extreme case where the emission is right elliptically polarized. The linearly polarized flux will only appear in the LCP receiver and the RCP receiver picks up all the emission including linear and circular polarizations. If the magnetic field orientation changes along the amplification path, the linear polarization component may be shifted in velocity with respect to the circular polarized component. This offset will manifest itself as a velocity shift between the RCP and LCP spectra. However, in the case of the OH emission region of W43A the RCP and LCP are at the same intensity level which means that both contain linear and circular polarizations. Therefore, this effect is unlikely to be at work.

Finally, to investigate the effect of instrumental polarization on the measured magnetic field, we imaged the unpolarized source, 3C84, in all polarization states and obtained the fractional linear and circular polarization which may account as leakage. 3C84 is regularly used as VLA / VLBA / MERLIN polarization calibrator, and is known to be unpolarized. Our results indicate a limit of 3% linear and 1% circular instrumental polarization. The relative low level of instrumental polarization could therefore not generate the observed circular polarization of 12% in the OH maser region of W43A. However, we can not formally rule out instrumental polarization as the cause of the linear polarization observed for any of the maser features other than feature 8.

2.4.2   H$_2$O maser polarization

The magnetic field on the red-shifted H$_2$O masers of W43A was detected using the cross-correlation method that was also used to measure the magnetic field in the OH maser region. To distinguish between separate spectral features, we specifically used the 'running' average method described in Vlemmings (2008) over 3 km/s intervals. We detect a magnetic field strength $B_{\parallel}$ changing sign from 31 ± 8 mG to -24 ± 7 mG across the red-shifted maser region (Fig. 2.5). This is approximately a factor of two lower than the magnetic field measured on blue-shifted masers using the VLBA (Vlemmings et al. 2006). However, blending of the maser features will decrease the magnetic field measured with low angular resolution and small differences of the pre-shock density, pre-shock magnetic field, or the shock velocity at blue and red-shifted tips of the jet will also affect magnetic field strength in the shock compressed H$_2$O maser region (Elitzur et al. 1989). The measurements are thus in good agreement with the previously published results. Additionally, the sign reversal seen across the maser provides additional support for the proposed jet collimation by a toroidal magnetic field as we would expect the magnetic field to change sign on either side of the jet.

2.4.3   The role of the magnetic field

Taking into account all the possible effects which may contribute to the velocity offset between RCP and LCP, we found no significant effect other than Zeeman splitting that could explain the observed circular polarization of the OH maser of W43A. We conclude that the observed circular polarization has a Zeeman origin and implies the OH maser region contains a large scale magnetic field of B $\sim$ 100 μG.

Vlemmings et al. (2006) observed the H$_2$O maser region of W43A at 22 GHz and measured a magnetic field of 85 ± 33 mG in the blue-shifted region. Our GBT observations reveal magnetic field strength $B_{\parallel}$ changing sign from 31 ± 8 mG to -24 ± 7 mG across the red-shifted H$_2$O masers. The magnetic field measured from the GBT observations confirms previous results by Vlemmings et al. (2006) that the magnetic field has a role in collimating the jet of W43A. H$_2$O masers occur in gas with a hydrogen number density of n $\approx 10^8 - 10^{10}$ cm^{-3} and OH is excited in gas with a hydrogen number density of $10^4 - 10^6$ cm^{-3} (Elitzur 1992). Two different scenarios for H$_2$O masers in W43A exist. One possibility is that the masers occur at the tips of the jet, when the jet has swept up enough material previously ejected from the stellar atmosphere. The jet occurs at the distance of 1000 AU from the central star traced by H$_2$O maser observations and the typical hydrogen density at the distance of 1000 AU is 10^5 cm^{-3} (Vlemmings et al. 2006). Therefore, the density must increase by three orders of magnitude at the tips of the jet so that the conditions become appropriate for H$_2$O maser excitation. Since the magnetic field strength depends on the density of the material (B $\propto n^k$, with magnetic field measurements in star forming regions implying k$\sim$0.5), the extrapolation of magnetic field outside the jet implies the value of B $\approx$ 0.9-2.6 mG in the OH maser region (Vlemmings et al. 2006). Alternatively, the masers can occur in a shock between the collimated jet and the dense material outside the CSE, similar to the H$_2$O masers occurring in star forming regions (Elitzur et al. 1989). Then, the pre-shock magnetic field extrapolated from the H$_2$O observations is 70 μG, comparable to what we now find for the OH maser region and implies a pre-shock density of 3×10^6 cm^{-3} (Vlemmings et al. 2006). Previously, it was thought that the H$_2$O masers are likely to occur in the compressed material at the tips of the jet because the pre-shock density is somewhat higher than the expected value at 1000 AU from the star in the circumstellar envelope (Vlemmings & Diamond 2006). However, our observations show that it is more likely that
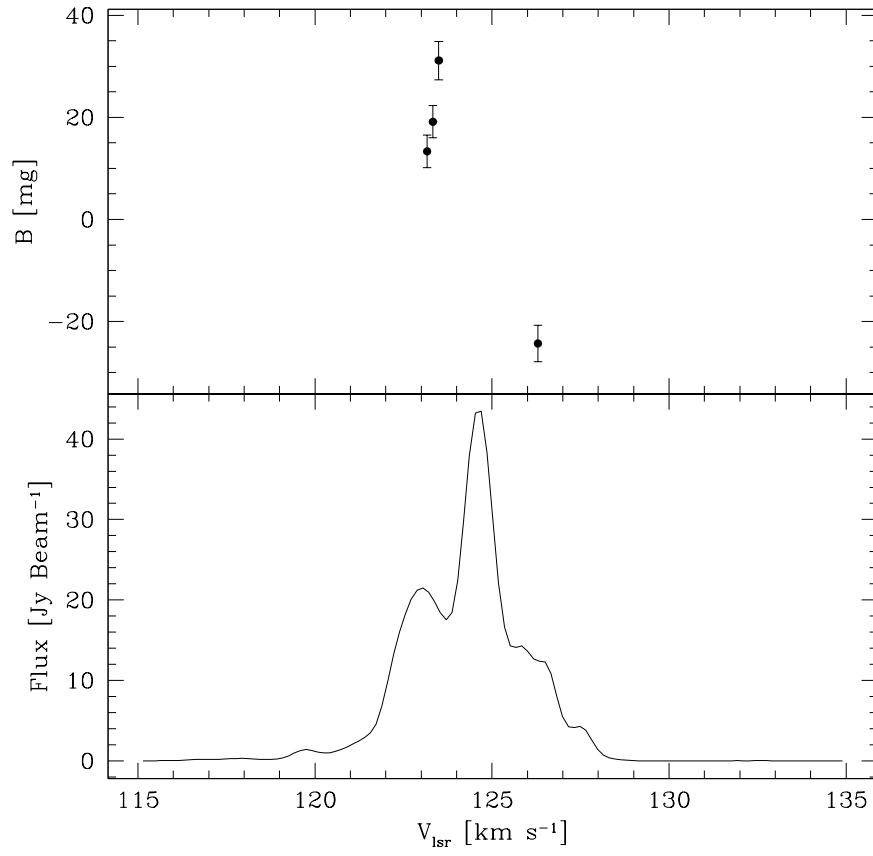
Figure 2.5 – Bottom panel: The total intensity spectrum of the red-shifted H_2O masers of W43A obtained from the GBT observations. The top figure shows the magnetic field strength measured for the red-shifted part of the spectrum.

the H_2O masers occur in a shock since the measured magnetic field of 100 μG is more consistent with the estimated magnetic field from the shock model (70 μG).

In the H_2O maser region of W43A, Vlemmings et al. (2006) concluded that the linear polarization is perpendicular to the magnetic field and aligned to the jet. However, at the low frequency of OH , Faraday rotation makes the derivation of the magnetic field configuration impossible. For a source at 2.6 kpc and a typical value of the interstellar magnetic field of 1 μG and a density of n_e = 0.03 cm^{-3}, the Faraday rotation is $\sim$ 125 °. Additionally, the internal Faraday rotations introduce large scattering of polarization angle (Fish & Reid 2006). Therefore, it is not possible to determine the absolute geometry of the magnetic field in the OH maser region of W43A.

2.4.4   OH maser shell expansion of W43A

Our observations reveal that the OH and H_2O masers in the CSE of W43A occur in two emission clusters with opposite velocity separations. The locations of the blue and red-shifted OH maser components are reversed compared with the H_2O emission features (Fig. 2.4).

From our MERLIN observations, we obtained an angular separation of 0.28±0.02 arcsec between the red and blue-shifted OH features. The observed velocity difference is $\sim$ 13 km/s between the two emission complexes. The fact that the red and blue-shifted features are not coincident on the sky is not fully compatible with a spherically symmetric expanding shell. Similar observations of the OH maser shell of W43A were performed previously. The 1612 MHz MERLIN observations by Diamond & Nyman (1988) on March 1981, showed an angular separation of 0.21±0.03 arc sec with a velocity splitting of $\sim$ 16 km/s between the two emission clusters. Assuming the two sets of observations are tracing the same sites of OH emission, the measured expansion is 0.07 ±0.03 arcsec in 26.5 years, which is equivalent to 2.67±1.37 mas/yr. Assuming spherical expansion, this corresponds to an expansion velocity of V_{exp} $\sim$ 18 km/s in the OH maser shell of W43A, consistent with typical OH/IR expansion velocities (Sevenster 2002). Thus, even though the maser morphology indicates a spherical shell is unlikely, there is no strong indication for fast, non-spherical expansion of the OH maser region.
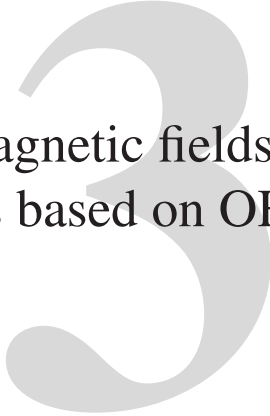
2.5   Conclusions

The non-spherical shape of PNe is thought to be related to outflows already generated during the AGB phase. Magnetic fields are considered as collimating agents of the jets around evolved stars. The magnetic field and jet characteristics of W43A, an evolved star in transition to a PN, have been previously reported from H_2O maser polarization observations. Our GBT observations reveal a magnetic field strength $B_{\parallel}$ changing sign from 31 ± 8 mG to −24 ± 7 mG across the H_2O masers in the red-shifted lobe of the W43A precessing jet. We observed the OH maser region of the CSE of this star and measured circular and linear polarization. Due to Faraday rotation, we can not determine the magnetic field configuration in the OH maser shell. However, the measured circular polarization, which is attributed to the Zeeman effect, implies a magnetic field of 100 μG in the OH maser region of W43A. Our result is consistent with the predicted magnetic field extrapolated from the blue-shifted H_2O maser region of W43A, and further confirms that the magnetic field plays an important role in the transition from a spherical AGB star to a non-spherical PN.

We considered the motion and expansion of the OH maser region of W43A. The observed expansion is 2.67±1.37 mas/yr, which corresponds to an expansion velocity of ~18 km/s. While the significantly offset red- and blue-shifted caps of the OH maser shell indicates it is a-spherical, the measured OH maser motions do not show any signs of a clear bipolar expansion in the plane of the sky.

Acknowledgements

The kinematics and magnetic fields in water-fountain sources based on OH maser observations

N. Amiri, W. H. T. Vlemmings, H. J. van Langevelde

Abstract

Water-fountain sources are a class of post-AGB objects that exhibit bipolar jet-like structures traced by H_2O maser emission. The circumstellar envelopes of these objects show deviations from spherical symmetry. While the H_2O masers originate in a collimated outflow in the polar region, the OH masers may be distributed in the equatorial region or a biconical outflow in the circumstellar shell. Magnetic fields could play an important role in collimating the jet and shaping the circumstellar envelope of these objects. The aim of this project is to understand the morphology of the OH masers in three water-fountain sources, for which we obtained high-resolution interferometric data. We compare the observational parameters of the spectral profile and spatial distribution with our models in order to constrain the morphology and velocity fields of the OH maser shell. We would also like to understand the role of the magnetic field in shaping the circumstellar envelope of these stars. We observed the OH masers of three water-fountain sources (OH 12.8-0.9, OH 37.1-0.8, and W43A) in full polarization spectral line mode using the UK Multi-Element Radio Linked Interferometer Network. Additionally, we performed reconstruction models of OH maser shells distributed uniformly in equatorial or biconical outflows and compared them with the OH maser observations. The OH masers of W43A seem to be located in the equatorial region of the circumstellar shell, while for OH 12.8-0.9 the masers are likely distributed in a biconical outflow. We measured magnetic fields of ~360 μG and ~ 29μG on average for OH 37.1-0.8 and OH 12.8-0.9, respectively. The measured field strengths show that a large-scale magnetic field is present in the circumstellar environment of these stars. Our observations show that the OH maser region of the three water-fountain sources studied in this work show signs of aspherical expansion. Reconstruction of the OH maser distribution of these objects show both biconical and equatorial distributions. Magnetic fields likely play an important role in shaping the OH maser region of water-fountain sources.

3.1   Introduction

Maser emission occurs in different regions of the circumstellar envelope (CSE) of evolved stars and can be studied at high angular resolution. These masers are good tracers of the outflow and morphology. In the picture of regular asymptotic giant branch (AGB) stars, SiO masers occur close to the central star, while the H_2O and OH masers are found at progressively further distances (e.g. Habing 1996). The OH masers often exhibit double-peak profiles, while the H_2O maser spectra are typically more irregular and have a velocity range confined within the OH spectrum (e.g. Reid & Moran 1981).

Water-fountain sources are defined by having high-velocity H_2O masers, and they are observed to have jets. The spectral characteristic and the spatial morphology of the OH and H_2O masers of these objects are unique and differ from those of typical AGB stars. The OH and H_2O masers of these objects show double-peak profiles; however, the H_2O maser velocity range exceeds that of OH masers (Likkel et al. 1992). For example, OH 09.1-0.4 has water maser emission spread over nearly 400 km s^{-1} (Walsh et al. 2009). Therefore, these objects can not be understood by the standard expanding shell model. An archetype of this class of objects is W43A, for which interferometric observations showed highly collimated H_2O maser jets, with a 3D outflow velocity of 145 km s^{-1} (Imai et al. 2002). Interferometric observations of the H_2O masers of other water-fountains (e.g. IRAS 16342-3814, IRAS 19134+2131, and OH 12.8-0.9) also revealed bipolar distributions (Morris et al. 2003, Claussen et al. 2004, Boboltz & Marvel 2005).

The bipolar jets observed in water-fountain sources are presumably to be related to the onset of asymmetric planetary nebulae (PNe) (Sahai & Trauger 1998). The majority of the observed planetary nebulae show elliptical or bipolar structures (Manchado et al. 2000). During the post-AGB phase, the jet-like outflows modify the CSEs, for example, by carving out polar cavities. It could be this imprint that provides the morphological signature of the aspherical PNe. These jets are thought to form on a very short time scale, less than 100 years during the transition from the AGB phase to PNe (Imai et al. 2002).

Although H_2O masers are found in bipolar jet-like structures in water-fountain sources, the distribution of OH masers in the CSE of these stars is not clear. For example, the blue-shifted and red-shifted OH masers of W43A are separated in the plane of the sky and in the opposite direction with respect to the blue-shifted and red-shifted H_2O masers (Diamond et al. 1985, Likkel et al. 1992, Imai et al. 2002). Likkel et al. (1992) proposed that the OH masers of W43A are located in a biconical outflow surrounding the H_2O maser jet at lower latitudes. Likewise, Sahai et al. (1999) suggests that the OH masers of the water-fountain source IRAS 16342-3814 are located at intermediate systemic latitudes, where the outflow velocity is much lower than along the polar axis. So far, no systematic studies have been performed to explain the morphology of the OH masers in water-fountains. Therefore, it is important to investigate observational parameters, such as the profile shape and spatial distribution, and compare them with geometrical models to constrain the morphology and velocity field of these objects.

The H_2O maser jets observed in water-fountain sources may result from magnetic collimation (García-Segura et al. 2005). Theoretical models indicated that magnetic fields in AGB stars are driven by a dynamo. However, in order to maintain the differential rotation an additional source of angular momentum such as a binary companion or a heavy planet is required (Nordhaus et al. 2007). In addition to probing the morphology of the CSEs, masers are useful tracers of the magnetic field strength and structure around these stars. For example, H_2O maser polarimetric observations

35

of W43A showed that the jet is magnetically collimated (Vlemmings et al. 2006). Follow up polarimetric observations of the OH maser region showed evidence for a large scale magnetic field in the circumstellar environment of this star (Amiri et al. 2010, hereafter A10).

In this paper, we present the 1612 MHz OH maser polarimetric observations of three water-fountain candidates (W43A, OH 12.8-0.9 and OH 37.1-0.8). For two sources, OH 12.8-0.9 and OH 37.1-0.8 the observations are presented for the first time. The observations are compared with the kinematical reconstruction models in order to understand the OH maser morphology of these objects. In Sect. 2 we describe the MERLIN observations. The results of the observations are shown in Sec. 3.3. The modeling procedure and comparison with observations are discussed in Sect. 3.4.

3.2 MERLIN Observations

We observed the 1612 MHz OH masers of three water-fountain sources with the UK Multi-Element Radio Linked Interferometer Network (MERLIN). The observations were performed on 7 May 2007, 4 June 2007 and 6 June 2007 for OH 37.1-0.7, OH 12.8-0.9 and W43A respectively. We achieved a spatial resolution of of 0.3×0.2 arcsec. The observations of W43A were presented earlier (A10). Here we present the observations of the two other sources, following the same procedure as we used for W43A.

For OH 37.1-0.8, the observations were performed in full polarization spectral line mode with 256 spectral channels and a bandwidth of 0.25 MHz, covering a velocity width of 44 km s^{-1} and a channel width of 0.2 km s^{-1}. The observations were interleaved with observations of the phase reference source, 1904+013, in wide-band mode in order to obtain an optimal signal-to-noise-ratio. 3C286 was observed as primary flux calibrator and polarization angle calibrator. 3C84 was observed both in narrow band and wide band modes in order to apply band pass calibration and a phase offset correction. The rms noise in the emission free channels was 6.5 mJy.

Similarly, the observations of OH 12.8-0.9 were performed in full polarization spectral line mode. We also used a bandwidth of 0.25 MHz, but now with 512 spectral channels. This covers a velocity range of ~44 km s^{-1} with a spectral resolution of 0.08 km s^{-1}. We observed the phase calibrator 1829–207 in wide band mode, in order to obtain sufficient signal to noise ration. 3C286 and 3C84 were observed as a primary flux calibrator and polarization angle calibrator. The rms noise in emission free channels was 9.4 mJy.

The initial processing of the raw data and conversion to FITS file were performed using the local "d-programs" at Jodrell Bank. 3C286 was used to obtain the flux density of the amplitude calibrator 3C84. We used the Astronomical Image Processing Software Package (AIPS) to perform the rest of the calibration, editing and imaging of the data. We corrected the phase offset between the wide and narrow band data by determining the difference in phase solution for 3C84. These solutions were then applied to phase reference source. The phase and amplitude corrections derived from the phase calibrator where applied to the target data set.

The polarization calibration for leakage was determined using 3C84, and the R and L phase offset corrections were performed on 3C286. Image cubes were created for stokes I, Q, U, V, RR and LL. A linearly polarized data cube was made using the Stokes Q and U. Using the AIPS task SAD, OH maser features with peaks higher than three times the rms noise in the emission free channel were identified and fitted with a Gaussian in the total intensity image cube.

We use the cross-correlation method introduced by Modjaz et al. (2005) to measure the magnetic field due to the Zeeman splitting. In this method the right circular polarization (RCP) and the left circular polarization (LCP) spectra are cross-correlated to determine the velocity splitting. The magnetic field is determined by applying the Zeeman splitting coefficient to the measured velocity splitting. We refer to A10 for a detailed description of the polarization procedure.

3.3 Results

3.3.1 OH maser observations of OH 12.8-0.9

Fig. 3.1 shows the total intensity and the stokes V spectra of OH 12.8-0.8. The stokes I spectrum shows a double peak structure with peaks at -68.0 and -43.7 km s^{-1}, which is typical for the OH masers of AGB stars. Since maser lines are very narrow, it is likely that each of the peaks in the spectrum is a blend of several maser lines.

The properties of the OH maser features identified using the AIPS task SAD are shown in Table 3.1. Each maser feature consists of several maser spots. On average, we measured a magnetic field of $\sim -31\mu$G and $\sim 27\mu$G for the blue-shifted and red-shifted regions, respectively. The magnetic field measured for the blue- and red-shifted features have opposite signs which may indicate a clear difference between the blue- and red-shifted regions. We found no significant linear polarization for the OH maser features of this source. Additionally, no stokes V signal is apparent in the spectrum shown in Fig. 3.1, which corresponds to the total V emission from all maser features. However, an individual analysis of the features identified with SAD using the cross-correlation method still produces 3-4 σ detections of the magnetic field strength. This is confirmed by the V-spectra, shown in Fig. 3.2, taken at the location of one of the individual maser feature (feature 13). Now a circular polarization signal is clearly visible.

The spatial distribution of the blue- and red-shifted OH maser spots of OH 12.8-0.9 are plotted in Fig. 3.1. The spots are color-coded according to their radial velocity. We calculated the average position for the red- and blue-shifted spots. The distribution of the spots implies that the maximum extent of the OH maser region and the offset between the blue- and red-shifted emission are ~500 mas and ~135 mas in the plane of the sky, respectively. The measured offset is slightly higher than the standard deviation in the spread of the red- and blue-shifted maser features (~100 mas), and significantly larger than the positional uncertainty on the individual features (<30 mas). The distance to OH 12.8-0.9 is not accurately known, based on Galactic rotation models it was estimated to be 8 kpc (Baud et al. 1985), but this could be off by a considerable amount. At a distance of 8 kpc, the measured maximum extent of the OH maser region of this source corresponds to 4000 AU. However, the actual extent of the OH maser region could be much larger, since we only detected emission at the blue- and red-shifted peaks and no emission was found close to the stellar velocity (V_{lsr}=-55 km s^{-1}). The observed distribution does not seem to be explained by the spherically expanding shell model, in which the red- and blue-shifted peaks should be coincident.

Figure 3.1 – Top panel: Total power (I) and stokes V spectra of the OH maser region of OH 12.8-0.9. The V spectrum is shown after removing the residual scaled down of the stokes I. Bottom panel: The OH maser region of OH 12.8-0.9. The offset positions are with respect to the maser reference feature 1. The maser spots are color-coded according to their radial velocity, measured in km s^{-1}. The size of the spots is scaled logarithmically according to their flux density.
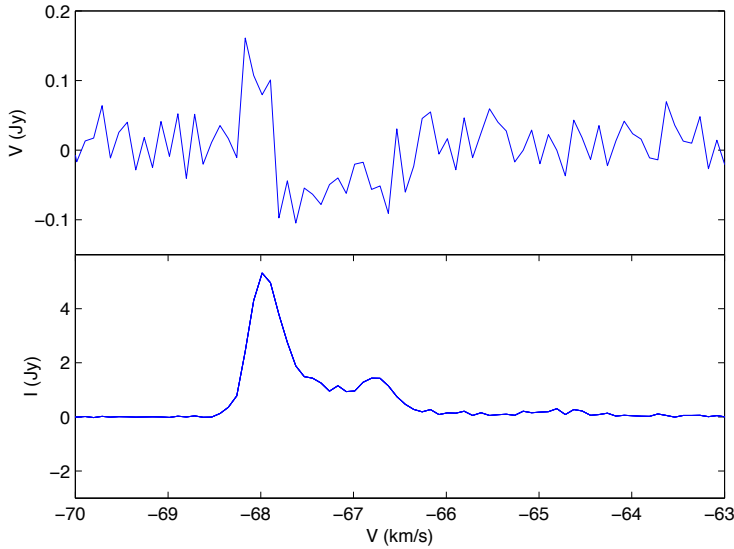
Figure 3.2 – Total intensity (bottom panel) and stokes V (top panel) spectra of the blue shifted OH maser region of OH 12.8-0.9 taken at the position of feature 13. The V spectrum is shown after removing the residual scaled down of the stokes I.

3.3.2 OH maser observations of OH 37.1-0.8

Fig. 3.3 displays the total intensity and stokes V spectra of OH 37.1-0.8. The spectrum shows a double peak structure. The emission is also detected in the circular polarization profile. The red-shifted emission ranges from 73 km s^{-1} to 78 km s $^{-1}$. The blue-shifted emission ranges from 95 km s $^{-1}$ to 103 km s^{-1}. Each of the blue-shifted and red-shifted regions has multiple peaks and is a blend of several lines. In Table 3.2 we present the maser components that we identified for the OH maser region of this star, using the AIPS task SAD. Each component consists of several maser spots. We did not find significant linear polarization for the OH maser features of this source. On average we measured a magnetic field of ~430 μG and ~230 μG for blue- and red-shifted masers, respectively.

Fig. 3.3 displays the spatial distribution of the OH maser spots of OH 37.1-0.8. We determined the average position for the red- and blue-shifted peaks. The maximum extent of the OH maser region and the offset between the blue- and red-shifted emission are ~200 mas and ~100 mas, respectively. The offset is almost twice higher than the standard deviation in the spread of the red- and blue-shifted maser features (~50 mas). The best estimate for the distance of this source based on galactic rotation model is 8 kpc (Baud et al. 1985). At this distance, the measured maximum extent of the OH maser region of this source is ~ 1600 AU. This distribution is not consistent with spherically symmetric shell model, since the blue-shifted and red-shifted maser features are not coincident in the plane of the sky.

Feature	RA 18 16	Dec. -18 15	Velocity km s^{-1}	Flux Jy beam^{-1}	B μG
1	49.21560	1.53	-43.65	9.3	< 19
2	49.21315	1.53	-43.4	7.8	<19
3	49.21947	1.89	-43.9	0.3	< 37
4	49.21560	1.56	-44.5	1.9	<22
5	49.21111	1.53	-45.3	0.4	27 ± 7
6	49.21947	1.62	-45.7	0.6	< 44
7	49.22368	1.80	-46.2	0.3	< 23
8	49.21947	1.74	-46.6	0.5	< 127
9	49.21862	1.77	-47.5	0.6	< 165
10	49.22189	1.59	-65.3	0.3	< 29
12	49.22579	1.50	-66.2	0.3	< 39
13	49.22347	1.44	-67.9	0.3	-45 ± 12
14	49.22158	1.50	-66.7	1.5	-27 ± 8
15	49.21685	1.50	-66.9	1.6	-21 ± 6
16	49.21581	1.56	-67.6	9.1	< 17
17	49.21105	1.53	-66.9	0.8	< 15

Table 3.1 – Properties of the OH maser features of OH 12.8-0.9. Each maser feature consists of
several maser spots. The upper limits are given in absolute values.

feature	RA 19 02	Dec 03 20	V km s^{-1}	peak flux Jy	B μG
1	6.28344	15.7047	102.3	1.9	180 ± 3
2	6.28736	15.6984	102.6	5.0	180 ± 2
3	6.29012	15.6579	101.6	3.1	240 ± 3
4	6.2978	15.6186	101.4	2.1	260 ± 5
5	6.29083	15.658	99.8	2.8	240 ± 3
6	6.29074	15.6257	99.6	3.8	290 ± 7
7	6.2800	15.66	77.3	4.2	150 ± 4
8	6.28534	15.66	74.2	4.7	850 ± 5
9	6.28801	15.66	74.02	2.5	260 ± 7
10	6.28801	15.7	73.8	1.3	720 ± 6

Table 3.2 – Properties of the OH maser features of OH 37.1-0.8. Each maser features consists of
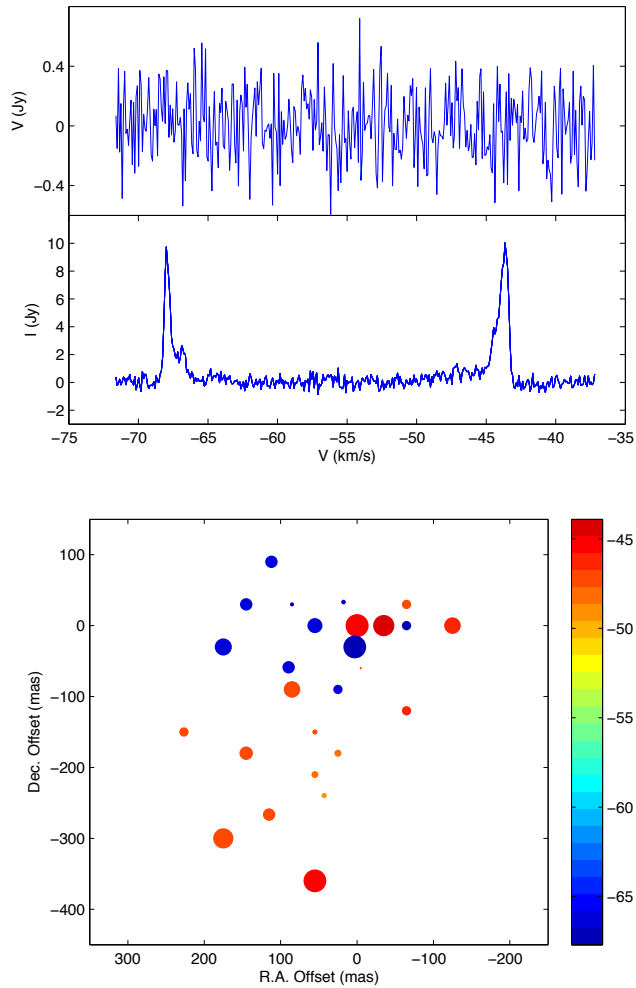several maser spots.
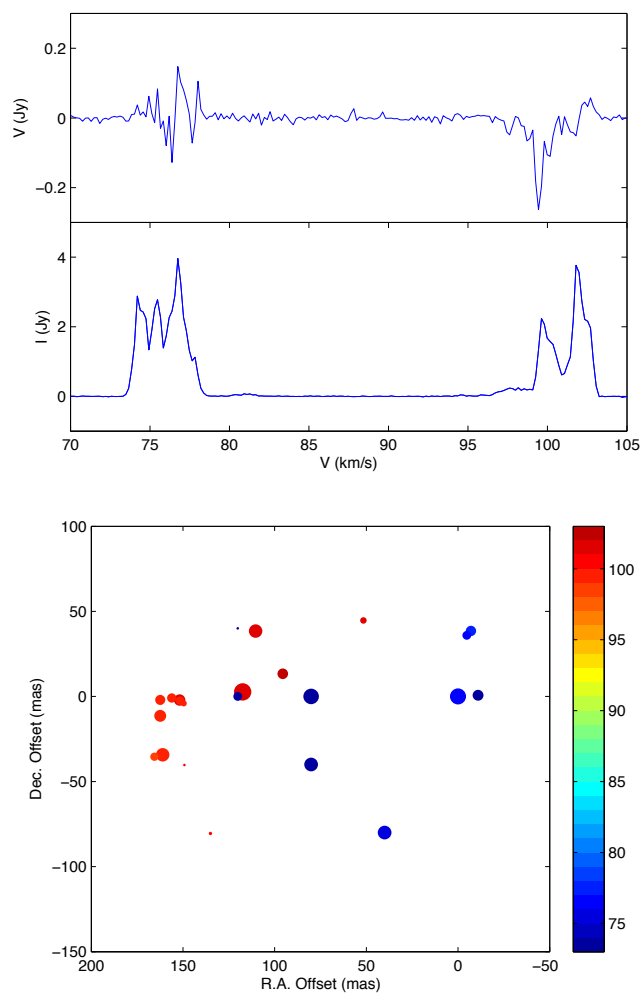
Figure 3.3 – Top panel: Total power and the stokes V spectra of the OH maser region of OH 37.1-0.8. The V spectrum is shown after removing the residual scaled down of the stokes I. Bottom panel: The OH maser region of OH 37.1-0.8. The offset positions are with respect to the maser reference feature 7. The maser spots are color-coded according to their radial velocity, measured in km s^{-1}. The size of the spots is scaled logarithmically according to their flux density.

3.4 Analysis

3.4.1 Description of the kinematical reconstruction procedure

The observations of the H_2O masers in a number of water-fountain sources revealed that these masers are located in bipolar structures (e.g Vlemmings et al. 2006, Boboltz & Marvel 2005). Thus the spherically symmetric circumstellar envelope is modified, for example by carving out polar cavities. In order to understand the geometry of the OH maser region of these sources, we performed a geometrical reconstruction of the masers in three dimensional grids. We did not consider radiative transfer of masers in our analysis. Instead, the velocity coherent path length along the line of sight was determined for maser shells of various geometries and velocity fields. In all cases, we assumed a maximum shell radius of 3×10^{16} cm (~2000 AU), which is typical for OH masers (Chapman & Cohen 1986).

We assumed that the masers are saturated and that the resulting intensity increases linearly rather than exponentially with path-length. Observations indicate that the 1612 MHz respond smoothly and linearly to the change in physical conditions and pump rates, which could indicate that the masers are saturated (Elitzur 1990). Therefore, the saturation assumption enables us to investigate the extent at which the velocity field along the line of sight contributes to the profile and structure of the maser shells, but not the line strengths in detail.

A similar analysis was performed by Bowers (1991), in which they obtained the velocity coherent path length along the line of sight for ellipsoidal shells with various inclinations from the plane of the sky. They also considered different velocity fields, incorporating isotropic velocity, rotation and radial acceleration. We use a similar modeling procedure, but we expand our work to more complex morphologies and velocity fields that may explain the distribution of OH masers in water-fountain sources which show significant deviation from spherically symmetric CSEs. For the basic method we refer to Bowers (1991).

We consider two different possibilities for the distribution of OH masers in water-fountain sources: equatorial distribution or biconical outflow (Fig. 3.4). In the case of equatorial distribution, the OH masers stem from the equatorial region of the circumstellar shell, while the H_2O masers are located in a bipolar jet-like outflow. Alternatively, the OH masers may originate in a biconical outflow surrounding the H_2O maser jet (Likkel et al. 1992). The spectral profile and emission structure were calculated assuming these two morphologies. Throughout our analysis the opening angle in the case of equatorial distribution is defined as the angle from the equatorial plane. In contrast, for a biconical outflow the opening angle is defined from the polar axis.

We incorporate two different velocity fields: isotropic expansion or azimuthally dependent velocity, either towards the equatorial plane or the polar axis. In the case of isotropic outflow, we assume a constant expansion velocity of 15 km s^{-1}, which is typical for the OH maser in evolved stars (e.g. Sevenster 2002). Since the velocity scales linearly with the extent of the velocity, choosing other values of the expansion velocity does not change the profile shape in our models. In the case where the velocity is enhanced towards the equatorial plane, we use $V_{exp} = a + b \times |\sin\phi|$. Similarly, if the velocity increases towards the polar axis, we adopt $V_{exp} = a + b \times |\cos\phi|$. In both cases $a + b = 15$ km s^{-1}. In all cases ϕ is the angle from the polar axis.

If the velocity has a latitudinal dependence, we assume an elongated ellipsoid geometry for the

maser shell. We define the ellipticity ($e = \sqrt{1 - \frac{R_{min}^2}{R_{max}^2}}$) of the oblate or prolate shells by the velocity ratio between the major and minor axes of the ellipsoid ($p = \frac{a+b}{a}$, $e = \sqrt{1 - p^2}$). We present the results for two values of ellipticity ($e = 0.7$ and $e = 0.9$), which implies that the velocity of the major axis of the ellipse is twice and four times higher than that for the minor axis of the ellipse. The models in this section have not been adjusted to match the data for a specific object.

The following plots are presented for each model:

1. Normalized intensity profile versus velocity, which indicates the path length along the line of sight for each velocity integrated over the sky. We calculated the spectra for inclinations of 0°, 15°, 30°, 45°, 60°, 75°, 90° from the plane of the sky. At each inclination, the spectra are presented for 25°, 45°, 65°, 80° opening angles.

2. The offset between the blue-shifted and red-shifted peaks in the plane of the sky. The spatial distribution of the OH maser region of a number of water-fountain sources reveal that the blue-shifted and red-shifted features are separated in the plane of the sky. For the cases where the spectrum shows the typical double peak profile, we calculated the position of the blue-shifted and red-shifted peaks and measured the offset. For more complex spectra where the spectra show inner peaks it becomes more complicated as the position of the inner peaks and outer peaks are different. Therefore, we measured the position of the outer peaks for the blue-shifted and red-shifted emission and determined the offset value. For example, Fig. 3.5 shows the distribution of the blue-shifted and red-shifted peaks in the case where masers are confined within 30° from the equatorial plane with an inclination of 40° from the sky plane, which shows that the OH masers are reversed in the plane of the sky compared to those of the bipolar outflow. Similarly, for all cases we determined the separation between the blue shifted and red shifted regions. The negative sign for the offset values implies that the masers are located in the opposite direction with respect to the fast bipolar H_2O maser outflow.

We consider different scenarios, which are intended as a guide for analysis of the OH masers in water-fountain sources. The plots presented are particularly useful for comparison with the observed parameters of spectral structure and spatial distribution in these objects. Fig. 3.6 and Fig. 3.7 show the results for the cases of equatorial and biconical distribution of the masers, where the expansion velocity is constant in all directions. For the other cases where the velocity has latitudinal dependence we present the result of our modeling calculations in Fig. 3.8- 3.15.

A1: Equatorial distribution, V_{exp}=constant

This case describes the situation that the OH masers remain active in the equatorial plane, while H_2O masers originate in a high velocity outflow in the polar region. The outflow velocity is constant in all directions. The OH masers in this scenario would have a slower expansion velocity with respect to the fast outflow in the polar region.

Fig. 3.6 displays the results for this case. The spectra show double peak structure for inclinations below 45° from the plane of the sky. For 60° and 75° inclinations, the spectra display inner peaks for opening angles smaller than 45°. At 90°, the spectra again show double peaks.

The diagram at the bottom shows the offset between the blue-shifted and red-shifted regions versus opening angle from the equatorial plane. Each line shows the offset at a specific inclination. For 0°, 15° and 90° inclination angle from the plane of the sky, the separation is zero and the blue-shifted and red-shifted emission coincide in the plane of the sky. For other inclinations the masers are
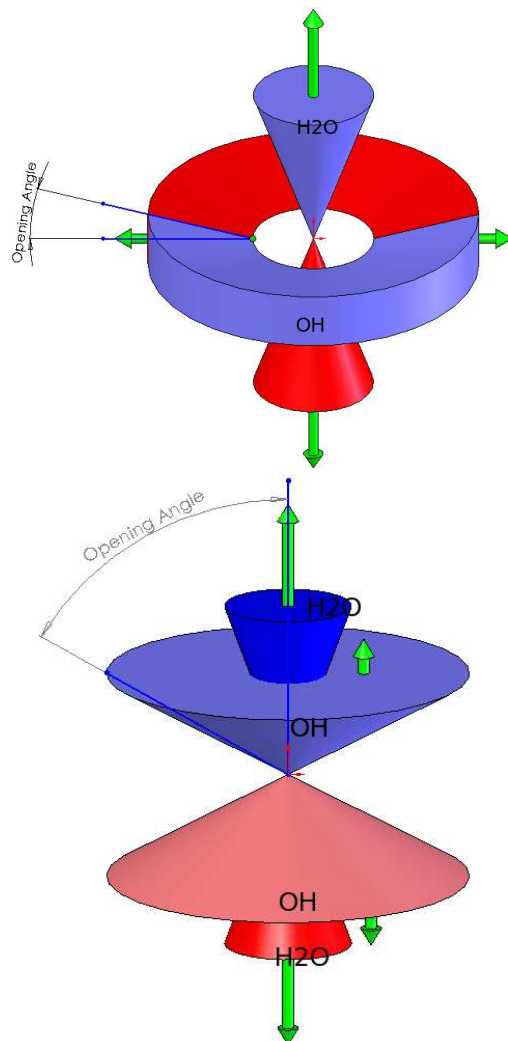
Figure 3.4 – Top panel: Equatorial distribution of the OH masers surrounding the H_2O maser jet
in the CSEs of water-fountain sources. The opening angle is shown from the equatorial plane.
Bottom panel: Biconical distribution of the OH masers around the H_2O maser jet in the CSEs of
water-fountain sources. The opening angle is shown from the polar axis.
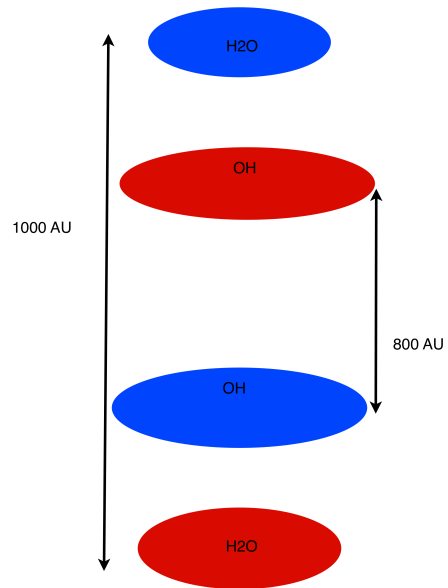
Figure 3.5 – The offset between the blue-shifted and red-shifted peaks of maser emission calculated from the models. The OH masers are confined within 30° from the equatorial plane with an inclination of 40° from the plane of the sky. The models show that the OH masers are reversed in the plane of the sky compared to those of the bipolar H_2O maser outflow.
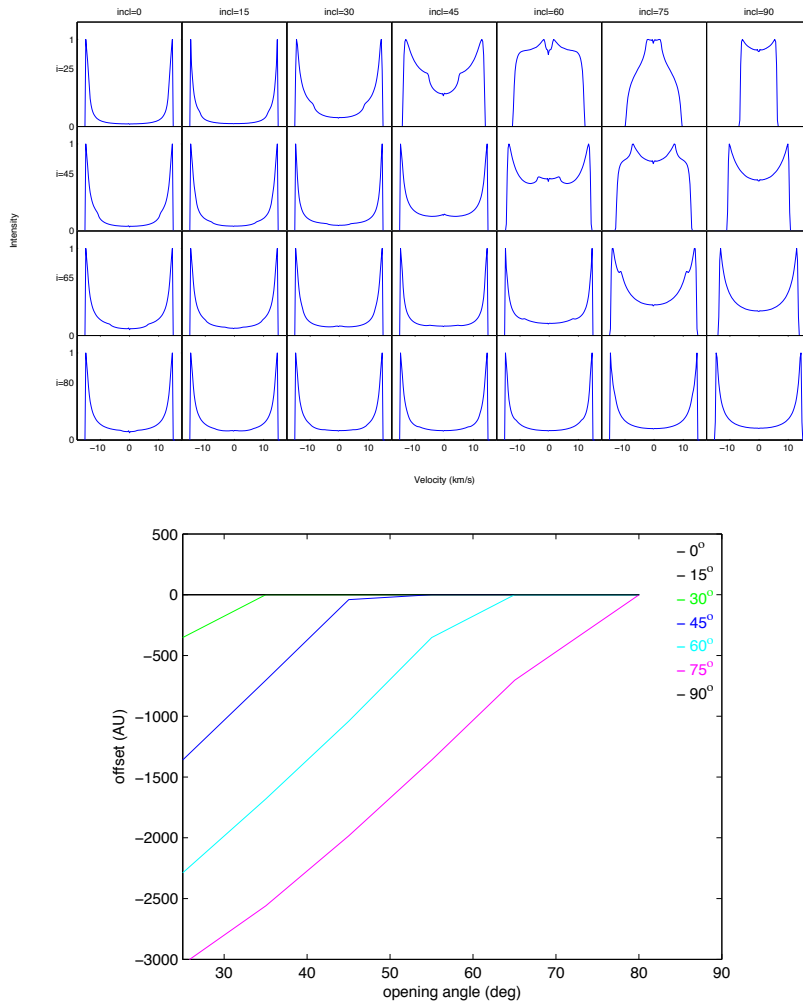
Figure 3.6 – Model calculations for the case of isotropic outflow of 15 km s^{-1} with equatorial distribution. The top panel shows the spectra calculated for inclinations of 0°,15°,30°,45°,60°,75°,90° from the plane of the sky. For each inclination the spectra are shown for 25°, 45°, 65° and 80° opening angle from the equatorial plane. The bottom panel displays the offset between the blue shifted and red shifted regions in the plane of the sky. The negative sign indicates that the masers are reversed in the plane of the sky compared to those located in a narrow region in the polar axis.

reversed in the sky plane. The offset is highest at small opening angles and as expected approaches 0 for large opening angles in the equatorial region. The highest offset is ~3000 AU.

A2: Equatorial distribution, $V_{exp} = a + b \times |\sin \phi|$

Similar to case A1, we assume equatorial distribution for the masers. But we adopt a latitudinal dependent velocity of $V_{exp} = a + b \times |\sin \phi|$, where the velocity is highest in the equatorial plane and decreases towards the polar region. The shell geometry is elongated towards the equatorial plane. This case potentially describes the situation where the masers are affected by a binary companion in the equatorial region of the circumstellar envelope.

We calculated the spectra and map structure for $e = 0.7$ and $e = 0.9$. The results of this case are shown in Fig. 3.8 and Fig. 3.9. Comparison of the spectra obtained for this scenario and those for the case A1, shows that the shape of the spectra remains similar at inclinations below 60°, where the spectra show double peaks. Above 60° inclination the inner peaks occur, which dominate the emission at the edges of the spectrum for the case of $e = 0.9$.

Again, the second figure displays the offset value between the blue-shifted and red-shifted peaks. At 0° and 90° inclinations from the plane of the sky, the separation is zero. For other inclinations the masers are reversed and the offset is in the range 400-2500 AU and 400-2500 AU for the cases of $e = 0.7$ and $e = 0.9$, respectively.

A3: Equatorial distribution, $V_{exp} = a + b \times |\cos \phi|$

In this case we assumed equatorial distribution for the masers but the shell geometry is considered to be elongated towards the polar axis. The velocity field is latitudinally dependent ($V_{exp} = a + b \times |\cos \phi|$), which implies that the velocity increases towards the polar region.

We calculated the models for $e = 0.7$ and $e = 0.9$, the results of which are shown in Fig. 3.10 and Fig. 3.11. The spectra show significant differences compared to the case A1, where the velocity is constant in all directions. For all inclinations the spectra show inner peaks, which are even higher than the emission at the edges of the spectrum for opening angles smaller than 45°.

The bottom figure shows the separation between the blue shifted and red shifted regions. For 0° and 90° inclination from the plane of the sky, the offset between the blue shifted and red shifted regions is zero. At 45°, 60° and 75° inclinations the masers are reversed when the opening angle is smaller than 45°, 60° and 75° from the equatorial plane, respectively. The maximum offset value is ~1500 AU and ~800 AU for the cases of $e = 0.7$ and $e = 0.9$, respectively.

B1: Biconical distribution, V_{exp}**=constant**

A biconical distribution is another possibility for the distribution of OH masers in water-fountain sources (Likkel et al. 1992, Sahai et al. 1999). In this case, the OH masers are located in a biconical outflow surrounding the H_2O maser jet, but at lower latitudes (Fig. 3.4) with a constant expansion velocity of 15 km s^{-1}.

Fig. 3.7 displays the results for this case. The spectra show double peak structures generally. However, at inclinations of 0°, 15 ° and 30° there are strong inner peaks for small opening angles (i ≤45).

For 0° and 90° inclination angle from the sky plane the offset between the blue-shifted and red-shifted peaks is zero. In contrast to case A1, the masers are not reversed in the plane of the sky. The maximum offset value is 3000 AU.
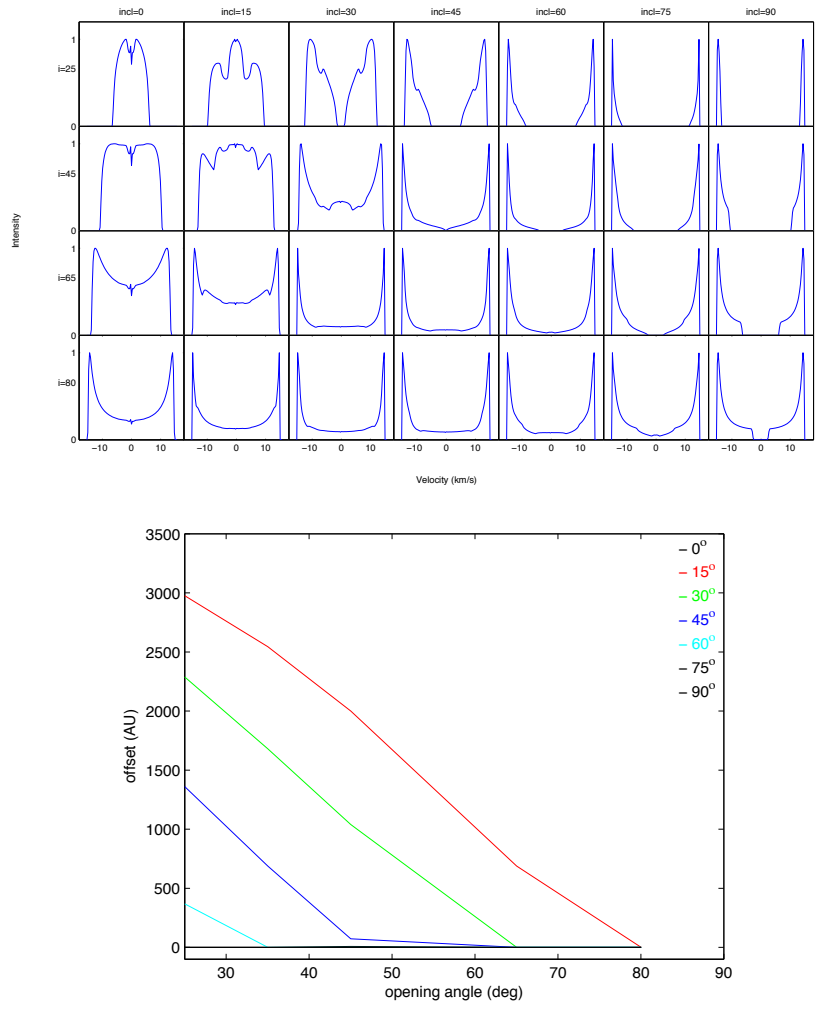
Figure 3.7 – Model calculations for the case of biconical outflow with constant expansion velocity of 15 km s^{-1}.

B2: Biconical distribution, $V_{exp} = a + b \times |\sin \phi|$

In this scenario, the masers are distributed in a biconical outflow and the expansion velocity increases azimuthally towards the equatorial region. This case describes the situation where the masers are affected by a binary companion in the equatorial region, while they are still entrained by the fast collimated outflow in the polar region.

We calculated the models for $e = 0.7$ and $e = 0.9$. The results of this case are shown in Fig. 3.12 and Fig. 3.13. Comparison of the spectra obtained for this case and those for the case B1 show significant differences in the profile structure for inclinations above 45°, where most of the spectra show inner peak emission.

The bottom figure shows the offset between the blue-shifted and red-shifted emission. The masers are reversed for large inclinations from the plane of the sky, in particular at 45°, 60° and 75°. The maximum offset value is ~1500 AU and ~800 AU for $e = 0.7$ and $e = 0.9$ respectively.

B3: Biconical distribution, $V_{exp} = a + b \times |\cos \phi|$

In this case, the masers are distributed in a biconical outflow and the velocity has latitudinal dependence towards the polar axis. Fig. 3.14 and Fig. 3.15 show the results for $e = 0.9$ and $e = 0.9$ cases.

For 45° to 90° inclination angle from the plane of the sky, the spectra show double peak profiles, however for 0° to 30° inclinations the spectra show inner peaks. The offset between the blue shifted and red shifted regions is higher for smaller opening angles and approaches zero for higher opening angles. The maximum offset value is ~2500 AU and ~1600 AU for $e = 0.7$ and $e = 0.9$ respectively.

3.4.2 Application to individual sources

3.4.2.1 W43A

W43A is a unique water-fountain source because it exhibits OH (1612, 1665 and 1667 MHz), H_2O and SiO masers (A10; Nyman et al. 1998, Imai et al. 2002). The spectra of the OH and H_2O masers of this object exhibit double peak profiles. The H_2O maser velocity range (~180 km s^{-1}) is much higher than that for the OH masers ($\sim$ 13 km s^{-1}), which makes this the archetype water-fountain source (Imai et al. 2002, Likkel et al. 1992).

High resolution interferometric observations of the H_2O maser region of W43A revealed a highly collimated and precessing jet. The H_2O masers are found in two opposing clusters separated by ~1700 AU at a distance of 2.6 kpc (Diamond et al. 1985). The H_2O maser jet has an outflow velocity of $\sim$ 145 km s^{-1} with 39° inclination from the plane of the sky (Imai et al. 2002). The SiO masers of this source are thought to occur in a shock at the interface between the fast collimating jet and the slow biconical outflow (Imai et al. 2005). The spatial distribution of the OH maser region of W43A revealed that the OH masers are located inside the H_2O maser region. The OH masers are found in two opposing clusters separated by ~650 AU. The red-shifted and blue-shifted OH masers are reversed in the plane of the sky with respect to those of H_2O masers (A10).

The fact that the blue and red-shifted OH maser features are not positionally coincident in the plane of the sky, is not consistent with an isotropically expanding shell model. Additionally, the bipolar structure of the H_2O and SiO maser regions is another piece evidence that these masers are located

in a-spherical shells.

The expansion velocity of the OH maser region of W43A is ~ 18 km s^{-1} (A10). This seems to imply that the OH maser region is not affected by the fast post-AGB wind. We considered the two scenarios of either an equatorial distribution or a biconical outflow, as explained in section 3.4.1 and compared the spectral profile and the OH masers spatial distribution with the model calculations. The same inclination ($39°$) as that of the collimated H$_2$O maser jet was adopted for the OH maser region (Imai et al. 2002).

If the masers are distributed in the equatorial plane of the circumstellar shell with a constant expansion velocity in all directions, then our calculations show that the masers are reversed in the plane of the sky and the spectra would show double peak structures for all opening angles in the equatorial region (Fig. 3.6). For an opening angle of ~35°, the offset corresponds to the observed value of ~ 650 AU. If the velocity is azimuthally enhanced towards the equatorial plane, the spectra would show double peak profiles in all opening angles (Fig. 3.8 and Fig. 3.9). The models show that the masers are reversed in the plane of the sky, and the offset is in the range 400 AU to 700 AU for all opening angles in the equatorial plane. Therefore, this case may also describe the distribution of the OH masers of W43A.

On the other hand if the velocity has latitudinal dependence enhanced towards the polar axis, the spectra show inner peaks (Fig. 3.11). These profile shapes are not consistent with the OH maser profile of W43A. Therefore, this scenario is unlikely for the OH maser region of W43A.

Alternatively, we considered biconical distribution of the OH maser region of W43A. If the velocity is isotropic or azimuthally enhanced towards the polar axis, the masers are not reversed in the plane of the sky (Fig. 3.7 and Fig. 3.15), which is not consistent with the OH maser morphology of W43A. However, if the velocity is azimuthally enhanced towards the equatorial region, the spectra show double peak profiles at opening angles larger than 70°, for which the separation between the blue shifted and red shifted regions is ~650 AU (Fig. 3.13). Therefore, this scenario may also explain the OH maser morphology of W43A. However, for such large opening angles we are approaching an oblate distribution with enhanced outflow in the equatorial region. Thus, in either case, the reconstruction of the OH maser region of W43A suggests a predominantly equatorial distribution.

3.4.2.2   OH 12.8-0.9

OH 12.8-0.9 is a water-fountain candidate. This source was first reported by Baud et al. (1979) as a type II OH/IR star on the basis of its double peak 1612 MHz OH maser profile. The source IRAS 18316-1816 is identified as the IR counterpart to this source. The H$_2$O masers of OH 12.8-0.9 were first discovered by Engels et al. (1986). They also found that the OH masers of this object lie inside the H$_2$O maser velocity range, which is not typical for OH/IR stars. VLBI H$_2$O maser observations of this object revealed that the masers are located in two opposing clusters at the tips of a bipolar jet-like structure oriented north-south (Boboltz & Marvel 2005). The blue-shifted and red-shifted H$_2$O masers are found in arc-shape structures separated by ~ 110 mas in the plane of the sky.

Multi-epoch VLBA observations revealed a 3D outflow velocity of 58 km s^{-1} for the H$_2$O maser jet with 24° inclination from the plane of the sky (Boboltz & Marvel 2007). Comparison of the spatial morphology of the OH masers (Fig. 3.1) and the H$_2$O masers reveal that the OH masers are located outside the H$_2$O maser jet. The maximum extent of the OH maser region is ~500 mas, which is much larger than that for H$_2$O masers (~110 mas). This is in contrast to Boboltz & Marvel (2005)

expectation that the OH masers should be located inside the H_2O maser jet. Since this object is characterized as a high mass-loss source it is possible that this source is still in the AGB phase and that the jet has recently turned on in this source (Deacon et al. 2007).

We compared the observational parameters of the profile shape and spatial distribution (Fig. 3.1) with our model calculations. The OH maser spectrum of this source shows a double peak structure. Our observations show that the separation between the blue shifted and red shifted OH maser region of this source is ∼ 135 mas (Fig. 3.1). Assuming a distance of 8 kpc for this source, the offset corresponds to 1080 AU. Unlike W43A, the blue-shifted and red-shifted OH masers are not reversed in the plane of the sky compared to those of H_2O masers.

The equatorial distribution of the masers is unlikely. Our models show that the masers are reversed in the plane of the sky at 24° in the case of isotropic outflow and latitudinal dependent velocity enhanced towards the equatorial region (Fig. 3.6, Fig. 3.9). However, in the case where the velocity azimuthally increases towards the polar region, the masers are not reversed in the plane of the sky, but the spectral shapes in this case are quadruply peaked (Fig. 3.11), which is not consistent with the observed spectrum of this source.

If the masers are located in a biconical outflow with isotropic expansion velocity or azimuthal dependent velocity towards the polar axis, our results show that at opening angles of ≥ 65°, the spectra show double peak profiles (Fig. 3.7 and Fig. 3.15). However, the offset between the blue shifted and red shifted regions is smaller than 1000 AU. This implies that either the distance of 8 kpc is not accurate for this source or the assumption of maximum shell radius of 2000 AU is not correct. In the case of a biconical distribution where the velocity enhances towards the equatorial region (Fig. 3.13), at opening angles above 65° the profile shape is double peaked, however the offset approaches zero at these large opening angles, which is not consistent with the observed spatial distribution of the OH maser region of this source. Therefore, a biconical outflow with isotropic expansion velocity or azimuthal dependent velocity towards the polar axis may explain the OH maser morphology of this source. However, we do not consider other effects (e.g. anisotropic pumping, etc), that may produce the observed asymmetry of the OH maser region of this source.

3.4.2.3   OH 37.1-0.8

The H_2O masers of this source were first discovered by Engels et al. (1986) and the OH masers were first detected by Winnberg et al. (1975). The H_2O maser velocity range of this source (63-114 km s^{-1}; Engels (2002)) is higher than that for OH masers (73-103 km s^{-1}), which establishes the water-fountain nature of this source.

The spatial distribution of the OH maser of this source shows that these masers are located in a-spherical shell. The separation between the two corresponds to ∼100 mas (Fig. 3.3). Since no high resolution map of the H_2O masers of this source is available, the spatial distribution of the OH maser features with respect to H_2O masers is not clear in this source. Additionally, we do not have information on the orientation of the jet from the plane of the sky. Therefore, we can not easily distinguish between the equatorial or biconical outflow scenarios for the OH maser region of this source.

However, the OH maser spectrum of this source shows double peaks, but each peak is a blend of several maser lines. This could raise two possibilities. These peaks could originate from several maser spots with different velocities. Alternatively, geometric effects can produce this profile struc-

ture. Our calculations show that multiple peaks in the spectra may form in both biconical outflow and equatorial distribution; for example Fig. 3.11 and Fig. 3.13.

3.5   Discussions

Our observations reveal that the OH maser region of the three water-fountain sources studied in this work show signs of non-spherical expansion. This morphology can not be explained by the standard spherically expanding shell model for the OH maser shells in evolved stars. The dynamical ages of the H_2O maser jets of W43A and OH 12.8-0.9 are 90 and 50 yr , respectively (Boboltz & Marvel 2007, Imai et al. 2005). We measured a shell size of >1600 AU and the expansion velocity of <15 km s^{-1} for the OH masers. This implies the dynamical time scale of ~506 yr. This indicates that the OH maser region is significantly older compared to the H_2O maser jet. Therefore, the collimating agent was likely already at work before the H_2O maser jet was launched. No H_2O maser image of OH 37.1-0.8 is available. Therefore we can not confirm whether the jet is older that the OH maser shell in this star. Alternatively, the observed asymmetry may not reflect an actual asymmetry in the distribution, but rather other effects such as anisotropic pumping.

Recent observations have shown that magnetic fields could have an important role in collimating the H_2O maser jets in water-fountain sources. Vlemmings et al. (2006) show that the H_2O maser jet of W43A is magnetically collimated. The bipolar H_2O masers, can be explained by the dynamo-driven magnetic field. Blackman et al. (2001) showed that a single star model can produce magnetic driven dynamo in the AGB phase. However, since magnetic field drains rotational energy, it needs to be reseeded. A binary companion can maintain the differential rotation required during the lifetime of the AGB phase. In the presence of a binary companion, the in-spiral of the companion into the envelope produces rotational energy needed for the generation of the magnetic field (Nordhaus & Blackman 2006).

Magnetic fields could also have an important role on the non-spherical shape of the OH masers in water-fountain sources. From our MERLIN observations, we measured a magnetic field of ~430 μG and ~230 μG for blue shifted and red shifted masers of OH 37.1-0.8, respectively. These values are approximately an order of magnitude larger than those measured for the OH maser features of OH 12.8-0.9 (~27 μG and ~-31 μG for the blue-shifted and red-shifted regions, respectively). Previous MERLIN observations of the OH masers of W43A also revealed a field strength of 100 μG (A10), which indicates that a large scale magnetic field is present in the circumstellar environment of this object. A10 discussed several non-Zeeman effects which could produce the observed circular polarization. These effects include observational and instrumental effects. However, they did not find any effects which could falsely be attributed to the Zeeman splitting. This implies that the circular polarization observed in the OH masers originates from the Zeeman splitting

The fact that the field strength measured for OH 37.1-0.8 is almost an order of magnitude larger than that for OH 12.8-0.9 could imply that the OH maser region of OH 37.1-0.8 is located at a smaller distance to the central star than that of OH 12.8-0.9. As shown in Fig. 3.1 and Fig. 3.3, the maximum extent of the OH maser region of OH37.1-0.8 is ~200 mas, which is ~2.5 times smaller than the OH maser region of OH 12.8-0.9 (~500 mas). The magnetic field strength changes as a function of distance from the central star (Vlemmings et al. 2005, Fig. 6). The dipole field has r^{-3} dependence and the solar type field has r^{-2} dependence, where r is the distance from the central star. The distance to these stars is poorly known. However, considering the maximum extent of the

OH maser region of these objects, it could be due to the difference in size of the OH maser shell that we measure different field strengths. Therefore, depending on the magnetic field morphology, the field strength in the OH maser region of OH 37.1-0.8 could be higher than that of OH 12.8-0.9 by up to an order of magnitude.

We performed geometrical reconstruction in order to clarify the morphology of the OH maser region in water-fountain sources. We have studied the effects of many different parameters including the spectral shape, velocity field and the equatorial or biconical morphology. Our analyses show that the OH maser spots of W43A are likely located in the equatorial region of the circumstellar shell, while in OH 12.8-0.9 the OH masers are likely found in a biconical outflow surrounding the H_2O maser jet. The equatorial enhancement could be produced by the presence of a binary companion close to the CSE via common envelope (CE) evolution (Nordhaus & Blackman 2006). Under certain conditions the Roche lobe overflow, in a binary system may result in both companions immersed in a CE (Paczynski 1976). Numerical simulations showed that a binary induced equatorial outflow is confined to opening angles of 20°-30° (Terman & Taam 1996).

Although the binary companion could explain the equatorial enhancement, at the same time it may destroy the maser action. Schwarz et al. (1995) performed statistical analysis for a limited sample of symbiotics, most of them containing Mira variables as primaries. Their analysis showed that for very wide systems (R $\geq$ 50 AU), all masers (OH, H_2O and SiO) can operate. At intermediate orbits (10 AU$\leq$ R $\leq$ 50 AU) SiO and H_2O but not OH masers can survive. For much closer orbits (R $\leq$ 10 AU) no maser operates. The absence of masers in the close binary systems may be explained by the tidal effects from the secondary on the maser regions. Therefore, in water-fountain sources which show OH and sometimes SiO maser activity, the orbital separation is wide enough, that the masers are not affected by the companion (Deacon et al. 2007). Alternatively, the companion may already be swept up by the primary and does not influence the maser regions which occur at much larger distances from the central star.

3.6   Conclusions

The observations show that the OH masers in water-fountain sources are located in a-spherical shells. We performed geometrical reconstruction in order to understand the morphology of the OH masers. The comparison between the observations and models show that the OH masers of W43A are likely located in the equatorial region of the circumstellar shell, while in OH 12.8-0.9 the OH masers stem from a biconical outflow surrounding the H_2O maser jet. We measured significant magnetic fields for the OH maser region of OH 12.8-0.9 and OH 37.1-0.8. This shows the possible role of the magnetic field in shaping the circumstellar envelope of these stars.

Acknowledgements
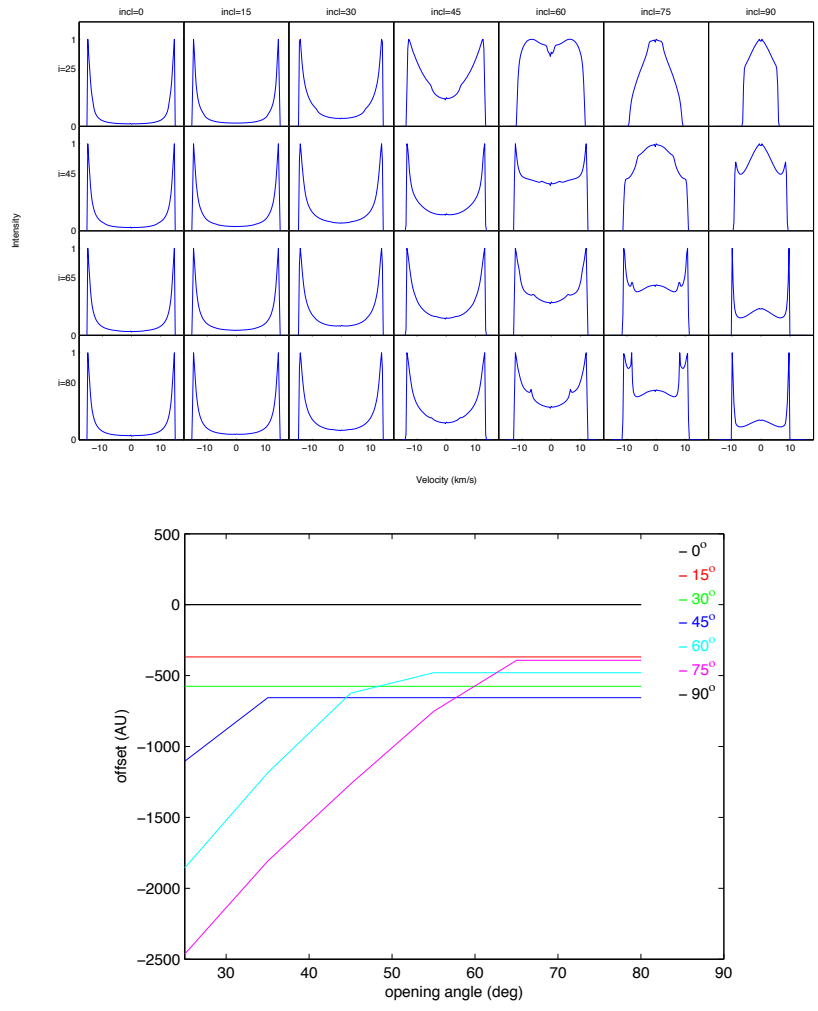
Figure 3.8 – As in Fig. 3.6, model calculations for the oblate ellipsoid $e = 0.7$ with equatorial distribution, where the velocity in the equatorial region is twice that in the polar axis.

Figure 3.9 – As in Fig. 3.6, model calculations for the oblate ellipsoid ($e = 0.9$) with equatorial distribution,where the velocity in the equatorial region is four times higher than that in the polar axis.

Figure 3.10 – As in Fig. 3.6, model calculations for the prolate ellipsoid ($e = 0.7$) with equatorial
distribution, where the velocity in the polar axis is twice than that in the equatorial plane.

Figure 3.11 – As in Fig. 3.6, model calculations for the prolate ellipsoid ($e = 0.9$) with equatorial distribution, where the velocity in the polar axis is four times higher than that in the equatorial plane.

57
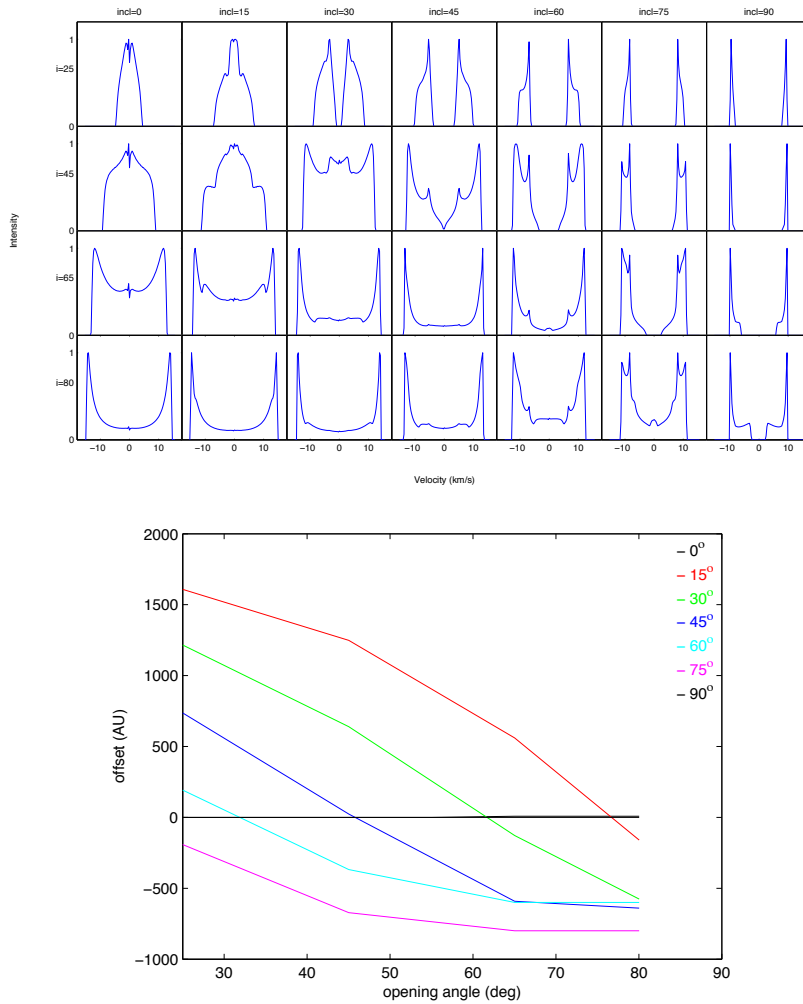
Figure 3.12 – As in Fig. 3.7, model calculations for the oblate ellipsoid (e = 0.7) with biconical
distribution, where the outflow velocity increases towards the equatorial plane.
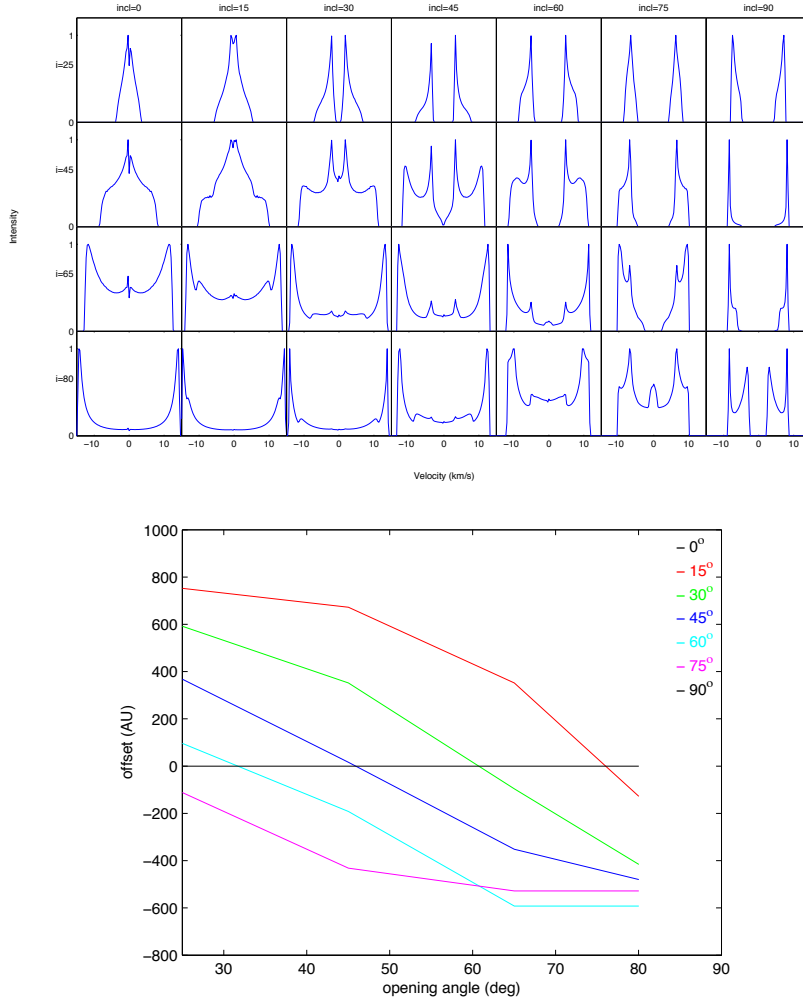
Figure 3.13 – As in Fig. 3.7, model calculations for the oblate ellipsoid ($e = 0.9$) with biconical distribution, where the outflow velocity increases towards the equatorial plane.
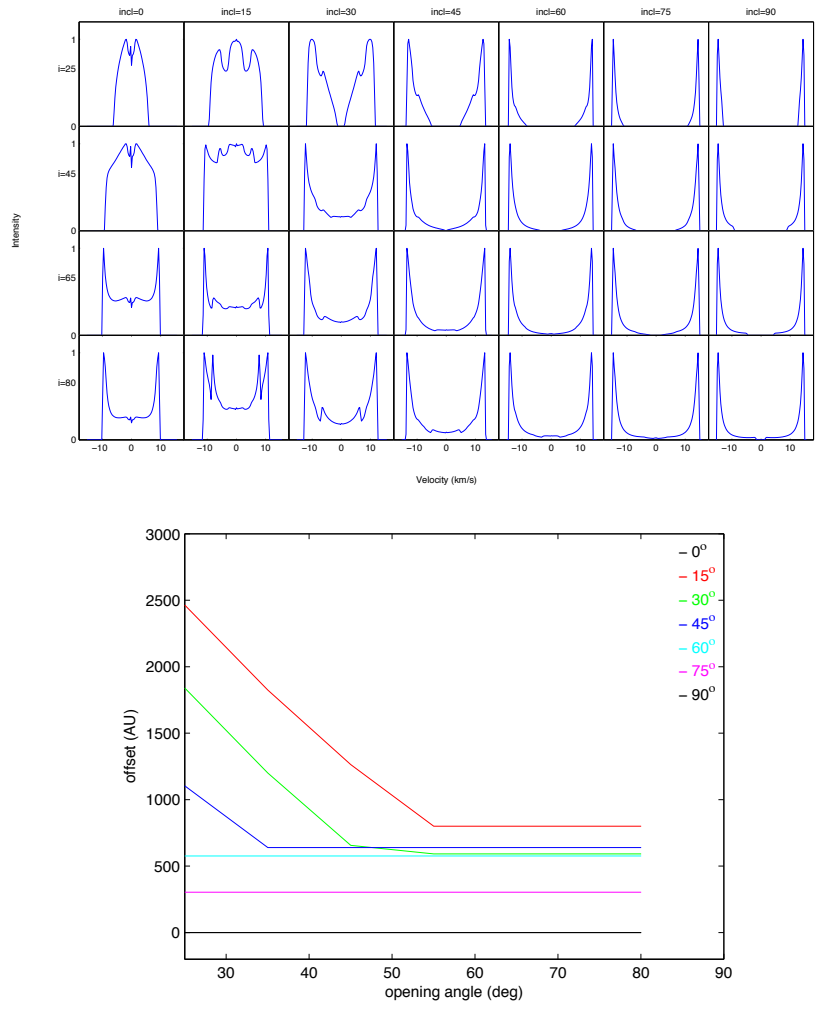
Figure 3.14 – As in Fig. 3.7, model calculations for the prolate ellipsoid (*e* = 0.7) with biconical distribution, where the outflow velocity increases towards the polar region.

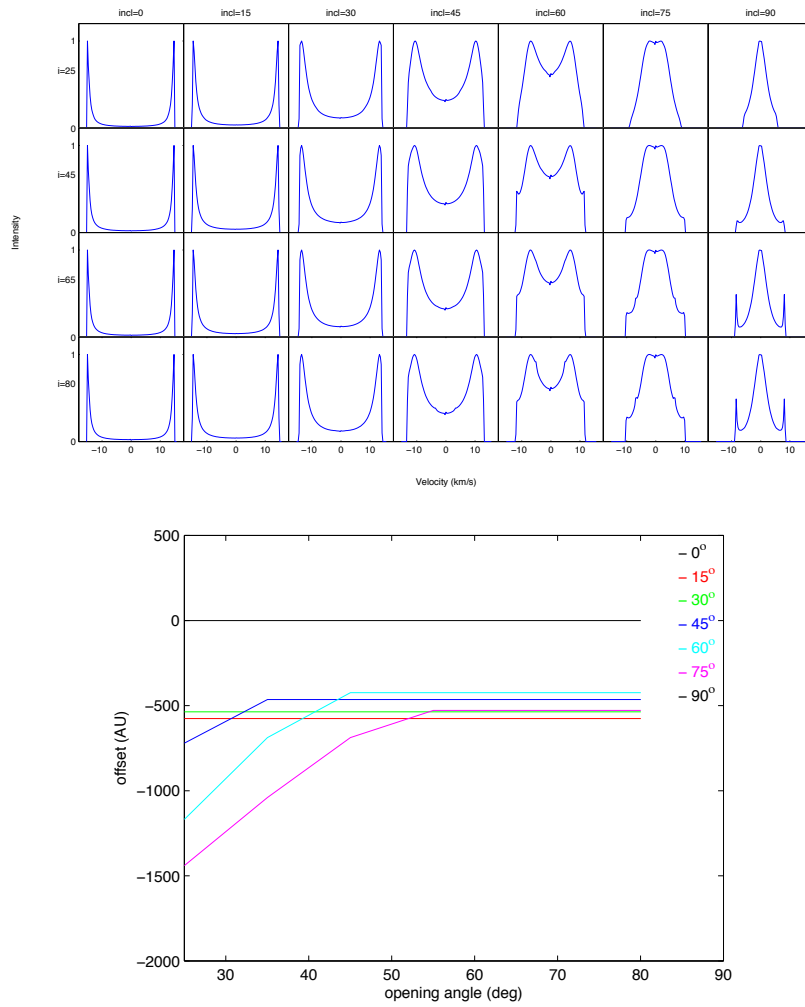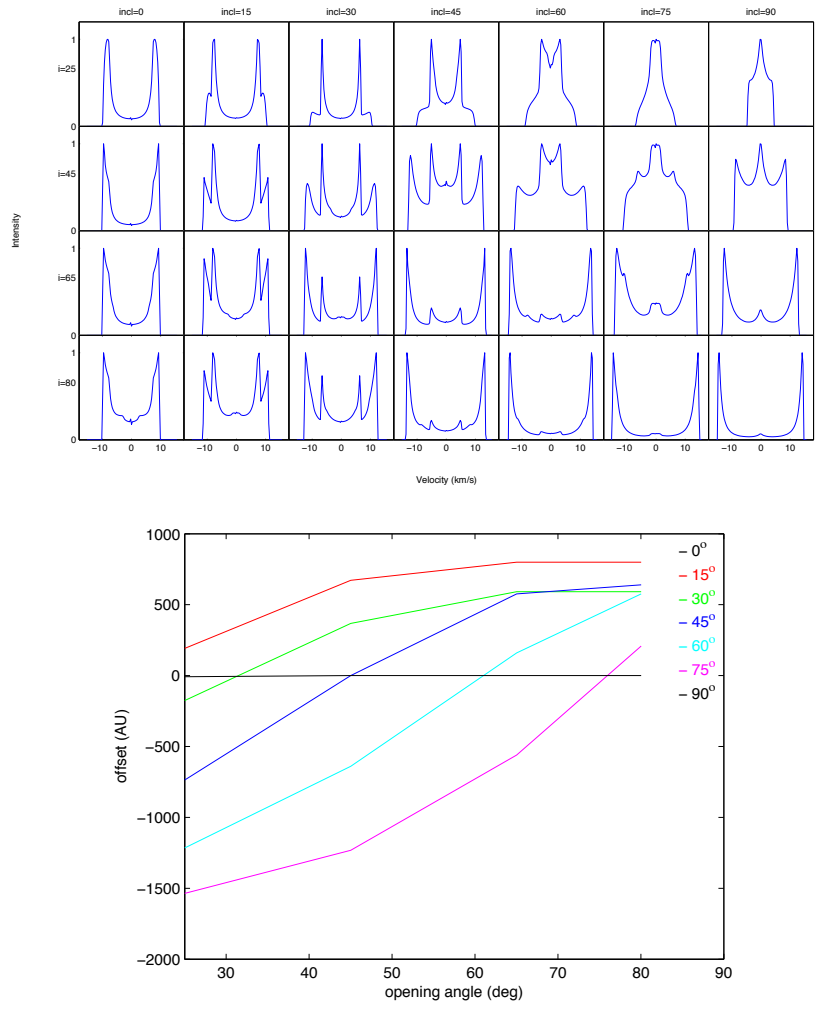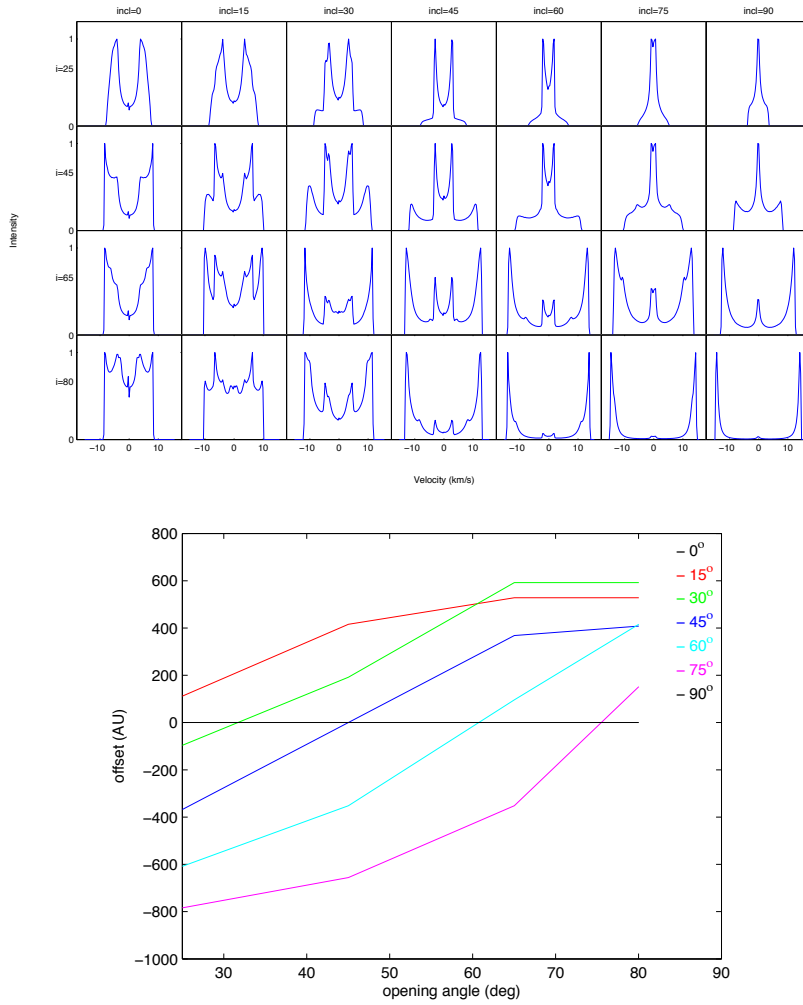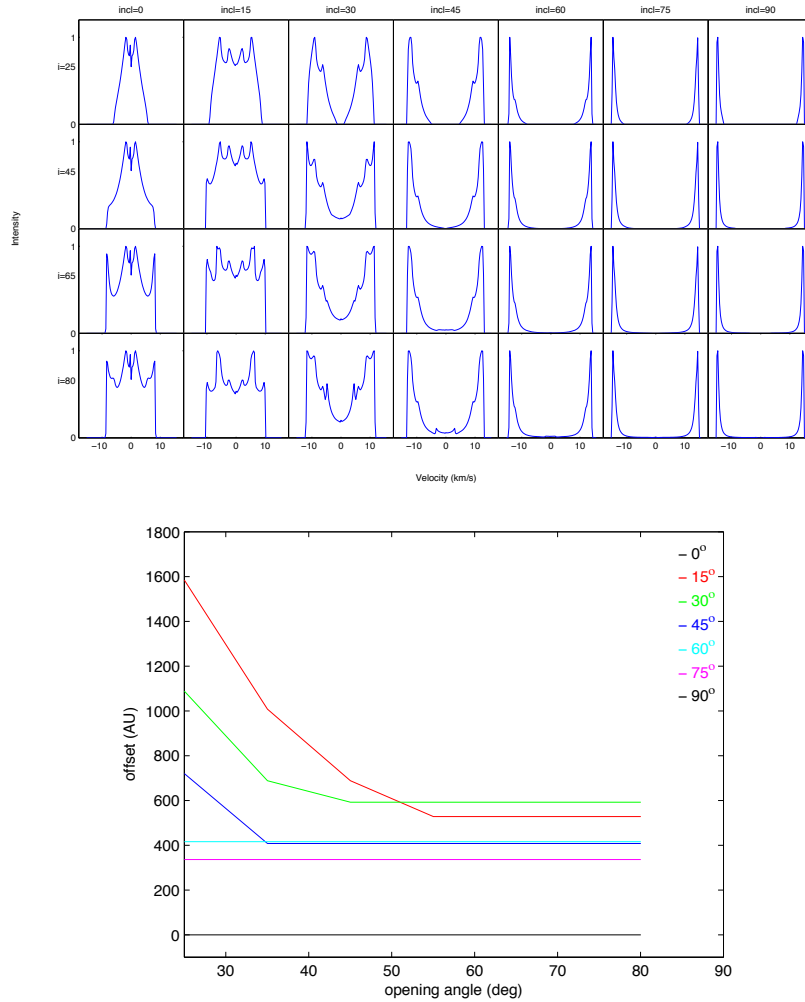**Figure 3.15** – As in Fig. 3.7, model calculations for the prolate ellipsoid ($e = 0.9$) with biconical distribution, where the outflow velocity increases towards the polar region.

Green Bank Telescope Observations of the H$_2$O masers of evolved stars: magnetic field and maser polarization

N. Amiri, W. H. T. Vlemmings, H. J. van Langevelde
Submitted to Astronomy & Astrophysics

63

Abstract

Magnetic fields potentially play an important role in shaping the circumstellar envelopes of evolved stars. The measurement of the Zeeman splitting through circular polarization observations of maser species constitutes the most direct way to determine magnetic field strength at various distances to the central evolved stars. H_2O masers typically occur between 10-100 AU from the star and the circular polarization of the masers is shown to stem from the Zeeman effect. So far significant magnetic field strengths were measured in the H_2O maser regions of Mira variable stars and supergiant stars as well as in the bipolar outflow of post-AGB objects. We like to extend the previous H_2O maser circular polarization studies and observe more evolved stars with different mass loss rates using single dish observations in order to be able to probe also the weaker maser sources. The 22 GHz H_2O maser observations were performed with the Green Bank telescope in full polarization spectral line mode. The Zeeman splitting was measured by cross correlating the right circular polarization and the left circular polarization spectra. We determined the magnetic field strength by applying the Zeeman splitting coefficient to the measured Zeeman splitting. We measured a magnetic field of 18.9 ± 3.8 mG for the H_2O maser region of the OH/IR star IRAS 19422+3506. The field strength is significantly lower than those measured for Mira variables. For the rest of the sources in our sample we place a 3σ upper limit in the range 10-800 mG. Specifically the ∼10 mG limit on the field of R LMi is significant, considering this is the lowest limit thus far determined in the H_2O maser region of an evolved star. Additionally, we measure significant variation in the peak flux density of up to two orders of magnitude compared to previous observations. In particular, the appearance of the double peak profile of IRAS 19422+3506 could indicate a bipolar H_2O maser outflow in this star. Our observations seem to indicate the possible role of magnetic field in shaping the circumstellar envelope of the OH/IR star IRAS 19422+3506. Finally, the H_2O masers show significant variability in flux density which could imply periodic variation in density and / or the velocity field of the circumstellar envelope.

4.1 Introduction

Low mass stars ($M \sim 8 - 10\ M_\odot$) undergo a period of high mass loss at the end of their evolution while climbing the Asymptotic Giant Branch (AGB). This outflow forms circumstellar envelops (CSEs), in which several maser species occur at different distances from the central star. Observations indicate that the CSE of AGB stars is generally spherically symmetric (Griffin 2004). However, planetary nebulae (PNe), supposedly formed from the ejected outer envelope of evolved stars, often show elliptical or bipolar morphologies (e.g. Manchado et al. 2000). It is not clear how the spherically symmetric mass loss changes to produce the aspherical PNe. The formation of aspherical PNe has been explained by the interacting stellar wind model (e.g. Balick et al. 1987). In this scenario, a fast wind ($\sim$1000 km s^{-1}) interacts with the older, slow AGB wind. Hubble Space Telescope (HST) observations of a sample of young PNe and proto-PNe revealed collimated jets (Sahai & Trauger 1998, Sahai et al. 2007). The precession of the jets is thought to be responsible for the formation of asymmetric PNe.

Magnetic fields can play an important role in shaping the circumstellar envelope (CSE) of evolved stars and can produce asymmetries during the transition from a spherically symmetric star into an aspherical PNe. They are also possible agents for collimating the jets around these sources (e.g. García-Segura et al. 2005). Polarization observations of different maser species can reveal the strength and morphology of the magnetic field at different regions of the CSEs. In the high temperature and density regime close to the central star (5-10 AU), SiO masers occur. Polarimetric observations of SiO masers indicate field strengths of order 3.5 G, assuming the standard Zeeman interpretation for the observed circular polarization (e.g. Kemball & Diamond 1997, Herpin et al. 2006, ;Amiri et al. 2011, submitted). However, a non-Zeeman interpretation was introduced by (Wiebe & Watson 1998), according to which the observed circular polarization of the SiO masers can be explained by fields of $\sim$30 mG. OH masers occur much further out in the CSEs and probe low temperatures and densities. Polarimetry observations of these masers have revealed large scale magnetic fields with a strength ranging from 0.1 mG to 10 mG (e.g. Etoka & Diamond 2004, Amiri et al. 2010).

H_2O masers are found at intermediate distances to the central star (a few hundred AU) and probe a higher density and temperature than the OH masers. The circular polarization of the masers was shown to be due to the Zeeman splitting (e.g. Vlemmings et al. 2002). Therefore, until the uncertainty on the SiO maser polarization interpretation is solved, only H_2O masers can accurately measure the field strength at distances close to the central stars. Recent VLBA polarization observations of H_2O masers revealed significant field strength for Mira variables and supergiants in the range 0.2 G to 4 G (Vlemmings et al. 2002, 2005). In addition, the H_2O maser jet of the proto-PNe W43A was shown to be magnetically collimated with a field strength of 80 mG (Vlemmings et al. 2006).

The origin of strong magnetic fields in the CSE of AGB stars remains a topic of debate. Magnetic fields in AGB stars can be produced by a dynamo. However, one of the arguments against a magnetic dynamo is the slow rotation of the AGB star due to the conservation of angular momentum in combination with the large expansion on the AGB. However, Blackman et al. (2001) showed that a single star model can produce magnetic driven dynamo in the AGB phase. Since magnetic field drains rotational energy, it needs to be reseeded. A binary companion can maintain the differential rotation required during the lifetime of the AGB phase. In the presence of a binary companion, the spiral-in of the companion into the envelope produces rotational energy needed for the generation of the magnetic field (Nordhaus & Blackman 2006).

In order to asses the role of the magnetic field throughout the AGB evolution, polarimetric observations of evolved stars with different mass loss rates are required. So far, significant field strengths are measured for Mira variables and supergiants. However, no systematic studies have been performed to measure the magnetic field strength in the inner parts of the CSE of OH/IR stars. These objects have larger and denser CSEs and much longer periods up to 2000 days compared to those of Mira variables (Herman & Habing 1985b). They are strong 1612 MHz OH maser emitters (Baud et al. 1979). The stars are surrounded by thick dust shells which makes them optically obscured.

In this work, we report the results of our H_2O maser polarimetric observations of a sample of evolved stars (including Mira variables and OH/IR stars) with the Green Bank telescope. The observations aim to measure the magnetic field strength in the H_2O maser region of a sample of evolved stars for the first time. Even though the single dish measurements are biased towards underestimating the magnetic field strength due to spectral blending, these observations will probe the overall field strength in stars with individual maser features too weak for VLBI.

The format of this paper is as follows: in Sec. 4.2 we present the observations. The Zeeman splitting theory for H_2O masers is briefly explained in Sec. 4.3. The results are given in Sec. 4.4. We discuss the interpretation of the observations in Sec. 4.5 and give conclusions in Sec. 4.6.

4.2   Observations

We performed the 22 GHz H_2O maser polarimetric observations of a sample of evolved stars with the Robert C. Byrd Green Bank Telescope (GBT) of the NRAO [1] on 22 April 2010. At 22 GHz the Full Width Half Maximum of the GBT is 30″. The GBT spectrometer was used with a bandwidth of 12.5 MHz and 4096 spectral channels, which provides a channel spacing of 0.04 km s^{-1} and a total velocity coverage of 170 km s^{-1}. We used the K-band receiver for the frequency range (18-24 GHz). The receiver has two beams, each producing two polarization channels. We observed the sample using a beam switching mode with beam throws of 8′. As a result, one beam was always looking at the source, while the other beam was used for baseline correction. The cycle time of 2 min was sufficient to compensate for atmospheric fluctuations.The total observing time was 6 hours including pointing and focusing observations. The on-source observing time for R LMi, RX Oph, V1416 Aql was 44, 42 and 8 minutes. For IRAS 17230+0113, IRAS 19422+3506 and IRAS 19579+3223 the on-source observing time was 36, 76 and 16 minutes. Although all sources were initially selected based on published observations, to be strong enough for a magnetic field detection, most sources were found to be variable. Sources of which the masers turned out to be weak in real time inspection, were cut short in favor of the stronger masers. The system temperature of the GBT was in the range 35-50 K during the observations. The rms noise in the emission free channels was in the range $\sim$ 8-17 mJy throughout our observations, with the exception of the rms noise of ~50 mJy V1416 Aql due to the short integration time on this source.The GBTIDL [2] software package was used for the data reduction and analysis. Baseline variation due to atmospheric and instrumental effects was determined and subtracted using the spectral channels free of any maser emission.

4.3 Zeeman Splitting of H$_2$O masers

The $(6_{16} - 5_{23})$ H$_2$O maser transition at 22.23508 GHz occurs ~600 K above the ground state. This transition consists of six hyperfine components (e.g. Walker 1984). In the presence of an external magnetic field, each hyperfine component will split into 3 groups of lines ($\sigma^\pm$, π). The π transitions produce emission linearly polarized along the external magnetic field. If the magnetic field has a component parallel to the line of sight, the $\sigma^\pm$ components appear in the right circular polarization (RCP) and the left circular polarization (LCP) respectively. The RCP and LCP spectra are slightly shifted in frequency with respect to each other. This frequency splitting corresponds to the Zeeman effect. Since the H$_2$O molecule is non-paramagnetic, the Zeeman splitting is very small and on the order of 10^{-3} of the maser line width (~1 km s^{-1}).

We use the RCP-LCP cross-correlation method introduced by Modjaz et al. (2005) to measure the Zeeman splitting and the magnetic field. This method is able to measure the Zeeman splitting in the case of spectrally blended features of non-paramagnetic molecules, assuming the magnetic field is constant across the spectrum. Cross correlating the RCP and LCP spectra yields the velocity separation (q) due to the Zeeman splitting, which is related to the magnetic field strength along the line of sight:

$$B_{\parallel} = \frac{q}{\sqrt{2} \, A_{F-F'}} \tag{4.1}$$

Where the A$_{F-F'}$ coefficient depends on the hyperfine component. The value of the coefficient can be determined from the non-LTE analysis which includes consideration of narrowing and re-broadening of the maser line as a result of maser saturation and unequal population of the magnetic sub-levels. This implies A$_{F-F'}$=0.02 km s^{-1} G^{-1} as the merging of the three hyperfine components for H$_2$O masers (Vlemmings et al. 2002). The cross-correlation method was shown to be robust against the relative RCP and LCP gain calibration errors. The sensitivity of this method is comparable to the traditional S-curve method, where the stokes V spectrum is directly used to measure the magnetic field.

4.3.1 Non-Zeeman effects

There are potentially non-Zeeman mechanisms prohibit one to interpret circular polarization as a measure of the magnetic field strength. The first one stems from the competition between the stimulated emission rate (R), the Zeeman coefficient rate (gΩ) and the radiative decay rate (Γ). Following the analysis of (Vlemmings et al. 2002) we rule out the non-Zeeman mechanism proposed by (Nedoluha & Watson 1990), in which the preferred direction of the radiation imposes a circular polarization.

Wiebe & Watson (1998) introduce yet another non-Zeeman effect in which the propagation of a strong linear polarization can create circular polarization if the condition $g\Omega \gg R \gg \Gamma$ is satisfied. The circular polarization can be generated if the magnetic field orientation changes along the maser propagation direction. The circular polarization produced from this scenario is $\sim \frac{m_l^2}{4}$ where m_l indicates the linear polarization fraction. Vlemmings et al. (2002) show that since H$_2$O masers do not exhibit significant linear polarization, this effect is also unlikely.

67

4.4   Results

We observed a sample of six evolved stars, including three Mira variables and three OH/IR stars. Fig. 4.1 displays the observed spectra of the H_2O masers obtained from the observations. These objects were previously observed with the Effelsberg Telescope (Engels & Lewis 1996), and strong H_2O masers with flux densities in the range 11-160 Jy were measured for these stars. The results of the Zeeman splitting analysis using the RCP-LCP cross correlation method are given in Table 4.1. The table also shows the source name, variability type, position, central LSR velocity, peak flux density.

4.4.1   Individual sources

4.4.1.1   R LMi

This source is a Mira variable with a period of 372.19 days (Samus et al. 2009). The H_2O masers of this source were previously detected by Engels & Lewis (1996) with a maximum flux density of ~ 30 Jy close to the LSR velocity of the star (-0.8 km s^{-1}). Single dish observations of the SiO and H_2O masers of this star were performed by Kim et al. (2010), in which they measured peak flux densities of ~8 Jy and 112 Jy for H_2O and SiO masers of this star, respectively. Colomer et al. (2000) performed high resolution observations of the H_2O masers of this source with the VLA interferometer. Although the distribution of the maser spots suggested the existence of a ring-like structure, they were not able to fit a shell to the distribution of the maser spots.

From the observations, we measured a peak flux density of 17.3 Jy at -0.2 km s^{-1}. Comparison of the spectrum with the previous observations by Engels & Lewis (1996) shows that the overall morphology of the spectrum remains similar between the two observations. However, the peak flux density has decreased by almost a factor of two indicating the strong variability of the masers.

Single dish polarimetric observations of the OH masers of this source revealed a magnetic field of 2.32 mG (Rudnitski et al. 2010). Herpin et al. (2006) performed polarimetric observations of the SiO masers of this source with the IRAS 30m telescope and measured a field strength in the range 0-5.6 G, assuming the standard Zeeman interpretation hypothesis. However, we did not measure a significant magnetic field through cross correlation method, instead we place a 3σ upper limit of 10.8 mG for the H_2O maser region of this star.

4.4.2   RX Oph

This source is a Mira variable with a period of 322.93 days (Samus et al. 2009). The OH masers of this star were previously detected by Lewis (1997). An attempt was made to observe the SiO masers of this object by Nyman et al. (1986), but no detection was reported. Engels & Lewis (1996) observed the H_2O masers of this star and measured a spectrum with a peak flux density of ~47 Jy at -47.8 km s^{-1}. However, the single dish observations of this sources by Shintani et al. (2008) did not result in any detection. Our observations indicate that the H_2O masers of this source occur close to the stellar velocity (-47.8 km s^{-1}) with a peak flux density of ~ 0.7 Jy. The observed flux density has decreased by a factor of ~ 70 compared to the previous observations by Engels & Lewis (1996). Furthermore, we did not measure a significant Zeeman splitting through cross correlating the RCP

Table 4.1 – The Zeeman splitting results.

source	Type	R.A. J2000	Dec. J2000	V_{rad} km s^{-1}	Peak flux Jy	B mG
R LMi	Mira	09 45 34.28	+34 30 42.77	-0.8	17.3	< 10.8
RX Oph	Mira	16 52 48.2	+05 24 27	-47.8	0.7	<800
V1416 Aql	Mira	20 07 43.1	+06 03 11	-69.5	0.7	-
IRAS 17230+0113	OH/IR	17 25 36.6	+01 11 05	-24.5	1	<198
IRAS 19422+3506	OH/IR	19 44 07.0	+35 14 08	-60	12.4	18.9± 3.8
IRAS 19579+3223	OH/IR	19 59 51.32	+32 32 09.8	4.1	3	< 98
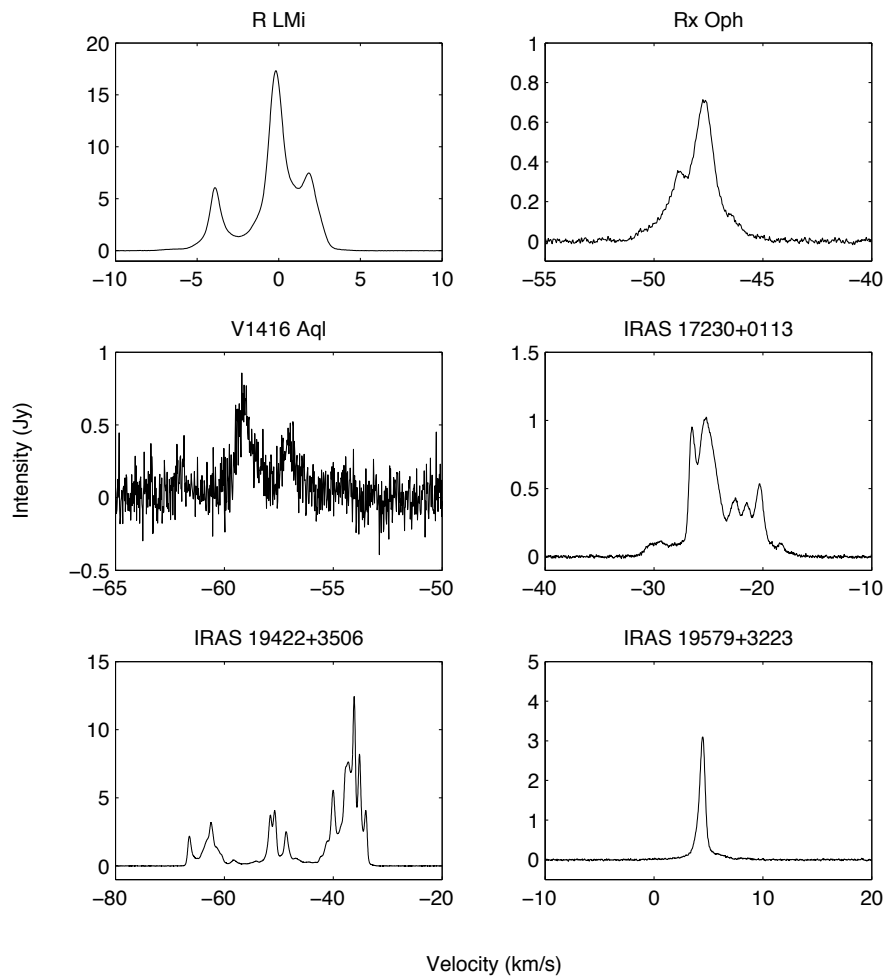
Figure 4.1 – The 22 GHz H$_2$O maser spectra of a sample of evolved stars obtained from the GBT observations.

and LCP spectra. Instead, we place a 3σ upper limit of ~800 mG for the H_2O maser region of this star.

4.4.3   V1416 Aql

This source is known as a Mira variable. The H_2O masers of this source were previously measured by Engels & Lewis (1996) with a flux density of 120 Jy. However, this source was not detected in single dish monitoring with the VERA telescope (Shintani et al. 2008). Our observations indicate a double peak profile with a maximum flux density of ~0.7 Jy for the H_2O masers of this source, which implies that the flux density is decreased about two orders of magnitude compared to the previous observations by Engels & Lewis (1996). This could indicate that Engels & Lewis (1996) observed this source during a flare. We note that due to the low signal to noise ratio, we were not able to perform the cross correlation method for this star.

4.4.4   IRAS 17230+0113

This object is known as an OH/IR star (Lewis 1997). The 1612 MHz OH masers of this star show a double peak profile (Lewis 1997). Previous 22 GHz H_2O maser observations of this star indicated multiple peaks close to the stellar velocity with a maximum flux density of ~12 Jy. Our observations show similar multiple peaks profile with a maximum flux density of 1 Jy. We note that we did not measure a significant magnetic field by cross-correlating the right and left circular polarization spectra and we only place an upper limit of the magnetic field at 3σ of 198 mG for the H_2O maser region of this star.

4.4.5   IRAS 19422+3506

This source is classified as a high mass loss OH/IR star (e.g. Lewis 1997) and exhibits SiO, OH and H_2O maser emission (Lewis 1997, Nakashima & Deguchi 2007, Engels & Lewis 1996). H_2O maser observations of this star showed a single peak profile with a peak flux density of 52 Jy at -60.9 km s^{-1} (Engels & Lewis 1996). Later, Nakashima & Deguchi (2007) performed simultaneous SiO and H_2O maser observations of this star. They measured peak flux densities for SiO and H_2O masers of 4.2 Jy at -48.9 km s^{-1} and ~9 Jy at -47 km s^{-1}, respectively. Shintani et al. (2008) also observed the H_2O maser of this star, but no detection was reported.

Our observations (Fig. 4.1) show that the H_2O masers of this source occur in three emission complexes with a peak flux density of 12.4 Jy. The spectrum shows a double peak profile together with the emission at the center close to the stellar velocity. There is a significant variation in spectral shape and peak flux density between our observations and those observed by Engels & Lewis (1996) and Nakashima & Deguchi (2007), in which only one peak was detected.

We performed cross-correlation for the blue-shifted and red-shifted emission as well as the central emission separately. A magnetic field of 18.9±3.8 mG was measured for the red-shifted region (-45 to -35 km s^{-1}). For the emission at the center of the spectrum and the blue-shifted region we did not measure a significant field strength, and the 3σ upper limits of 52 mG and 33 mG were determined for these two emission complexes. The field strength of 18.9±3.8 mG is between one and two

71

orders of magnitude lower than those measured for Mira variables and supergiants (Vlemmings et al. 2005).

4.4.6   IRAS 19579+3223

This star is classified as an OH/IR star (Lewis 1997). The 22 GHz observations of this star by Engels & Lewis (1996) indicated emission with multiple peaks close to the stellar velocity with a maximum flux density of 10.3 Jy. From our observations we measure a spectrum with a single peak with a flux density of ~3 Jy at 4 km s^{-1}. This implies that the spectrum shows significant variation in spectral shape and the peak flux density.

We did not measure a significant magnetic field strength in the H_2O maser region of this star. Instead we place an upper limit of ~98 mG at 3σ level.

4.5   Discussion

4.5.1   Magnetic field

The aim of this work is to expand the previous studies to measure the magnetic field strength through circular polarization observations of maser species in the CSEs of evolved stars. Recent observations revealed significant magnetic field strength at different regions of the CSEs. At the inner region of the CSEs, SiO maser polarimetric observations indicate magnetic fields of ~3.5 G (Herpin et al. 2006, Kemball & Diamond 1997). Moreover, the polarimetric observations of OH masers which occur at the outer part of the CSEs show field strength in the range 0.1-10 mG (Etoka & Diamond 2004, Amiri et al. 2010). This could imply that a large scale magnetic field is present in the circumstellar environment of evolved stars, something that so far has only been confirmed for the supergiant VX Sgr (Vlemmings et al. 2011).

We performed H_2O maser polarimetric observations of a sample of evolved stars including Mira variables and OH/IR stars which have higher mass loss rates. The observations show a magnetic field of 18.9±3.8 mG for the red-shifted emission of the OH/IR star IRAS 19422+3506. The measured field is of similar magnitude as the magnetic field in the bipolar H_2O maser outflow of the post-AGB star W43A (Vlemmings et al. 2006, Amiri et al. 2010). However, the observed field is between one and two orders of magnitude lower than the observed magnetic field of 0.2 to 4 G measured for the H_2O masers of Mira variables and supergiants (Vlemmings et al. 2002, 2005). Since IRAS 19422+3506 is a high mass loss OH/IR star, the CSE of this object is expected to be larger. Therefore, the lower field measured could imply that the H_2O masers are located at a larger distance from the central star compared to Mira variables. Polarimetric observations of all other maser species (OH, H_2O and SiO) are required to determine the magnetic field morphology in the CSE of evolved stars.

For the other sources in our sample we only place upper limits at 3σ level in the range 10-800 mG for the magnetic field strength in the H_2O maser region of the stars. In particular, while for R Lmi field strength of 2.32 mG and 0-5.6 G was measured for the OH and SiO maser regions (Rudnitski et al. 2010, Herpin et al. 2006), we did not measure a significant field strength for the H_2O masers of this star. However, blending of the maser features will decrease the observed magnetic field

strength with low angular resolution observations (Sarma et al. 2001). Interferometric observations of the H_2O masers of this star would help us to reveal if R Lmi indeed has a magnetic field strength significantly lower than those of other Miras.

4.5.1.1 The role of the magnetic field in shaping the circumstellar outflow

The role of the magnetic field in forming the aspherical PNe is discussed in the literature (e.g. Pascoli 1987). The interaction of a toroidal magnetic field (due to the stellar rotation) with the fast AGB wind can produce aspherical PNe (e.g. Chevalier & Luo 1994, Garcia-Segura 1997). Alternatively, Matt et al. (2000) propose another mechanism in which the interaction of a slow AGB wind with a dipole magnetic field of a few Gauss produces an equatorial disk. The interaction of the later fast AGB wind with the equatorial disk can produce aspherical, cylindrical PNe (e.g. Icke 1988). Moreover, under the influence of a strong magnetic field, the circumstellar disk can become warped (Lai 2003). The interaction of the fast AGB wind with the warped disk has been shown to produce multi polar PNe (Icke 2003). We are not able to determine the magnetic field morphology in the H_2O maser region from our single dish observations. However, Vlemmings et al. (2005) suggest a dipole field morphology for the H_2O maser region of the supergiant VX Sgr, the result which was recently confirmed by the high frequency SiO maser observations of this star (Vlemmings et al. 2011).

4.5.2 Variability

Our observations show that the H_2O masers of the evolved stars exhibit significant variability in flux density up to two orders of magnitude compared to the previous observations by Engels & Lewis (1996). Moreover, we are not witnessing a significant drift of the line of sight velocities of the maser components which could have indicated radial acceleration between the two observations. H_2O masers are known to be variable in flux and spectral shape (e.g. Bowers et al. 1993, Engels & Lewis 1996). The flux density may vary by 2 orders of magnitude and occasional flares by up to a factor of 1000 variation in flux are reported (Schwartz et al. 1974). H_2O masers are located in a region where shock waves driven by stellar pulsation are propagating through the H_2O maser zone (Rudnitskii & Chuprikov 1990, Shintani et al. 2008). Moreover, the strong variability likely indicate the masers are unsaturated and that they respond exponentially to the variation in excitation conditions in the maser region (Engels & Lewis 1996).

In particular, the H_2O masers of IRAS 19422+3506 exhibit three emission complexes in the spectrum, in contrast to the single peak profile observed previously by Engels & Lewis (1996). The variation in spectral shape could indicate that we are witnessing a transitory effect in this star. The double peak profile raises the possibility that the outer peaks occur at the tips of a jet that lies not too far to the plane of the sky. The inner components could indicate that the masers occur in the equatorial plane of the circumstellar shell (Walsh et al. 2009). We note that H_2O maser jets are already observed in several post AGB objects (e.g. Imai et al. 2002, Boboltz & Marvel 2005). In particular, VLBA H_2O maser observations of W43A revealed a collimated H_2O maser jet (Imai et al. 2002). Alternatively, the double peak profile may indicate the radial amplification of the masers. Since this object is an OH/IR star, the water maser shell is expected to be larger and located at much larger distances from the central star compared to the location of H_2O masers in Mira variables. At such large distances, there is a lower velocity gradient which allows the radial amplification of

masers which manifest itself as a double peak profile (Engels & Lewis 1996). Therefore, VLBI observations of this source are required to disentangle the morphology of the H_2O maser region of this source.

4.6   Conclusion
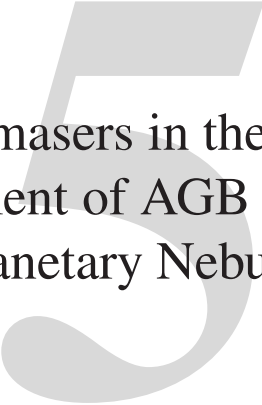
We performed polarimetric observations of the H_2O masers of a sample of evolved stars including Mira variables and OH/IR stars with the GBT. While, significant field strength of 0.2-4 G was measured previously for Mira variables and supergiants, we only measured a magnetic field of 18.9±3.8 mG for the red-shifted emission of the OH/IR star IRAS 19422+3506. However, this field strength was similar to the field of ~30 mG measured for the blue-shifted lobe of the H_2O maser jet of the post-AGB object W43A. For the rest of the sample we only place upper limits in the range 10-800 mG.

Additionally, our observations show that H_2O masers show significant variability in flux density up to two orders of magnitude compared to previous observations by Engels & Lewis (1996). This could imply significant variation in density and velocity of the H_2O maser region of the CSE of these stars.

Follow up monitoring observations of the H_2O masers of the evolved stars studied in this work are essential to study the variability of the masers in different classes of evolved stars. Furthermore, polarimetric H_2O maser observations for a larger sample of evolved stars with different mass loss rates are necessary to determine the role of the magnetic field throughout the AGB evolution.

Acknowledgements

The evolution of H_2O masers in the circumstellar environment of AGB stars in transition to Planetary Nebulae

N. Amiri, W. H. T. Vlemmings, H. J. van Langevelde
In preparation

Abstract

Observations have shown bipolar H_2O maser outflows in a class of post-AGB candidates, the so-called water fountain sources. Additionally, observations have established a significant correlation between the variability in flux density and profile shape with the stellar pulsation in Mira variables. However, it is not clear whether the H_2O masers exhibit similar variability behavior in higher mass loss AGB stars and in particular stars approaching the end of the AGB phase. The aim of this paper is to search for water-fountain sources in post-AGB candidates. A statistically relevant sample of these important transition objects is essential to study the evolution from spherically symmetric AGB stars to aspherical planetary nebulae. By observing in multi-epochs, we can also study the variability of the masers and compare them with those of Mira variables. We performed H_2O maser observations of a sample of 74 post-AGB candidates with the Effelsberg Telescope with a large velocity coverage (~1363 km s^{-1}). The observations were done at three epochs, spanning a timescale of ~500 days. Additionally we observed the OH masers of the supposedly dead OH/IR star, IRAS 18455+0448, after we noticed the return of the H_2O masers, to check whether the OH masers are also back. We identified six water fountain candidates which show double peak profiles in at least one epoch. In particular, we detected the H_2O masers of a supposedly dead OH/IR star IRAS 18455+0448. Additionally, we found significant variability in flux density and spectral profile for the H_2O masers in our sample. Comparison of our observations with the observations of the same source sample performed ~20 years ago by Engels & Lewis (1996) indicate the disappearance of 10 masers and the appearance of three new masers among a sample of 74 sources. Furthermore, the observations likely indicate a good correlation between the stellar pulsation and the H_2O maser variability. Furthermore, we estimate a lifetime of ~60 years for the H_2O masers in the post-AGB phase. We identified potential water fountain candidates. Interferometric observations of the H_2O masers of these stars are essential to clarify this. In particular, if the bipolar scenario for the H_2O masers of IRAS 18455+0448 is confirmed, this star will be the youngest proto-PNe identified to date. Furthermore, the observations likely indicate a relation between the H_2O maser variability and pulsation cycle, as was previously found for Mira variables.

5.1 Introduction

The Asymptotic Giant Branch (AGB) phase is one of the last stages of stellar evolution for low to intermediate mass stars (1-8 $M_\odot$). At this stage, stars eject a significant amount of their mass into the interstellar medium in the form of stellar winds. The outflow from these objects forms Circumstellar Envelopes (CSEs) which harbor several molecular species. Among the best probes of evolved star mass-loss, outflow history and morphology are the masers that occur in different regions of the CSEs, as they probe the dynamics and kinematics of the outflow at various distances to the central stars. In the picture of regular AGB stars, SiO masers occur close to the central star (e.g. Cotton et al. 2008), while the H_2O and OH masers are found at progressively further distances (e.g. Habing 1996). The OH masers often exhibit double-peaked profiles with their velocities covering up to ~ 25 km s^{-1} (e.g. te Lintel Hekkert et al. 1989), while the H_2O maser spectra are typically more irregular and have a velocity range confined within the OH maser spectrum (e.g. Bains et al. 2003).

Observations indicate that the majority of the observed PNe exhibit a range of complex morphologies (e.g. Balick et al. 1987), whereas their progenitor AGB stars are generally observed to be spherically symmetric. This implies that at some stage during the transition from the AGB phase to PNe, the spherically symmetric outflow changes to produce a-spherical PNe. A class of post-AGB objects have been discovered, which exhibit highly collimated H_2O maser jets (Likkel et al. 1992). The observed spectra and spatial distribution of these so-called water fountain sources are not consistent with those of regular AGB stars. The H_2O maser velocity range (~ 200 km s^{-1} or more) is much larger than the OH masers in these stars (e.g. Imai et al. 2008). Very Long Baseline Interferometry (VLBI) observations reveal collimated H_2O maser outflows in these stars (e.g. Imai et al. 2002, Boboltz & Marvel 2005). The dynamical ages of the water fountain jets studied at high-resolution range from few to a few hundred years, which has led to the conclusion that they represent a short transition phase between (post-)AGB and PN phase (Boboltz & Marvel 2007). The bipolar jets observed in water fountain sources are expected to be one of the major factors in shaping PNe, based on the existence of a large number of PNe with bipolar or multipolar morphologies (Sahai & Trauger 1998). This could indicate that during the post-AGB phase the jets carve out the CSEs and leave an imprint which manifests itself as asymmetric PNe at the later stage in the AGB evolution.

At the same time, the circumstellar masers, in particular H_2O masers, exhibit significant variability in spectral shape and flux density. H_2O maser monitoring observations of a sample of Mira variables reveal that the variability of the masers is related to the pulsation of the central star as well as the changes in the physical conditions in the interstellar medium (Rudnitskii & Chuprikov 1990, Shintani et al. 2008). However, it is not clear how the intensity and spectral profile of the H_2O masers vary for higher mass loss OH/IR stars and AGB stars approaching the end of the AGB phase. OH/IR stars are the extension of Mira variables towards larger masses and longer periods (up to 2000 days) and the CSEs of these stars are expected to be denser and larger (e.g. Herman & Habing 1985a).

In this paper, we present multi-epoch H_2O maser observations of a sample of post-AGB candidates with the Effelsberg Telescope. The primary goal of the observations is to identify water fountain candidates. Due to their short lived transition between the AGB and proto-PNe phase, only a handful of water-fountain candidates have been identified (e.g. Imai et al. 2007). However, a statistically relevant sample is important for our studies of the transition from spherically symmetric circumstellar envelopes into elliptical or even bipolar shapes of PNe. Additionally, the observations enable us to explore the variability behavior of H_2O masers in higher mass loss AGB stars and post-AGB

objects and compare them with those of Mira variables.

5.2 Observations and Data Reduction

We selected a sample of 74 evolved stars which are likely late AGB or early post-AGB objects (Table 5.3). All of these objects were previously observed with the Effelsberg telescope in an attempt to detect their H_2O maser emission (Engels & Lewis 1996). The sources were selected based on their location in the IRAS (60-25)/(25-12) color-color diagram (Fig. 5.1). The properties of the stars located in each region are shown in Table 5.1. Sources located in the regions IIIa, IIIb, IV, V are likely post-AGB candidates that have thick circumstellar shells and are likely undergoing a transition into PNe.

41 sources in our sample are objects for which no H_2O maser emission was detected in the earlier Effelsberg observations (Engels & Lewis 1996). The limited (~ 80 km s^{-1}) velocity coverage of the observations at the time could have failed to detect water-fountains which show high velocity H_2O maser outflows. Alternatively, maser variability, insufficient sensitivity or jet masers that were yet to appear can explain the non-detections. H_2O masers were originally detected for the remaining 33 sources in our sample. Among them, we selected sources for which some of the H_2O maser components lie outside the OH maser range, making them water fountain candidates.

We performed 22.23508 GHz H_2O maser observations of the source sample with the Effelsberg telescope. The full width half maximum (FWHM) of the telescope is 40.2 arcsec at the maser frequency (~ 22 GHz). Using the FFT spectrometer with 16384 channels and a bandwidth of 100 MHz (~ 1363 km s^{-1}) centered at the stellar velocity, the resulting spectral resolution is 0.08 km s^{-1}. The velocity coverage is much larger than that obtained in the previous observations of the source sample by Engels & Lewis (1996) (~ 80 km s^{-1}), which potentially could have missed to detect high velocity H_2O masers of water fountain sources.

The observations were performed in three epochs : 12 and 13 November 2009, 22 and 23 March 2011 and 14 April 2011. For the first two epochs we used the 1.3 cm primary beam receiver in spectral line mode. The 1.3 cm secondary VLBI receiver was used for the third epoch observations. The observations were made in position switching mode with a cycle of 1 min, sufficient to compensate for atmospheric fluctuations. The observing time for each source was 8-16 min at epoch 1, 8 min at epoch 2 and 12-24 min at epoch 3. The total observing time for first, second and third epochs were 14, 11 and 18 hours, respectively. The rms noise for the first, second and third epochs corresponds to 0.02-0.18, 0.06 and 0.07-0.3 Jy, respectively.

Additionally, we performed OH maser observations of IRAS 18455+0448 at 1612, 1665 and 1667 MHz. The observations were performed with the Effelsberg telescope after we observed the return of the H_2O masers of this star, to check whether the OH masers are excited again. We used the 21/18 cm primary focus receiver. At the OH maser frequency the FWHM of the telescope corresponds to ~ 470 arcsec. Mainline OH maser observations at 1665.4018 and 1667.359 were performed on 22 Feb 2010 with a bandwidth of 20 MHz and 16384 channels which provides a channel spacing of ~ 0.2 km s^{-1}. The total on source observing time was 2 hr and 26 minutes. The observations of 1612 MHz masers were made on 27 March 2010 with a bandwidth of 100 MHz and 16384 channels which corresponds to a channel spacing of ~ 1 km s^{-1}. The total on source observing time was 72 minutes. The rms noise in channels free of emission is ~ 7 mJy, for both epochs.

Region	Characteristic of the star
I	Oxygen rich non variable stars without any CSE
II	Variable oxygen rich stars with young CSE
IIIa	Variable stars with more evolved CSE
IIIb	Variable oxygen rich stars with thick CSE
IV	Variable oxygen rich stars with very thick CSE
V	Planetary nebulae and stars with cool CSE
VIa	Non variable stars with cold dust at large distances, mainly carbon-rich AGB stars
VIb	Variable stars with hot dust close to the star and cold dust at larger distances
VII	Variable stars with more evolved CSEs
VIII	Different objects

Table 5.1 – The properties of the stars located in different regions of the IRAS (60-25)/(25-12) diagram (van der Veen & Habing 1988).

79

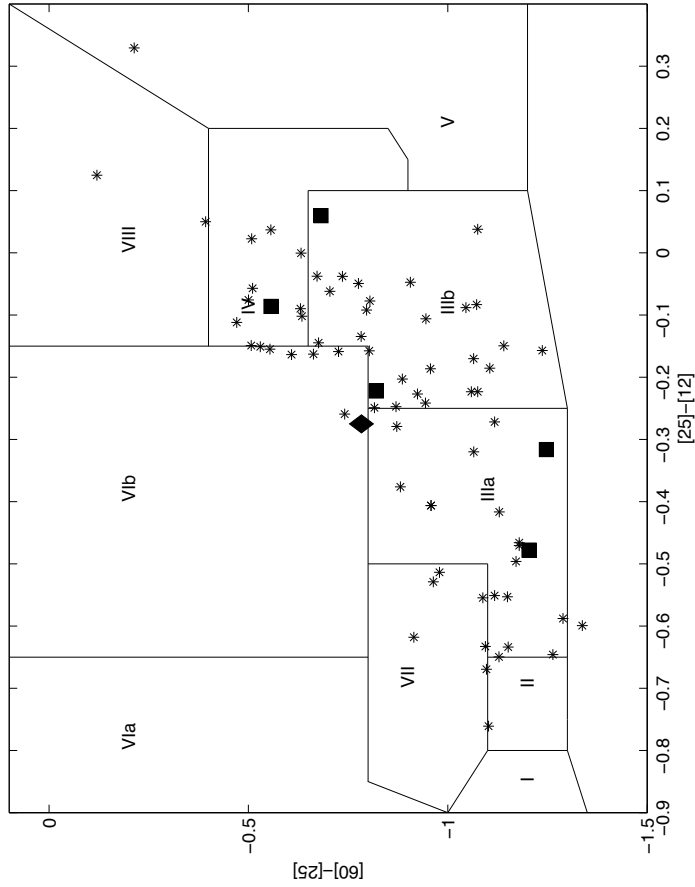**Figure 5.1** – Regions in the IRAS (60-25)/(25-12) color-color diagram which indicate various types of AGB stars (van der Veen & Habing 1988). The star symbols indicate the location of the sources in the diagram. The square symbols show the location of the water fountain candidates identified from the observations. The diamond indicates the location of the youngest proto-PNe candidate (IRAS 18455+0448).

The data reduction was performed using the Continuum and Line Analysis Single-dish Software (CLASS) package. The baseline for each spectrum was subtracted using the channels free of emission. From the observations, we obtained the raw spectra in units of temperature counts. The spectra were converted to units of antenna temperature (T_A) by applying the calibration noise temperature. We also corrected the spectra for atmospheric opacity and the gain-elevation effect. Finally, the spectra were converted to Jy units by dividing the spectra by the sensitivity of the telescope at the maser frequency.

5.3 Analysis

Table 5.4 shows the results of the observations. The spectra of the sources for which the H_2O masers were detected in at least one epoch are shown in Fig. 5.5-5.9. The analysis of the spectra observed at three epochs and comparison with the previous observations performed by Engels & Lewis (1996) reveal the appearance of new masers, the disappearance of some masers as well as significant variability in flux density and spectral shape. Among a sample of 74 sources observed, 10 masers have now disappeared. Additionally, we detected three new masers which were not observed to emit H_2O masers ~20 years ago.

5.3.1 New masers

The observations indicate three stars which exhibit new H_2O masers (IRAS 18455+0448, IRAS 19012+0819 and IRAS 19254+1631). The masers were not detected in the earlier observations by Engels & Lewis (1996).

5.3.1.1 IRAS 18455+0448

We discovered the H_2O masers of IRAS 18455+0448. This object is considered as a prototype of a dead OH/IR star after a rapid disappearance of the 1612 MHz OH masers (Lewis et al. 2001). The 1612 MHz OH masers of this star were first observed by Chengalur et al. (1993), with a double peak profile at ~27 and 40 km s^{-1} and a peak flux density of ~2 Jy for the blue-shifted masers. Follow-up monitoring of the 1612 MHz OH masers of this star indicated exponential decay in flux density. The OH masers declined in flux density by up to a factor of 20, 12 years after the first detection of the masers (Lewis et al. 2001). Additionally, the peak intensity of the blue-shifted peak at 27 km s^{-1} of the 1665 MHz masers decreased linearly by a factor of ~2 from 0.8 Jy in 1989 to ~0.4 Jy in 2000. In the case of 1667 MHz masers, apart from flare like event in 1999, the blue shifted peak at 27 km s^{-1} also showed a decrease in flux density almost by a factor of ~2 (1.6 Jy at 1998 and 0.7 Jy in 2000).

Fig. 5.5 shows the H_2O maser spectra of this star detected at three epochs with the Effelsberg telescope. The stellar velocity with respect to the local standard of rest (~34 km s^{-1}) as well as the previously observed range for the 1612 MHz OH masers (~27-40 km s^{-1}) are displayed in the figure. The spectrum shows emission blue-shifted with respect to the stellar velocity for the first two epochs with a peak flux density of ~2 Jy. In the third epoch, the spectrum shows emission at ~45 km s^{-1} with a peak flux of ~1 Jy, red-shifted with respect to the stellar velocity. Interestingly,

81
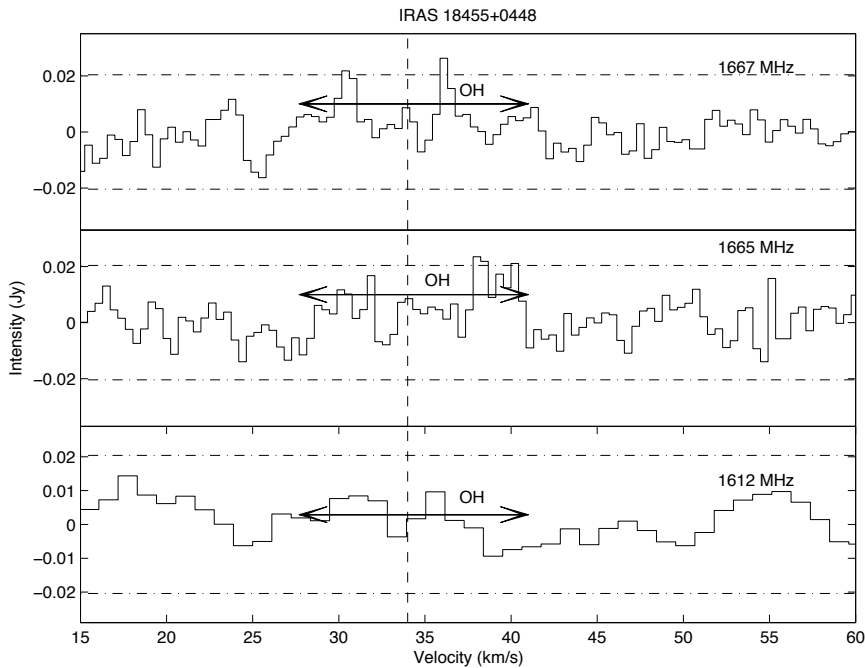
Figure 5.2 – The 1665 and 1667 MHz OH maser spectra of IRAS 18455+0448. The dashed-dotted horizontal lines are 3σ limits (~20 mJy). The vertical dashed line indicates the stellar velocity.

in all three epochs the H$_2$O maser emission range lies outside the 1612 MHz OH maser velocity range. This characteristic is not usually seen in the regular AGB stars.

We performed follow up observations of the OH masers of this star to check whether the OH masers are detectable again. Fig. 5.2 shows the OH maser spectra of IRAS 18455+0448 at 1612, 1665 and 1667 MHz. The observations indicate that the 1612 MHz OH masers have not reappeared together with the H$_2$O masers. Additionally, the observations show only a tentative detection at 1665 and 1667 MHz at 0.025 and 0.022 Jy, respectively. At both frequencies, the observed flux implies an order of magnitude decrease in flux density compared to the observations in 2000 by Lewis et al. (2001). We note that the peaks are at slightly different velocity compared to previously observed at these frequencies.

Engels & Lewis (1996) previously reported the absence of H$_2$O masers in this source. The appearance of the H$_2$O masers outside the OH maser velocity range, together with the non-detections of the 1612 MHz OH masers, raises the possibility that this object is in transition to become a PN. In particular the fact that the H$_2$O maser emission lies outside the OH maser velocity range, could indicate that a bipolar outflow is launched in this star. In order to reveal the nature of H$_2$O maser emission, follow up interferometric observations of the H$_2$O masers of this star, as well as monitoring observations at all transitions, are required.

5.3.1.2 IRAS 19112+0819

Fig. 5.7 shows the H_2O maser spectra of this star obtained at three epochs. The stellar velocity ($V_{lsr} \sim 36$ km s^{-1}) as well as the velocity range of OH maser emission are also shown in the figure. The masers were not detected in the first epoch. However, the maser profile shows the striking double peak profile in the second and third epochs. The maser emission is detected at ~ 21.6 and ~ 54 km s^{-1} with a peak flux density of ~ 2 Jy for the red-shifted complex. Comparison of the OH and H_2O maser velocity range in the second and third epochs shows a similar velocity range for both maser transitions.

5.3.1.3 IRAS 19254+1631

The H_2O maser spectra of this source observed at three epochs are shown in Fig. 5.7. In all epochs, the spectra show three emission complexes red-shifted with respect to the stellar velocity (1.9 km s^{-1}). The range of OH maser emission is also shown in the figure.

5.3.2 Variability of the H_2O masers with respect to stellar pulsation cycle

Our multi-epoch observations which spans over a time scale of ~ 500 days, enable us to study the possible relation between the variability behavior of H_2O masers with respect to the stellar pulsation cycle. We detected the H_2O masers of 23 sources in the first epoch. Among these sources, four stars lost the masers in the second and third epochs: IRAS 19081+0322, IRAS 19425+3323, IRAS 19565+3140 and IRAS 20267+2105. We define the short time scale variability for H_2O masers in the post-AGB phase. We assume that the variability time scale of the H_2O masers is 'T' days. The probability that 'm' H_2O masers have disappeared after a re-visit of Δt days among a sample of 'n' masers can be calculated according to the law of combinatorics (Engels & Jiménez-Esteban 2007):

$$P_n^m = \frac{n!}{m!\,(n-m)!} \times \left(\frac{\Delta t}{T}\right)^m \times \left(1 - \frac{\Delta t}{T}\right)^{n-m}$$
(5.1)

The 'n' and m values in Eq. 5.1 correspond to 23 and 4, respectively. Fig. 5.3, shows the probability of the disappearance of 3 maser features in the second epoch ($\Delta t \sim 485$ days). The figure shows a variability time scale of ~ 3000 days (~ 8 years) for the H_2O masers in the post-AGB phase. We note that the estimated variability timescale is similar to the period of high mass loss OH/IR stars (~ 2000 days more more). This indicates similar variability properties for OH/IR stars exist, which implies the variability of the masers are related to the pulsation period as was previously found for Mira variables (Shintani et al. 2008).

5.3.3 Disappearing H_2O masers

The observations also enable us to study the longer time scale variability by comparing the observations to the original work by Engels & Lewis (1996). The source sample includes 33 H_2O masers which were detected by Engels & Lewis (1996). We found that 10 sources no longer exhibit maser
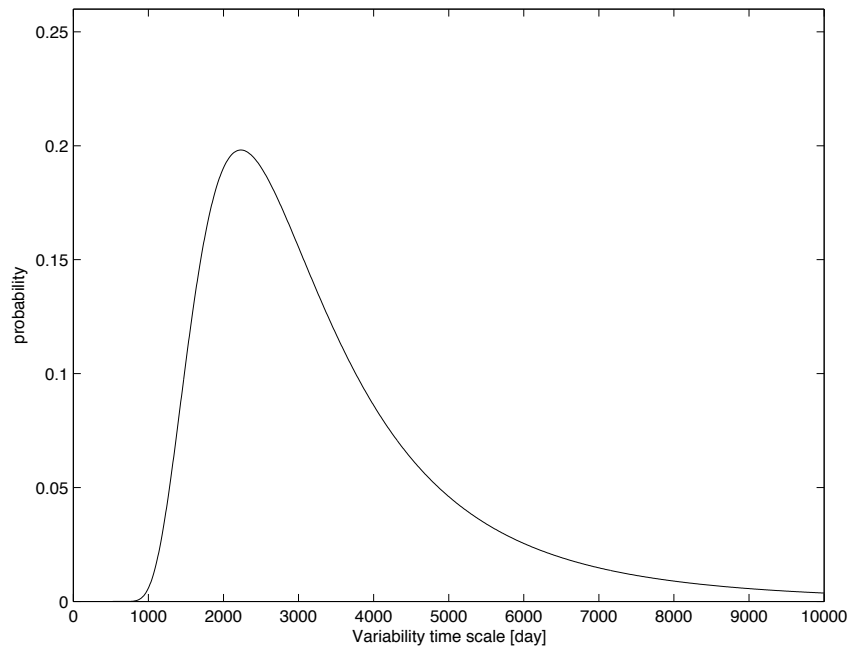
Figure 5.3 – Probability (P_n^m), that m=4 masers have disappeared among a sample of n=23 masers detected in the first epoch of our observations. The horizontal axis indicates the variability time scale (T) of the H$_2$O maser features in days.

emission in our multi-epoch observations. Table 5.2 lists the H_2O masers which were observed to have H_2O masers ~20 years ago, but no longer show maser emission. The 3σ upper limit for flux density is also given for every source at each epoch. We assume that AGB stars only support maser emission at specific times since the masers require optimal coherence path. If the stars which no longer exhibit maser emission in our multi-epoch observations do not come back, we can estimate the lifetime of the masers statistically according to Eq. 5.1. We assume that the lifetime of the H_2O masers is 'T' years. The 'm' and 'n' values from our observations correspond to 10 and 33, respectively. Fig. 5.4 displays the probability of finding 10 masers disappeared after a re-visit of 20 years. The figure shows a lifetime of ~60 years for H_2O masers in the post-AGB phase.

However, the overall lifetime of the H_2O masers is the lower limit. As mentioned in previous section, H_2O masers exhibit short time scale variability which is likely related to the stellar pulsation. This could imply that the disappearance of the masers could be the related to the stellar pulsation and that the masers may come back again at a later time. This is already evident as we have seen three masers return from previous observations ~20 years ago. As the sources selected from the detections and non-detections sample are of similar sizes, this could imply that three masers could return at a later time among the 10 masers disappeared. In that case the value of 'm' in Eq. 5.1 changes. For illustration, we show in Fig. 5.4 curves with m=10, 7 and 3 which indicate the result of over estimate of the disappeared masers. Therefore, the overall lifetime of the H_2O masers in the post-AGB phase could be much longer.

Additionally, the estimated lifetime of the masers may be influenced by the sensitivity limitations of the telescope. Therefore, it is possible that the star still exhibits maser emission, but the maser intensity is below the sensitivity of the telescope.

5.3.4 Individual Sources with double peak profiles

Water fountain sources are defined by having high velocity H_2O maser outflows (e.g. Likkel et al. 1992). The H_2O maser velocity is typically larger than the OH maser velocity range traced by 1612 MHz OH maser observations (10-20 km s^{-1}, te Lintel Hekkert et al. 1989). From the Effelsberg observations, we identified several water fountain candidates which exhibit the striking double peak profiles in at least one observation epoch. We note that the velocity extent of the sources identified is not as large as those observed previously for other water fountain sources (e.g. ~200 km s^{-1}, Imai et al. 2008).

5.3.4.1 IRAS 19422+3506

We detected a double peak profile together with emission close to the stellar velocity for IRAS 19422+3506 (Fig. 5.7). The stellar velocity with respect to the local standard of rest (-48.4 km s^{-1}) as well as the range of the OH maser emission are also shown in the figure. Previous H_2O maser observations of this star indicated a single peak profile at -60.9 km s^{-1} with a peak flux density of 52 Jy (Engels & Lewis 1996). Shintani et al. (2008) also observed the H_2O maser of this star, but no detection was reported.

The H_2O maser spectrum of this source at the first epoch (Fig. 5.7) shows double peak structure at -40 and -70 km s^{-1}. Also, there are central peaks close to the stellar velocity (-48 km s^{-1}). The double peak structure could indicate that the maser emission originates in a jet that lies close to

source	V$_p$ km s^{-1}	Flux Jy	3σ (epoch 1) Jy	3σ (epoch 2) Jy	3σ (epoch 3) Jy
IRAS 18341+0005	57.7	0.2	0.3	0.4	0.4
	59.6	0.6			
IRAS 18568+0550	-50	0.2	0.3	0.5	0.4
IRAS 18578+0831	36.8	0.3	0.35	0.3	0.4
IRAS 19017+0412	98.6	2.4	0.14	0.3	0.7
IRAS 19043+1009	34.8	2.6	0.5	0.3	0.4
IRAS 19052+0922	37.8	0.4	0.35	0.3	0.4
	54.8	0.7			
IRAS 19054+0419	-51.1	0.45	0.35	0.3	0.4
	-48	0.4			
	-30.3	0.15			
IRAS 19316+0919	78.5	6.1	0.13	0.3	0.13
IRAS 19462+2232	4.5	7	0.55	0.2	0.9

Table 5.2 – H$_2$O masers which were detected in previous observations by Engels & Lewis (1996), but have now disappeared in our multi-epoch observations. The first column shows the velocity at which the masers were detected and the second column lists the observed flux densities of the masers in the original observations (Engels & Lewis 1996). The last three columns indicate our upper limits.
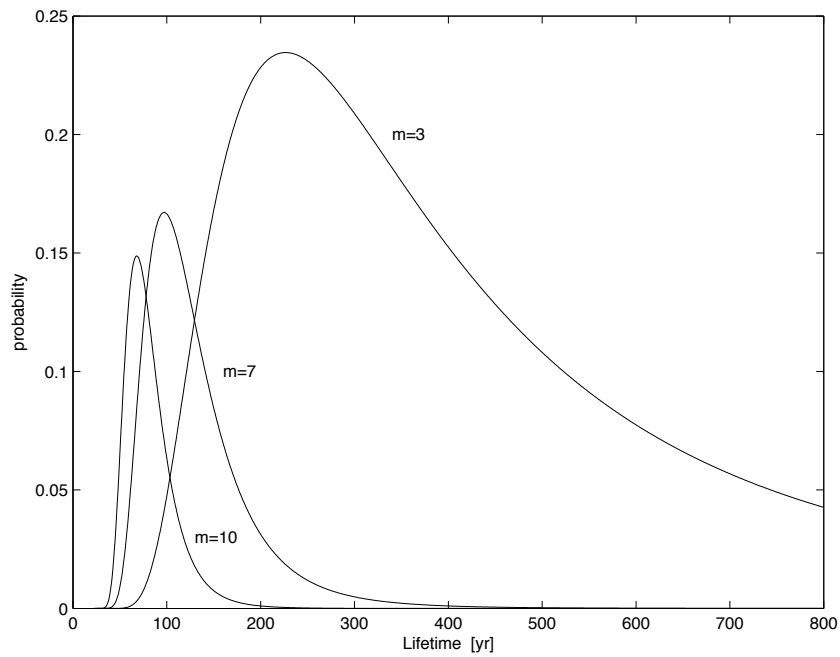
Figure 5.4 – Probability (P_n^m), that m=10, 7 and 3 masers have disappeared among a sample of n=33 previously detected H_2O masers. The horizontal axis indicates the lifetime T of the H_2O masers.

the plane of the sky, but it could also imply the radial amplification of the masers (Engels & Lewis 1996, Engels et al. 1997). The presence of the inner peaks could indicate that the inner peak masers occur in the equatorial plane of the circumstellar shell (Walsh et al. 2009).

Comparison of the H_2O maser spectra of this source obtained at three epochs shows significant variability in spectral shape and flux density. At the first epoch, the red-shifted peak was detected at ~13 Jy. However, for the second and third epochs the flux density has decreased by about an order of magnitude. In the second epoch, the emission close to the stellar velocity has the highest flux density (~1 Jy). At the third epoch which was performed about three weeks apart from the second epoch observations, the spectral shape is similar to that observed in the first epoch and the red-shifted emission has a flux density of ~1.3 Jy. Similar phenomena are known from monitoring observations of the H_2O masers of the OH/IR star OH 39.7+1.5, which showed evidence of mode switching between radial and tangential amplification with the stellar pulsation cycle (Engels et al. 1997). This star has a period of ~1430 days (Van Langevelde et al. 1990). During the stellar maximum the maser profile was similar to the double peak OH maser profile which indicates the radial amplification of the masers. However, close to the minimum phase of the stellar pulsation which occurred ~550 days after the stellar maximum, the radially beamed masers disappeared and the profile only showed emission close to the stellar velocity which implies the masers are tangentially amplified. Engels et al. (1997) argue that both the tangential and radially beamed masers are located in the same region and that due to the competitive gain, tangential amplification occurs only when the physical conditions are not sufficient to excite the radially beamed masers.

Therefore, the mode switching between the radial and tangential amplification of IRAS 19422+3506 could be related to the stellar pulsation. Monitoring H_2O maser observations of this star over a longer timescale is required to clarify the variability of the maser profile with respect to the stellar pulsation cycle.

5.3.4.2   IRAS 19067+0811

The H_2O masers of this star were not detected at the first epoch (Fig. 5.6). However, in the second and third epochs we observed a double peak profile at 45 and 78 km s^{-1} with a peak flux density of 3.5 Jy for the red-shifted complex of the H_2O masers of this star. The stellar velocity (59.2 km s^{-1}) as well as the range of OH maser emission are also shown in the figure. Previous observations of this star by Engels & Lewis (1996) only indicated a single peak profile for the red-shifted emission with a peak flux density of 3 Jy.

5.3.4.3   IRAS 19069+0916

We observed a double peak profile for the H_2O masers of this star at the first epoch at ~13 and 46 km s^{-1} with a maximum flux density of ~7 Jy for the blue-shifted complex (Fig. 5.6). For the second and third epochs the spectra only show a single peak at ~18 km s^{-1} with a flux density of ~0.8 Jy. The stellar velocity (32.7 km s^{-1}) as well as the range of OH maser emission are also shown in the figure. Previous observations of this star also showed double peak profiles at ~11 and 44 km s^{-1}, with a peak flux density of 2.4 and 0.4 Jy, respectively.

5.3.4.4 IRAS 19186+0315

The H_2O maser spectrum of this star shows a double peak profile at -35 and -15 km s^{-1} in all three epochs (Fig. 5.7). The blue shifted component has the higher flux density in each epoch. We note that the spectral shape appears consistent during our multi-epoch observations. However, the previous observations of the H_2O masers of this star only showed emission at -33.7 km s^{-1} with a flux density of 6 Jy (Engels & Lewis 1996).

5.4 Discussion

5.4.1 Water Fountain Candidates

As mentioned earlier, water fountain sources often show high velocity H_2O maser outflows (e.g.~200 km s^{-1} or more, Likkel et al. 1992, Imai et al. 2008). From our multi-epoch observations, we identified six water-fountain candidates : IRAS 18455+0448, IRAS 19112+08129, IRAS 19422+3506, IRAS 19067+0811, IRAS 19069+0916, and IRAS 19186+0315. The locations of these sources in the IRAS (60-25)/(25-12) color-color diagram are shown in Fig. 5.1. The H_2O maser spectrum of all these stars exhibits a double peak profile at least in one epoch. The double peak profile raises the possibility that a bipolar outflow is launched in these stars.

However, the water-fountain candidates that we identified, do not exhibit a large velocity extent in their H_2O maser profile. One possibility is that the projection of the velocity vector along the line of sight for a jet in the plane of the sky results in a V_{lsr} maser velocity range that is not as wide. Additionally, the lower velocity extent could indicate that the masers are located in biconical outflows, which do not necessarily exhibit a large velocity extent in the spectrum (Maeda et al. 2008). Alternatively, this could imply that the jet is recently launched and is accelerating outwards. Previously, water fountains with lower velocity outflows for H_2O masers have been reported. For example, the H_2O maser jet of the water fountain source, OH 12.8-0.8, only shows ~55 km s^{-1} velocity extent (Boboltz & Marvel 2005). Additionally, the interferometric observations of the OH maser region of this star showed that the H_2O maser jet lies inside the OH maser shell which implies that the jet could be recently launched in this star (Amiri et al. 2011). In order to clarify this, interferometric observations of the H_2O masers of these stars are required to obtain the spatial distribution of the H_2O masers.

Alternatively, the double peak profile observed for the H_2O masers may indicate radial amplification of the H_2O masers. Engels & Lewis (1996) divide the H_2O maser spectra of evolved stars into two groups. Group A sources show emission close to the radial velocity of the star, as commonly observed for Mira variables. The H_2O masers in this case are located close to the central AGB star. At such distances there is large velocity gradient along the radial direction and as a result the masers are tangentially amplified. However, sources in group B display double peak profiles with velocities close to those of OH masers. High mass loss rate OH/IR stars likely belong to this group. The H_2O maser shell is located at larger distances compared to the location of H_2O masers in lower mass loss rate Mira variables. At such large distances, there is lower velocity gradient which allows the radial amplification of masers, that manifest itself in double peak profile. This type of profile is usually observed for high mass loss OH/IR stars. Moreover, in one of our objects, IRAS 19422+3506, we found confirmation of the model proposed by Engels et al. (1997) for the changes in the H_2O maser

emission in the OH/IR star OH 39.7+1.5. It seems possible that in some OH/IR stars the maser amplification switches from radial to tangential within the stellar pulsation.

5.4.2   IRAS 18455+0448, Youngest proto-PNe candidate

We discovered the H_2O masers of the supposedly dead OH/IR star IRAS 18455+0448. The exponential decline of the 1612 MHz OH masers of this star were previously reported by Lewis et al. (2001). The lack of the OH masers could imply that the mass-loss has stopped in this star. Interestingly, our followup observations of the OH masers (1612, 1665 and 1667 MHz) indicate that this star seems to emit weak mainline masers, but not the 1612 MHz OH masers. This could be due to the fact that the 1612 MHz masers require larger column density and as a result of the cessation of the mass-loss, they disappear faster than the mainline masers (Lewis 1989).

The detection of the H_2O masers in this source could have two explanations. First possibility is that the mass loss has resumed in this star and that the H_2O masers are emitted close to the central star. The other possibility would be that the H_2O masers are excited in the wind, outside the OH masers at the tips of a jet. In particular, we found that the H_2O maser velocity range is larger than the previously observed 1612 MHz OH maser emission (Fig. 5.5), which is an essential characteristic of water-fountain sources. To clarify between these two possibilities, we need high resolution interferometric observations to obtain the spatial extent of the H_2O masers and accurate positions for follow up VLBI observations. In particular, if the second scenario (jet) is confirmed, this source will be the youngest proto-PN identified so far.

5.4.3   Variability

We observed a sample of 74 post-AGB candidates to monitor the variability of the H_2O masers in the pre-PNe stage. The sources in our sample are mainly OH/IR stars which are expected to have thicker and denser circumstellar shells compared to Mira variables. OH/IR stars are expected to have longer periods, ~2000 days or more. The multi-epoch observations covered a time scale of ~500 days. We found that the H_2O masers exhibit significant variability in flux density and spectral characteristics. We observed the rise of new maser features that differ by as much as 35 km s^{-1} in velocity from features detected in the earlier observations (e.g. IRAS 19422+3506; Fig. 5.7). H_2O masers in regular AGB stars are located in a region where the medium is highly turbulent and undergoes radial acceleration. Rudnitskii & Chuprikov (1990) attribute the variability of the H_2O masers to the shock waves propagating in the H_2O maser region. These shock waves are periodically generated in the H_2O maser region and travel outward in the CSE. However, it is not clear how shock waves with a few km s^{-1} speed can have an strong effects in the H_2O maser zone.

H_2O maser monitoring in Mira variables with a time spacing of 1-2 months revealed good correlation between the stellar light curve and the H_2O maser emission (Shintani et al. 2008). Their results show that the H_2O maser emission changes over the pulsation cycle of the star. Since the sources studied in our work belong to a different class of AGB stars, we do not have optical light curves available to study the correlation between the stellar pulsation and the H_2O maser emission. However, our observations likely show a correlation between the stellar pulsation cycle and the short time scale variability (~3000 days, Fig. 5.3), which is the same order of magnitude as the pulsation of high mass loss OH/IR stars.

For 10 sources, we observed disappearance of the masers, compared to the earlier observations performed ~20 years ago by Engels & Lewis (1996). Assuming that the masers do not come back again, we estimate a lifetime of ~60 years for H_2O masers in the post-AGB phase from statistical arguments. Since our multi-epoch observations only cover a timescale of ~500 days, which is much shorter than the period of OH/IR stars (2000 days or more), we can not confirm that the masers will not rise up again. Therefore, follow up monitoring H_2O maser observations spanning the whole period of OH/IR stars are required to clarify this. Additionally, follow up 1612 MHz OH maser observations of the sources are required to understand whether the stars which already show a decline in the H_2O maser emission, still exhibit 1612 MHz OH maser emission. The lack of OH maser emission could imply limited lifetime of the masers in the post-AGB phase.

It is not clear however, whether stars only support maser emission once during the AGB and post-AGB phases or H_2O masers turn on and off several times. OH/IR stars are found to be dead when they no longer exhibit 1612 MHz OH maser emission (Lewis 2003, Lewis et al. 2001). A dead OH/IR star can then undergo one of the two evolutionary scenarios. In the first scenario the mass loss stops and the CSE expands sufficiently that it no longer exhibits maser emission. The star then first become a proto-PNe and finally a PN. Alternatively, the mass loss can decrease temporarily after a Helium shell flash, despite the fact the star is still in the AGB phase and maintains the CSE (Lewis et al. 2001). In this scenario, the masers will be back after the mass loss resumes. Monitoring observations of the 1612 MHz OH masers of a sample of OH/IR stars that showed decline in flux density indicated that most AGB stars likely go through an OH/IR phase several times during the AGB phase (Lewis 2003).

5.5 Conclusions

We performed 22 GHz multi-epoch observations of a sample of post-AGB candidates. We identified six water fountain candidates which exhibit the striking double peak profile in at least one epoch. The double peak profile is a strong indication that a bipolar H_2O maser outflow is launched in these stars. Follow up interferometric observations of the identified water fountain candidates are required to understand the spatial distribution of the H_2O masers. In particular, if a bipolar H_2O maser jet is confirmed for IRAS 18455+0448, this source could be the youngest proto-PNe candidate identified so far.

Furthermore, we found that the H_2O masers of the post-AGB candidates studied in this work, exhibit large variability in flux density and profile shape. We estimate an overall lifetime of ~60 years for the H_2O masers in the post-AGB phase. Additionally, the observations likely indicate that the variability on shorter timescale (~3000 days) is related to stellar pulsation, as was previously found for Mira variables.

Table 5.3 – Source sample

	IRAS Name	RA (J2000)	Dec (J2000)	[25-12]	[60-25]	V_{lsr} km s^{-1}
1	IRAS 18095+2704	18 11 30.67	+27 05 15.5	0.0381	-1.0752	-4.6
2	IRAS 18341+0005	18 36 40.67	+00 08 01.2	-0.5528	-1.1496	85.4
3	IRAS 18349+1023	18 37 19.26	+10 25 42.2	-0.7609	-1.1022	-32
4	IRAS 18353+0020	18 37 55.79	+00 23 31.6	-0.0831	-1.0722	-43.5
5	IRAS 18395+0130	18 42 03.10	+01 33 15.0	-0.1863	-0.9565	48.6
6	IRAS18398+1035	18 42 09.98	+10 38 54.9	-0.6327	-1.0944	78.6
7	IRAS 18455+0448	18 48 02.30	+04 51 30.5	-0.2748	-0.7835	34.1
8	IRAS 18475+0353	18 50 00.1	+03 56 32	-0.0568	-0.5105	25.8
9	IRAS 18490+0302	18 51 35.64	+03 05 55.9	-0.259	-0.7416	130.9
10	IRAS 18534+0215	18 55 59.0	+02 19 06	-0.1509	-0.53	39.6
11	IRAS 18549+0208	18 57 27.5	+02 12 16	-0.0757	-0.5003	77.9
12	IRAS 18549+0905	18 57 20.82	+09 09 40.9	-0.496	-1.1713	19.4
13	IRAS 18568+0550	18 59 20.74	+05 54 41.1	-0.1446	-0.6761	-52
14	IRAS 18571+0611	18 59 35.98	+06 15 36.6	-0.149	-0.5071	35.4
15	IRAS 18578+0831	19 00 17.5	+08 35 29	-0.2028	-0.886	48.8
16	IRAS 18596+0315	19 02 06.28	+03 20 16.3	0.3296	-0.2136	88.4
17	IRAS 19006+0624	19 03 03.3	+06 28 52	-0.1635	-0.6082	-31
18	IRAS 19012+1128	19 03 36.71	+11 33 03.4	-0.5509	-1.1173	53.7
19	IRAS 19017+0412	19 04 14.42	+04 16 59.5	-0.2718	-1.1176	85.8
20	IRAS 19017+0608	19 04 09.71	+06 13 16.0	-0.1344	-0.7826	148.6
21	IRAS 19035+0451	19 05 58.91	+04 55 45.6	-0.5134	-0.9794	88.9
22	IRAS 19043+1009	19 06 43.0	+10 14 32	-0.4164	-1.1292	49.5
23	IRAS 19052+0922	19 07 38.91	+09 27 16.6	-0.5288	-0.9636	44
24	IRAS 19054+0419	19 07 55.9	+04 23 51	-0.249	-0.8162	-37
25	IRAS 19065+0832	19 08 58.8	+08 37 45	-0.0003	-0.6322	53.1
26	IRAS 19067+0811	19 09 07.471	+08 16 22.52	0.0599	-0.682	59.2
27	IRAS19069+0916	19 09 19.4	+09 21 13	-0.086	-0.5568	31.8

Table 5.3 – Continued.

	IRAS Name	RA (J2000)	Dec (J2000)	[25-12]	[60-25]	V_{lsr} km s^{-1}
28	IRAS 19075+1147	19 09 54.08	+11 52 47.7	-0.1493	-1.1405	4.8
29	IRAS 19076+1247	19 09 56.83	+12 52 56.5	-0.2791	-0.8719	47.4
30	IRAS 19081+0322	19 10 36.70	+03 27 02.3	-0.1017	-0.6345	41.5
31	IRAS19083+0851	19 10 47.33	+08 56 22.9	-0.466	-1.1792	45.5
32	IRAS 19085+0755	19 10 59.7	+08 00 23	-0.1117	-0.4708	76.1
33	IRAS 19112+0819	19 13 37.32	+08 24 52.4	-0.2219	-0.8206	38.6
34	IRAS 19128+0910	19 15 16.2	+09 15 46	-0.106	-0.9452	51.4
35	IRAS 19128+1310	19 15 07.97	+13 16 00.1	-0.2269	-0.9238	62.1
36	IRAS 19172+1956	19 19 28.7	+20 01 39	-0.2473	-0.8703	46.4
37	IRAS 19178+1206	19 20 14.01	+12 12 20.3	-0.0375	-0.6723	47.2
38	IRAS 19183+1148	19 20 42.59	+11 54 04.5	-0.0617	-0.7044	34.4
39	IRAS 19186+0315	19 21 11.70	+03 20 57.9	-0.3161	-1.2473	-22
40	IRAS 19188+1057	19 21 11.8	+11 02 49	-0.0898	-0.6306	-22.5
41	IRAS 19200+1035	19 22 26.67	+10 41 21.3	-0.1627	-0.663	53.4
42	IRAS 19200+1536	19 22 17.77	+15 41 49.0	-0.1587	-0.726	59.6
43	IRAS 19201+1040	19 22 29.2	+10 46 19	-0.2415	-0.9441	53.5
44	IRAS 19226+1401	19 24 54.1	+14 07 31	-0.1547	-0.554	4.7
45	IRAS 19248+1441	19 27 07.34	+14 47 21.7	-0.6179	-0.9149	36.8
46	IRAS 19254+1631	19 27 42.04	+16 37 24.0	0.0227	-0.5083	1.9
47	IRAS 19283+1944	19 30 29.48	+19 50 41.0	-1015	-0.72	27.4
48	IRAS 19295+2228	19 31 38.97	+22 35 17.2	-0.157	-1.2372	-74
49	IRAS 19316+0919	19 34 02.81	+09 26 06.2	-0.6692	-1.0971	76.4
50	IRAS 19343+2926	19 36 18.91	+29 32 50.0	0.1249	-0.1201	-0.9
51	IRAS19344+2457	19 36 32.03	+25 04 13.1	-0.1854	-1.1053	5.5
52	IRAS 19352+2030	19 37 24.00	+20 36 57.8	-0.0491	-0.776	-1.0
53	IRAS 19360+3442	19 37 57.77	+34 49 36.2	-0.2231	-1.075	-67.7
54	IRAS 19374+1626	19 39 40.4	+16 33 44	-0.0918	-0.7963	-29.5
55	IRAS 19440+2251	19 46 08.8	+22 59 24	-0.1574	-0.803	-7.5

93

	IRAS Name	RA (J2000)	Dec (J2000)	[25-12]	[60-25]	V_{lsr} km s^{-1}
56	IRAS 19422+3506	19 44 07.00	+35 14 08.2	-0.4778	-1.2037	-48.4
57	IRAS 19425+3323	19 44 29.96	+33 30 38.4	-0.5992	-1.3373	9.6
58	IRAS 19451+1628	19 47 26.66	+16 35 35.9	-0.3762	-0.8812	25.4
59	IRAS 19462+2232	19 48 26.24	+22 39 56.8	-0.4705	-1.1791	13
60	IRAS 19520+2729	19 54 08.64	+27 37 01.8	-0.2232	-1.059	-1.3
61	IRAS 19565+3140	19 58 30.29	+31 48 16.1	-0.0472	-0.9063	20.4
62	IRAS 19575+1143	19 59 56.39	+11 51 45.1	-0.6458	-1.2636	-10.3
63	IRAS 19576+2814	19 59 39.14	+28 23 07.3	-0.0774	-0.8046	-58.7
64	IRAS 19579+3223	19 59 51.32	+32 32 09.8	-0.6494	-1.1285	5.5
65	IRAS 20023+2855	20 04 20.74	+29 04 06.5	0.0369	-0.5565	-64.8
66	IRAS 20043+2653	20 06 22.74	+27 02 10.6	-0.0378	-0.7358	-4.6
67	IRAS 20137+2838	20 15 47.65	+28 47 54.9	-0.088	-1.0455	-57.8
68	IRAS 20160+2734	20 18 05.886	+27 44 03.69	-1.002	-0.4328	6.1
69	IRAS 20267+2105	20 28 57.10	+21 15 37.0	-0.4063	-0.9582	-72.8
70	IRAS 20272+3535	20 29 08.4	+35 45 44	0.0502	-0.3928	-4.1
71	IRAS 20351+3450	20 37 07.95	+35 01 10.7	-0.5878	-1.2889	-5.4
72	IRAS 20403+3700	20 42 18.49	+37 11 41.0	-0.5545	-1.0878	-50.9
73	IRAS 20460+3253	20 48 03.36	+33 05 02.1	-0.6336	-1.1516	32
74	IRAS 20531+2909	20 55 17.8	+29 20 49	-0.17	-1.0648	-137

Table 5.3 – Continued.

Table 5.4 – Results.

	IRAS Name	Engels & Lewis (1996)	Nov 2009	March 2011	April 2011
1	IRAS 18095+2704	N	N	N	N
2	IRAS 18341+0005	Y	N	N	N
3	IRAS 18349+1023	Y	Y	Y	Y
4	IRAS 18353+0020	N	N	N	N
5	IRAS 18395+0130	Y	N	N	N
6	IRAS18398+1035	Y	Y	Y	Y
7	IRAS 18455+0448	N	Y	Y	Y
8	IRAS 18475+0353	N	N	N	N
9	IRAS 18490+0302	N	N	N	N
10	IRAS 18534+0215	N	N	N	N
11	IRAS 18549+0208	N	N	N	N
12	IRAS 18549+0905	Y	Y	Y	Y
13	IRAS 18568+0550	Y	N	N	N
14	IRAS 18571+0611	N	N	N	N
15	IRAS 18578+0831	Y	N	N	N
16	IRAS 18596+0315	Y	Y	Y	N
17	IRAS 19006+0624	N	N	N	N
18	IRAS 19012+1128	Y	Y	Y	Y
19	IRAS 19017+0412	Y	N	N	N
20	IRAS 19017+0608	N	N	N	N
21	IRAS 19035+0451	Y	Y	Y	Y
22	IRAS 19043+1009	Y	N	N	N
23	IRAS 19052+0922	Y	N	N	N
24	IRAS 19054+0419	Y	N	N	N
25	IRAS 19065+0832	N	N	N	N
26	IRAS 19067+0811	Y	Y	Y	Y
27	IRAS19069+0916	Y	Y	Y	Y
28	IRAS 19075+1147	N	N	N	N

	IRAS Name	Engels & Lewis (1996)	Nov 2009	March 2011	April 2011
29	IRAS 19076+1247	N	N	N	N
30	IRAS 19081+0322	Y	Y	N	N
31	IRAS19083+0851	Y	Y	Y	Y
32	IRAS 19085+0755	Y	Y	Y	Y
33	IRAS 19112+0819	N	N	Y	Y
34	IRAS 19128+0910	N	N	N	N
35	IRAS 19128+1310	N	N	N	N
36	IRAS 19172+1956	N	N	N	N
37	IRAS 19178+1206	N	N	N	N
38	IRAS 19183+1148	N	N	N	N
39	IRAS 19186+0315	Y	Y	Y	Y
40	IRAS 19188+1057	N	N	N	N
41	IRAS 19200+1035	N	N	N	N
42	IRAS 19200+1536	N	N	N	N
43	IRAS 19201+1040	N	N	N	N
44	IRAS 19226+1401	N	N	N	N
45	IRAS 19248+1441	Y	Y	Y	Y
46	IRAS 19254+1631	N	Y	Y	Y
47	IRAS 19283+1944	N	N	N	N
48	IRAS 19295+2228	N	N	N	N
49	IRAS 19316+0919	Y	N	N	N
50	IRAS 19343+2926	N	N	N	N
51	IRAS19344+2457	N	N	N	N
52	IRAS 19352+2030	N	N	N	N
53	IRAS 19360+3442	N	N	N	N
54	IRAS 19374+1626	N	N	N	N
55	IRAS 19440+2251	N	N	N	N
56	IRAS 19422+3506	Y	Y	Y	Y
57	IRAS 19425+3323	Y	Y	N	N

Table 5.4 – Continued.

96

Table 5.4 – Continued.

|	IRAS Name	Engels & Lewis (1996)	Nov 2009	March 2011	April 2011
58	IRAS 19451+1628	Y	N	N	N
59	IRAS 19462+2232	Y	N	N	N
60	IRAS 19520+2729	N	N	N	N
61	IRAS 19565+3140	Y	Y	Y	Y
62	IRAS 19575+1143	Y	Y	Y	Y
63	IRAS 19576+2814	N	N	N	N
64	IRAS 19579+3223	Y	Y	Y	Y
65	IRAS 20023+2855	N	N	N	N
66	IRAS 20043+2653	N	N	N	N
67	IRAS 20137+2838	Y	Y	Y	Y
68	IRAS 20160+2734	N	N	N	N
69	IRAS 20267+2105	Y	Y	N	N
70	IRAS 20272+3535	N	N	N	N
71	IRAS 20351+3450	Y	Y	Y	Y
72	IRAS 20403+3700	Y	Y	Y	Y
73	IRAS 20460+3253	Y	Y	Y	Y
74	IRAS 20531+2909	N	N	N	N
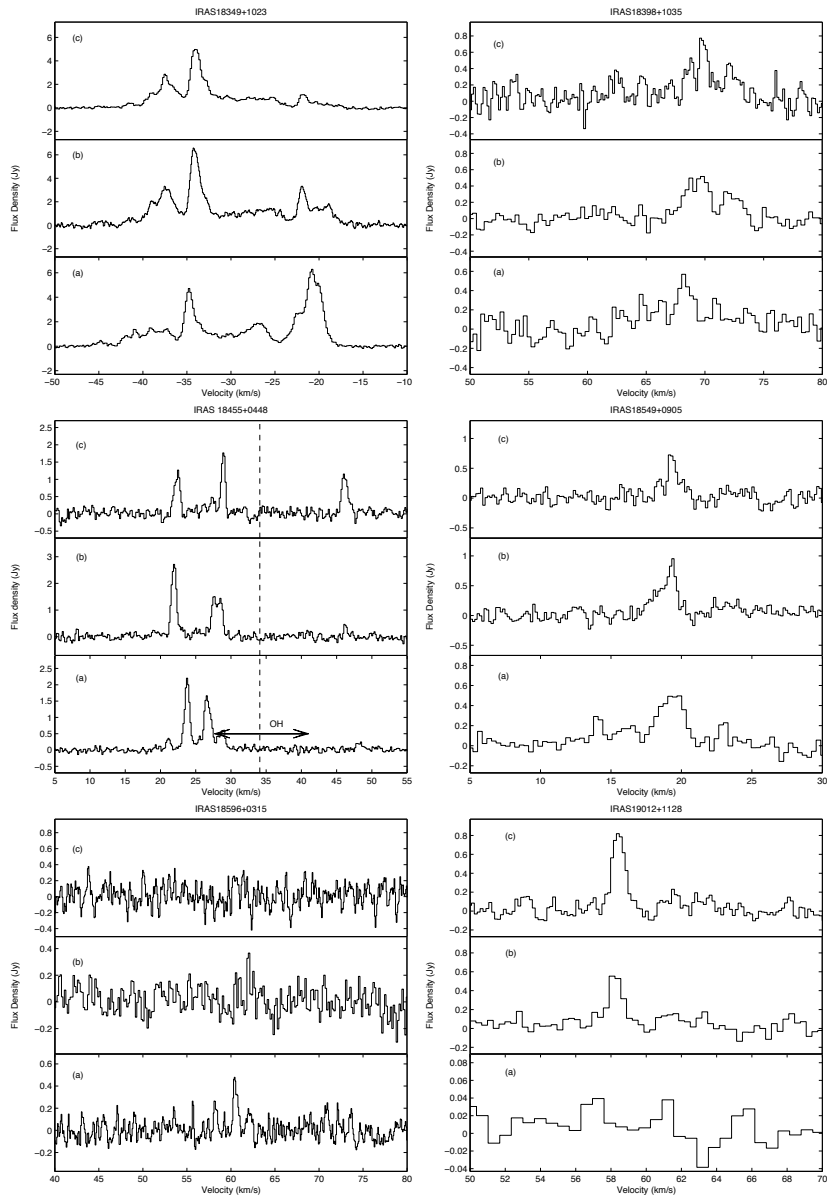
Figure 5.5 – H$_2$O maser spectra. Panels a, b and c show the spectrum observed at first (November 2009), second (March 2011) at third epochs (April 2011), respectively. The OH maser velocity range for water fountain candidates is shown in the plots. The dashed vertical lines indicate the stellar velocity.
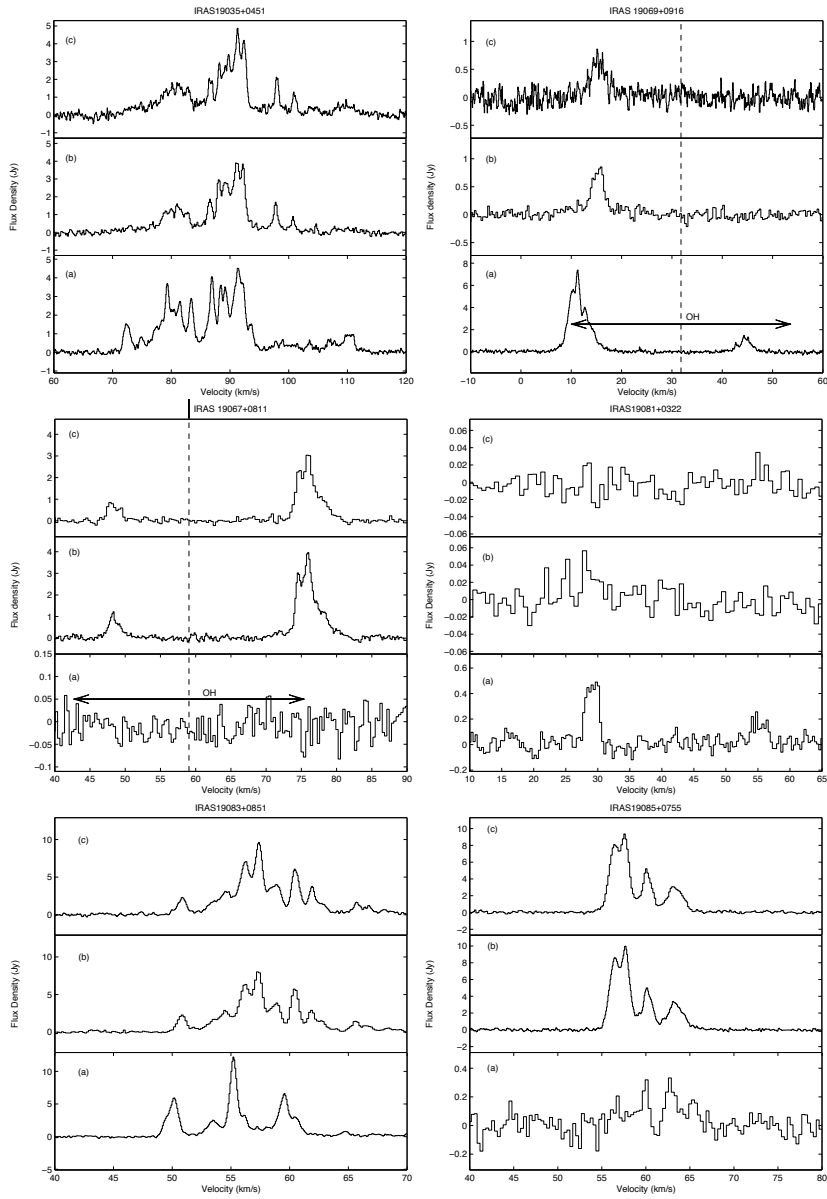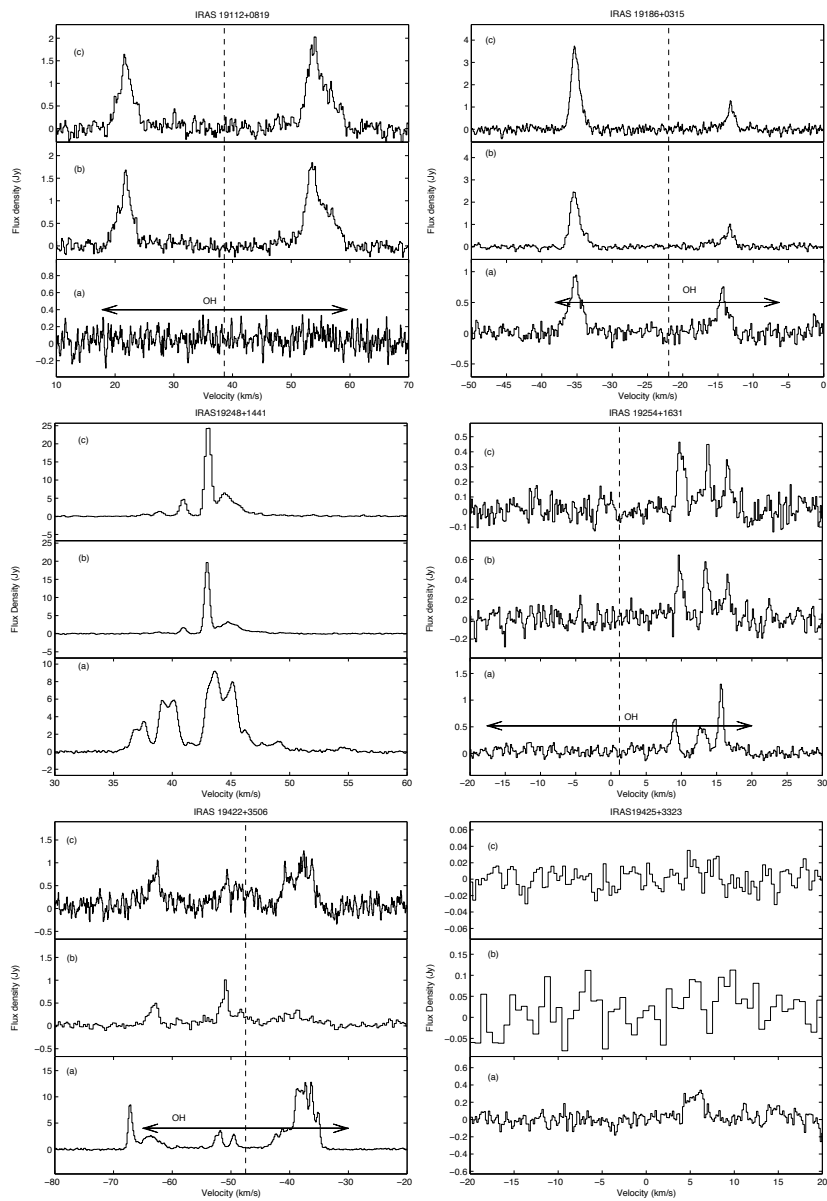
Figure 5.6 – Continued.
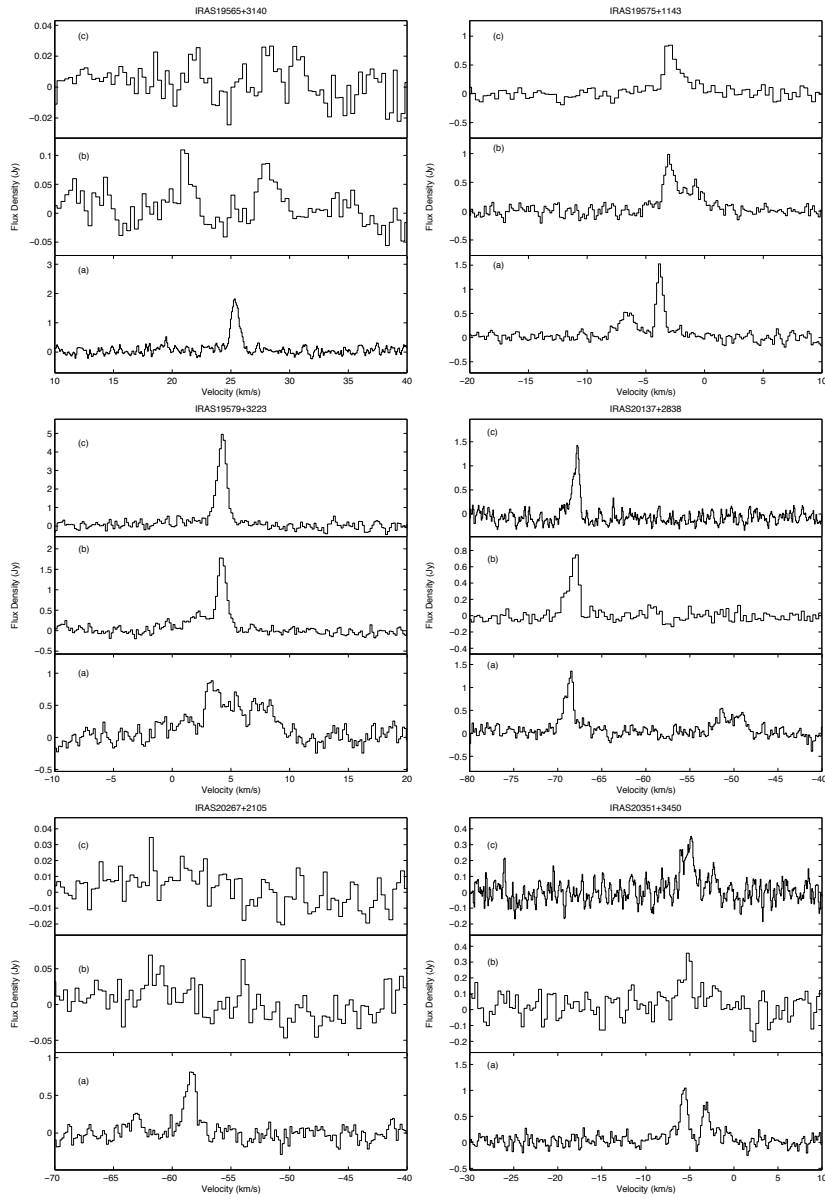
Figure 5.7 – Continued.

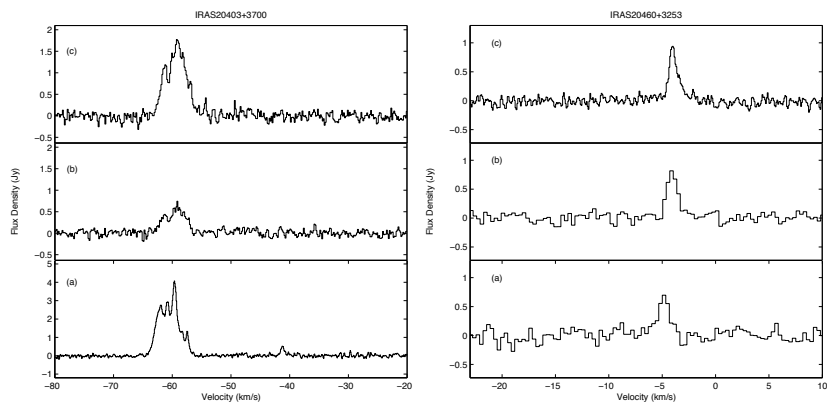**Figure 5.8** – Continued.

Figure 5.9 – Continued.

VLBA SiO maser observations of the OH/IR star OH 44.8-2.3: magnetic field and morphology

N. Amiri, W. H. T. Vlemmings, A. J. Kemball, H. J. van Langevelde

103

Abstract

SiO maser emission occurs in the extended atmosphere of evolved stars and can be studied at high angular resolution. As compact, high brightness components they can be used as important tracers of the dynamics at distances close to the central star. The masers also serve as probes of the evolutionary path from spherically symmetric AGB stars to aspherical PNe. Very long baseline interferometry (VLBI) observations of Mira variables indicate that SiO masers are significantly linearly polarized with linear polarization fraction up to 100%. However, no information is available at high angular resolution for SiO masers in higher mass loss OH/IR stars. Theory indicates a different SiO pumping mechanism in higher mass loss evolved stars. We extend the VLBI SiO maser studies to OH/IR stars. The observations enable us to understand the SiO pumping mechanisms in higher mass loss evolved objects and compare those with Mira variables. Additionally, polarimetric observations of SiO masers help us to understand the magnetic field strength and morphology and to distinguish between conflicting polarization theories. The 43 GHz SiO maser observations of the OH/IR star OH 44.8-2.3 were performed with the VLBA in full polarization spectral line mode. Auxiliary EVLA observations were performed to allow for the absolute calibration of the polarization angle. The Zeeman splitting was measured by cross correlating the right and left circular polarization spectra as well as the S-curve fitting. Additionally, we analyzed the 1612 MHz OH maser observations of OH 44.8-2.3 from the VLA archive. The SiO masers of OH 44.8-2.2 form a ring located at ∼5.4 AU around the star. The masers appear to be highly linearly polarized with fractional linear polarization up to 100%. The linear polarization vectors are consistent with a dipole field morphology in this star. We report a tentative detection of circular polarization of ∼0.7% for the brightest maser feature. The magnetic field measured for this feature corresponds to 1.5±0.3 G. Additionally, the distribution of the 1612 MHz OH maser emission could indicate an elongated morphology. The SiO masers in OH 44.8-2.3 exhibit a ring morphology. Even though the central AGB star of OH 44.8-2.3 is expected to be larger than typical Mira variables, the SiO masers occur at the similar distance from the stellar photosphere as Mira variables. The SiO masers and the 1612 MHz OH maser emission suggest a mildly preferred direction of the outflow in the CSE of this star. Significant linear polarization is measured for the SiO region of this star, which could originate from either collisional or radiative pumping. In any case, the observed polarization is also consistent with magnetic field structures along the preferred outflow direction. This could reflect the possible role of the magnetic field in shaping the circumstellar environment of this object. Although we cannot firmly distinguish between the different polarization theories, the derived magnetic field strength assuming standard Zeeman emission is fully consistent with other maser polarization measurements.

6.1 Introduction

SiO maser emission associated with Asymptotic Giant Branch (AGB) stars occurs at the inner region of Circumstellar Envelopes (CSEs). Maser emission has been detected in several vibrational transitions of the SiO molecule (e.g. Humphreys et al. 1997, Pardo et al. 1998, Soria-Ruiz et al. 2007). A series of very long baseline array (VLBA) high resolution observations of the SiO masers around Mira variables have shown that the maser emission is confined to a region, sometimes ring-shaped, between the stellar photosphere and the dust formation zone (e.g. Cotton et al. 2008, 2006, Diamond et al. 1994). On scales probed by the very long baseline interferometry (VLBI), the masers are confined to localized spots with lifetime of a few months. The resolution of the VLBI observations of SiO masers is a small fraction of the ring. The above points imply that SiO masers can be used as powerful probes of the processes that drive the mass loss and dynamics in the inner region of the CSEs.

SiO masers can also be important for understanding the evolutionary path from the spherically symmetric AGB stars to aspherical Planetary Nebulae (PNe). Magnetic fields likely play an important role in shaping the CSEs of evolved stars (e.g. Garcia-Segura 1997). Polarization observations of circumstellar masers enable us to determine the magnetic field strength and morphology at different distances from the central stars. Observations indicate that SiO masers are significantly linearly polarized, with polarization vectors mainly tangential to the maser ring. For example, multi-epoch polarization VLBA observations of the Mira star TX Cam revealed the linear polarization morphology tangential to the projected shell of SiO maser emission (e.g. Kemball et al. 2009). However, Cotton et al. (2008), observed five Mira variables with the VLBA at 43 GHz, but not all sources showed a tangential linear polarization morphology. It remains therefore unclear whether the tangential linear polarization morphology is a generic property of the SiO maser region of evolved stars. The circular polarization of the masers is in the range 3%-5% (e.g. Barvainis et al. 1987, Kemball et al. 2009). Polarimetric observations of a sample of evolved stars indicate an average magnetic field of several gauss (Herpin et al. 2006, Kemball & Diamond 1997). The SiO maser magnetic fields are consistent with those measured using H_2O and OH masers further out in the envelope assuming a dipole ($B \propto r^{-3}$) or solar-type ($B \propto r^{-2}$) magnetic field (Vlemmings et al. 2005).

VLBI studies of SiO masers have so far focused on Mira variables and a handful of post-AGB objects and water fountain sources (e.g. Cotton et al. 2008, Desmurs et al. 2007, Imai et al. 2005), and as far as we can tell no high resolution VLBI observation has been performed to image SiO masers in OH/IR stars. These objects have larger CSEs and much longer periods up to 2000 days compared to those of Mira variables (Herman & Habing 1985b). They are strong 1612 MHz OH maser emitters (Baud et al. 1979). The stars are surrounded by thick dust shells which makes them optically obscured. The SiO maser pump mechanism in OH/IR stars may be different from that operating in Mira variables (Doel et al. 1995). Due to the higher mass-loss of these objects the CSE is denser at least an order of magnitude more than those of Mira variables.

Here, we report the SiO maser polarimetric observations of the OH/IR star OH44.8-2.3 with the VLBA. The observations enable us to obtain the spatial distribution of the SiO maser features in OH/IR stars for the first time. Additionally, our experiment probes the magnetic field strength and morphology in the SiO maser region of OH/IR stars and compares them with those of Mira variables. We also reduced the 1612 MHz OH maser observations of this star from the VLA archive in order to determine whether there exists any large scale asymmetry in the OH maser shell of this star.

OH 44.8-2.3 is identified as a moderate OH/IR star with a warm and thin CSE and a period of 534 days (Groenewegen 1994). The mass loss of this star is estimated to be ~4.6×10^{-6} M$_\odot$ yr^{-1} (de Beck et al. 2010). The OH masers of this source show a double peak profile at -88.9 and -53.8 km s^{-1} with a peak flux density of 14.4 Jy for the red shifted part of the spectrum (Engels & Jiménez-Esteban 2007). A distance of 1.13±0.34 kpc was measured for this star using the phase-lag method based on the characteristic 1612 MHz double peak profile of the OH masers of this source (Van Langevelde et al. 1990). The H$_2$O masers of this star were detected by Engels et al. (1986) at ~5 Jy. However, further single dish monitoring of this source did not result in any detection (Shintani et al. 2008, Kim et al. 2010). The v=1, $J = 1 \rightarrow 0$ SiO masers of this star were observed by Nyman et al. (1998) with a flux density of 17.6 Jy. Kim et al. (2010) observed the v=1, 2 , $J = 1 \rightarrow 0$ emission from this star with an integrated flux density of ~25 Jy and ~28 Jy, respectively.

The outline of the paper is as follows: the observations are described in Sec. 6.2. Before giving the results in Sec. 6.4, we introduce the necessary background on maser polarization in Sec. 6.3. We discuss the interpretation of the results in Sec. 6.5. This is followed by conclusion in Sec . 6.6.

6.2 Observations

We observed the v=1, $J = 1 \rightarrow 0$ SiO maser emission toward OH 44.8-2.3 on 6 July 2010 using the NRAO [1] Very Long Baseline Array (VLBA) operating in the 43 GHz band. Additionally auxiliary Extended Very Large Array (EVLA) interferometer observations were performed on 2 July 2010 and 11 July 2010 to allow for the absolute calibration of the electric vector polarization angle (EVPA). Furthermore, we retrieved the 1612 MHz OH maser very large array (VLA) observations of OH 44.8-2.3 from the NRAO archive. The VLBA, EVLA and VLA observations are discussed below:

6.2.1 VLBA observations and reduction

The data were recorded in dual circular polarization spectral line mode, which generates all four polarization combinations in the correlator. The DiFX correlator was used with a bandwidth of 4 MHz and 1024 spectral channels, which results in 0.03 km s^{-1} spectral resolution. The observations were performed in one spectral window centered at a fixed frequency corresponding to the v=1, $J = 1 \rightarrow 0$ SiO maser transition at a rest frequency of 43.12208 GHz and a stellar velocity of -72 km s^{-1} with respect to the local standard of rest (LSR), determined from OH maser observations. The total observing time was 6 hr, balanced between the target source, OH 44.8-2.3, and the continuum calibrators, J2253+1608, J1751+0939 and J1800+3848. We achieved a spatial resolution of 0.5×0.2 mas.

We used the Astronomical Image Processing Software Package (AIPS) to perform the rest of the calibration, editing and imaging of the data. The first calibration steps were performed on the data set with modest spectral resolution (128 channels). The solutions were then applied to the high spectral resolution data set (1024 channels). Parallactic angle corrections were performed on all calibrators. The North Liberty (NL) and Saint Croix (SC) antennas had to be flagged due to the bad

---

[1] The National Radio Astronomy Observatory (NRAO) is a facility of the National Science Foundation operated under cooperative agreement by Associated Universities, Inc.

weather conditions at the time of the observations.

Since the SiO molecule is non-paramagnetic, the fractional circular polarization will be small ($m_c \sim$ 1% − 3%). In order to preserve the low stokes V signature, we performed amplitude calibration of OH 44.8-2.3 using the AIPS task 'ACFIT'. In this method, each circular polarization autocorrelation spectrum was calibrated independently using the method described by Reid et al. (1980). A template auto correlation spectrum was selected for ∼20 min interval from the Los Alamos antenna at a time range with sufficiently high elevation. The template spectrum was fitted to all other total power spectra from all antennas and the relative gains of the antennas as a function of time were determined. We used the system temperature measurements provided with the data to perform the amplitude calibration for the calibrators.

The complex band pass solutions were obtained using J2253+1608 on each data set separately. Fringe fitting for the residual relay and rate for the parallel hand data was done using the continuum calibrators J2253+1608 and J1751+0939. The fringe rate solutions for OH 44.8-2.3 were determined on the strongest feature. The delay offset between the right and left circular polarizations was determined for J2253+1608 on the Los Alamos - Fort Davis baseline. The solutions were transferred to all other baselines and sources. The polarization leakage terms were determined using J2253+1608. After the solutions were applied to both data sets image cubes could be created with 50 μarcsec pixel spacing. The rms noise in the modest spectral resolution and the high spectral resolution individual channel images corresponds to 8 mJy and 26 mJy, respectively.

6.2.2 EVLA observations and reductions

The absolute phase difference between the right and left circular polarizations at the reference antenna is not known, which implies that the absolute EVPA of linearly polarized emission cannot be measured accurately in our VLBA observations. Therefore, auxiliary EVLA observations were performed to measure the absolute polarization angle of the polarization calibrators with respect to a primary polarization calibrator with known polarization angle.

The continuum sources J2253+1608 and J1751+0939 were observed as transfer calibrators on 2 July 2010 and 11 July 2010, respectively. The observations were performed in continuum mode and full polarization, using two 128 MHz spectral windows. The data reduction was performed for each spectral window separately. We achieved a beam size of 2.6×1.7 arcsec during the observations.

We reduced the data according the standard EVLA data calibration and imaging recipe in the appendix of AIPS Cook Book. Since the delays are not set accurately in EVLA observations, we solved for the phase slope using the AIPS task FRING. A ∼1 min solution interval was chosen on J2253+1608 and J1751+0939 to solve for the phase slope as a function of frequency. The bandpass solutions were determined using J2253+1608 and J1751+0939. The flux density of the primary flux calibrators 3C286 and 3C48 was determined using the model provided within the AIPS software. The AIPS task 'CALIB' was used to perform phase calibration for 3C286 and 3C48 using a model of the sources. Subsequently, the phase solution was determined for the secondary calibrators J2253+1608 and J1751+0939. The amplitude of the secondary calibrators was adjusted with respect to the flux density of the primary flux calibrator. We used 3C286 and 3C48 for polarization calibration. The delay difference between the right and left circular polarizations were determined using the AIPS task 'RLDLY'. The feed parameters for each polarization were determined both in continuum and spectral mode since the EVLA feeds have significant variations in frequency.

Images were produced in each spectral window in Stokes Q, U, I adopting a pixel spacing of 0.2 arcsec. The rms noise for J2253+16 and J1751+9839 were ~8 mJy and ~1 mJy, respectively.

The absolute EVPA of J2251608 and J1751+0939 were measured with respect to 3C48 and 3C286, respectively. The final absolute EVPA was calculated as the mean of the EVPA in each spectral window. This corresponds to the measured EVPA of 62° and -44° for J2253+1608 and J1751+0939, respectively. Fig. 6.1 shows the EVPA of the linearly polarized emission for J2253+1608 for both EVLA and VLBA observations. The EVPA in the VLBA image is rotated by 15°, which corresponds to the difference in the EVPA between the EVLA and VLBA images. We note that the linearly polarized emission of the other polarization calibrator, J1751+0939 shows two polarized components separated by ~90° in the VLBA image. Therefore we were not able to use this source as an EVPA calibrator.

6.2.3 VLA observations of the 1612 MHz OH masers of OH 44.8-2.3

We found the previous observations of the 1612 MHz OH masers of OH 44.8-2.3 observed on 25 September 1983 using the Very Large Array (VLA) from the NRAO archive. The observations were performed under the project name 'AH127' in the A configuration with the largest spacing of 36.5 km, which gives a resolution of 1″. The band width of 1.5 MHz was used for the observations which gives a velocity resolution of 1.4 km s^{-1} at 1612 MHz. 3C286 was observed as a flux density calibrator and 1741-038 was used as the secondary phase calibrator. The data reduction was performed following the recipe provided in the AIPS cookbook.

Fig. 6.2 displays the OH maser map of OH 44.8-2.3. The emission covers a velocity range of -87 to -56 km s^{-1}. The figure shows the blue- and red-shifted peaks as well as emission summed over several channels close to the stellar velocity.

6.3 SiO maser polarization theory

The SiO maser emission at 43.12208 GHz involves the rotational transition $J = 1 \rightarrow 0$ in the excited vibrational state v=1. Since the SiO molecule is non-paramagnetic, its response to the magnetic field is weak. This implies that the Zeeman splitting is smaller than the line width.

6.3.1 Linear polarization

SiO masers present high fractional linear polarization (e.g. Kemball & Diamond 1997). It was shown that anisotropic background radiation from the central star generates anisotropic pumping, potentially producing a high degree of linear polarization in the SiO emission region (e.g. Watson 2002). In the case where the SiO masers are collisionally pumped, the magnetic sub states may be anisotropically populated, which can generate high linear polarization fraction for saturated masers Western & Watson (1983). However, the results from Nedoluha & Watson (1990) show that the polarization vectors still trace the direction of the magnetic field despite the fact that the linear polarization may originate largely from anisotropic pumping.
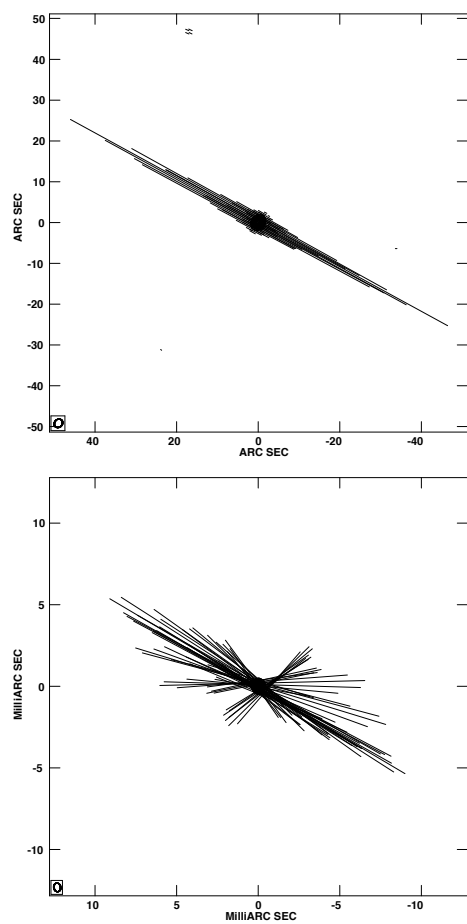
Figure 6.1 – Linearly polarized map of the polarization calibrator J2253+16 obtained with the EVLA (top panel) and the VLBA (bottom panel). The vectors are rotated by 15° in the VLBA image.
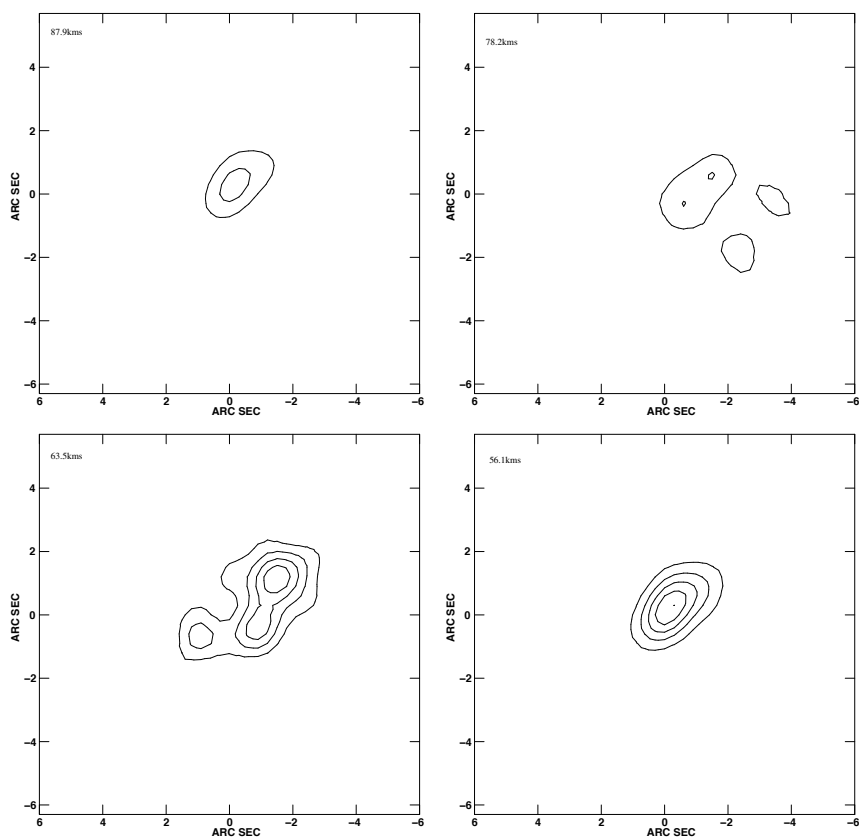
Figure 6.2 – The 1612 MHz OH maser map of OH 44.8-2.3 obtained with the VLA. The top-left and bottom-right panels show the blue- and red-shifted peaks. The red-shifted peak exhibits the highest flux density of 8.1 Jy. The contour levels are at 1.62, 3.24, 4.86, 6.48 and 8.1 Jy. The top-right and bottom-left panels exhibit emission summed over several channels close to the stellar velocity. The contour levels are at 0.005, 0.011, 0.016, 0.022 and 0.027 Jy. The star symbol indicates the position of the peak in the red-shifted emission which likely indicates the position of the central star.

6.3.2 Potential non-Zeeman effects for circular polarization

The non-Zeeman mechanism prohibits one to interpret circular polarization as a measure of the magnetic field strength. This stems from the competition between the stimulated emission rate (R), the Zeeman coefficient rate (gΩ) and the radiative decay rate (Γ). The circular polarization can be created by the change of the axis of symmetry for the molecular quantum states when the condition g$\Omega \simeq R > \Gamma$ is satisfied (Nedoluha & Watson 1994). For some distance along the maser path g$\Omega \geq R$ is satisfied and the magnetic field is the quantization axis. As the radiation propagates farther into the maser path and the rate of stimulated emission becomes larger, the inequality R $\geq$ gΩ is satisfied and the molecule interacts more strongly with the radiation. This implies that the axis of the symmetry of the molecule changes from parallel to the magnetic field to parallel to the direction of propagation. The resulting circular polarization would have the anti-symmetric profile which resembles to that produced by the ordinary Zeeman effect. The intensity dependent circular polarization can be higher than that created by the Zeeman effect by a factor as large as 1000. This scenario is an inherent part of the radiative transfer process and does not require anisotropic pumping or high fractional linear polarization.

Wiebe & Watson (1998) introduce yet another non-Zeeman effect in which the propagation of a strong linear polarization can create circular polarization if the condition $g\Omega \gg R > \Gamma$ is satisfied. The circular polarization can be generated if the magnetic field orientation changes along the maser propagation direction. The circular polarization produced from this scenario is on average $\sim \frac{m_l^2}{4}$ where m_l indicates the linear polarization fraction. For a typical linear polarization fraction of 30%, the circular polarization results from the formula above corresponds to ~2-3% which is in agreement with the observed circular polarization (e.g. Barvainis et al. 1987), however in individual maser features the circular polarization fraction can go up to ~20%. This mechanism would then generate circular polarization with only 10 - 20 mG fields. Moreover, if there is no velocity gradient along the maser path, the circular polarization profile would have the shape of the S-curve. However, the intrinsic profiles can be distorted as a result of saturation, together with velocity and magnetic gradients along the amplification path. A correlation between the linear and circular polarization fraction is expected for the individual features.

6.4 Results

6.4.1 Total intensity

Fig. 6.3 shows the total intensity spectrum of the SiO maser emission towards OH 44.8-2.3. The emission covers a velocity range of ~7 km s^{-1}. The SiO emission actually implies a stellar velocity 3-4 km s^{-1} offset from the stellar velocity of -72 km s^{-1} based on OH maser observations of this star. Fig. 6.4 displays the SiO maser emission map of OH 44.8-2.3 summed over all velocity channels covering emission. The maser features form a partial ring of 4.75 mas corresponding to 5.4 AU assuming a distance of 1.13 kpc (Van Langevelde et al. 1990). The masers appear to be absent from the North-East and South-West part of the ring. The ring pattern observed in the SiO maser region of this star implies that the masers are tangentially amplified. This is typically interpreted to indicate that large velocity gradients exist in the SiO maser region which prohibits radial amplification. The peak flux density for the maser features are displayed in Table 6.1. Feature 1 exhibits the largest
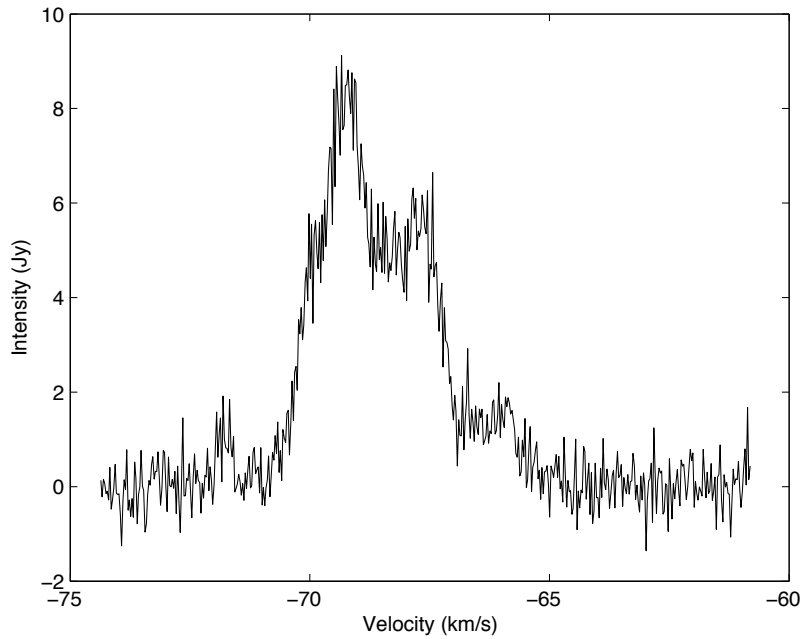
Figure 6.3 – The total intensity spectrum of OH 44.8-2.3 for the v=1, $J = 1 \rightarrow 0$ SiO maser emission obtained with the VLBA.

flux density of 2.8 Jy.

6.4.2 Linear polarization

The polarization morphology is shown in Fig. 6.5. In this plot, the polarized emission is plotted as vectors with a length proportional to the polarization intensity. The position angle of the vectors corresponds to the EVPA of the emission. All stokes parameters are summed over frequency before making this plot. The background contours represent the total intensity image. The fractional linear polarization for the individual maser features is shown in Table 6.1. The average linear polarization fraction for the SiO maser features of this star is ~30%. In particular for feature 8 it reaches 100%. This likely implies that the (radiative or collisional) pumping of SiO masers is not isotropic.

6.4.3 Circular polarization

The instrumental gain differences between the RCP and LCP spectra, can cause a residual scaled down of the stokes I to appear in the circular polarization profile. The Zeeman splitting for the
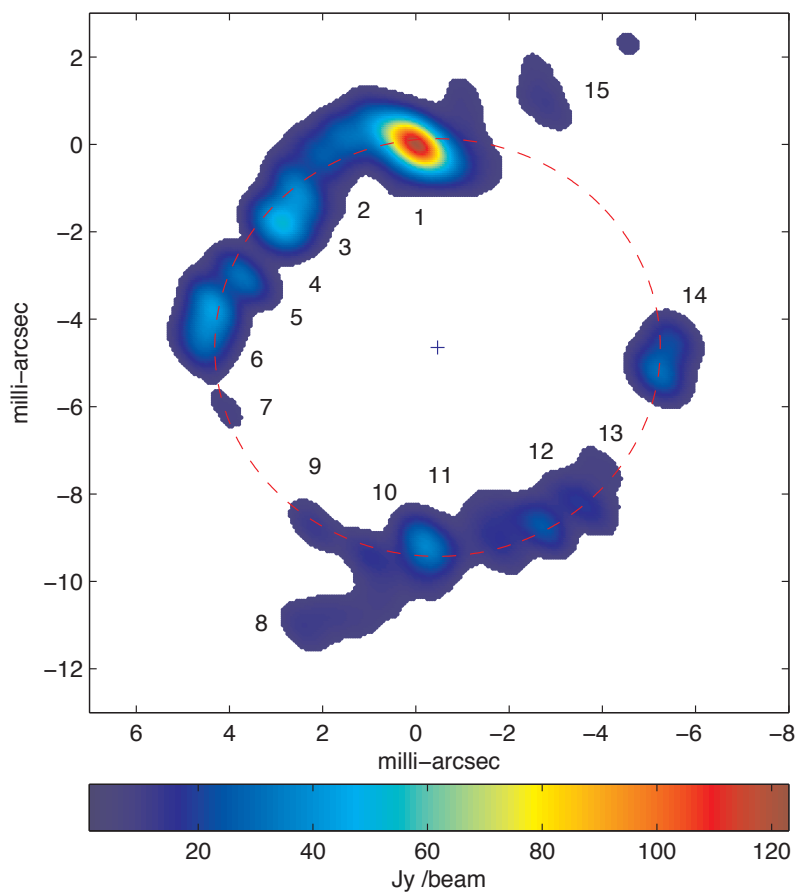
112

Figure 6.4 – The VLBA map of v=1, $J = 1 \rightarrow 0$ SiO maser emission towards the OH/IR star OH 44.8-2.3. The features are color coded according to the flux density (Jy / beam) integrated over all velocity channels.
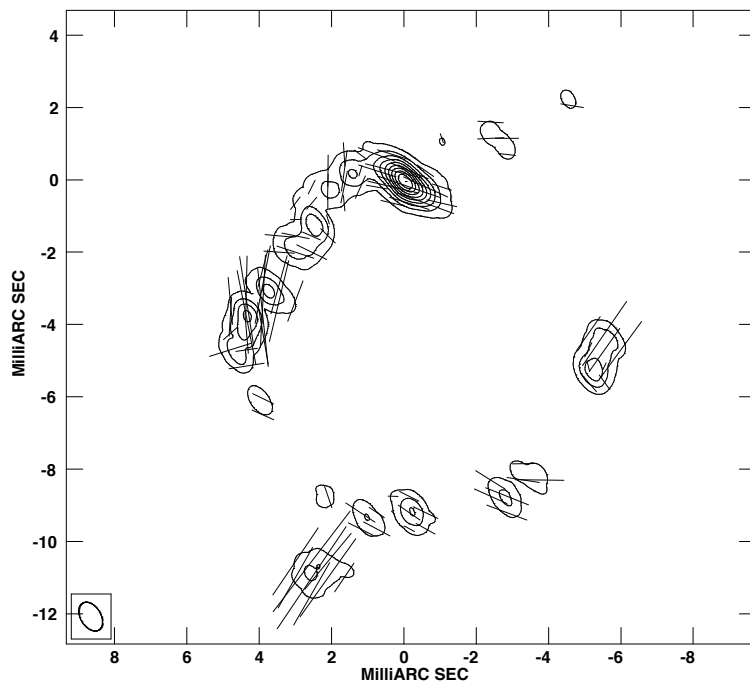
Figure 6.5 – Contour plot of the Stokes I image at levels [1, 2, 5, 10, 20, 40, 80, 100]% of the peak. Vectors are overlaid proportional to the linearly polarized intensity (on a scale 1 mas = 1.25 Jy beam^{-1}) and drawn at a position angle of the EVPA. All Stokes parameters (I,Q,U) are summed over velocity.

feature	RA	Dec	V	I	m_l	B
	19 21	09 27	km s^{-1}	Jy	%	G
1	36.63700337	56.5199500	-69.4	2.9	8	1.5 ± 0.3
2	36.63710476	56.5203000	-69.8	0.7	26	< 3
3	36.63722303	56.5180500	-67.8	0.5	23	< 9
4	36.63725683	56.5169000	-65.9	0.9	36	< 3
5	36.63728386	56.5161500	-67.7	1.2	34	< 2
6	36.63731427	56.5152000	-68.3	0.7	48	< 2.5
7	36.63727710	56.5141000	-66.6	0.3	50	< 3
8	36.63717234	56.5091500	-70	0.6	100	< 2.7
9	36.63715545	56.5113500	-68.7	0.4	50	< 12
10	36.63706420	56.5106000	-71.2	0.6	42	< 3
11	36.63698310	56.5111500	-67.2	0.6	18	< 36
12	36.63680399	56.5109500	-67.7	0.5	30	< 6
13	36.63673641	56.5116000	-67.9	0.3	69	< 7
14	36.63661475	56.5156000	-69.0	0.7	46	< 2.5
15	36.63682427	56.5214500	-69.2	0.24	-	< 12

Table 6.1 – Results of the Magnetic fields determination of the SiO maser features of OH 44.8-2.3 obtained from the VLBA observations.

stokes V spectra of the SiO maser features of OH 44.8-2.3 can be determined by measuring the residual curve having the shape of the derivative of the total intensity spectrum in the least square sense (Troland & Heiles 1982):

$$V(\nu) = a \times \frac{dI}{d\nu} + b \times I(\nu) \tag{6.1}$$

Where a is the measure of the circular polarization due to the Zeeman splitting and b denotes the instrumental polarization term. This method assumes that intrinsically equal flux is present in the RCP and LCP spectra, which implies that the circular polarization spectra have the antisymmetric S-curve pattern. However, theoretical models of circular polarization produce asymmetric profiles depending on the velocity gradient along the amplification path (Wiebe & Watson 1998). We find a tentative detection of the circular polarization for the brightest maser feature in Fig. 6.4 (feature 1 in Table 6.1). Fig. 6.6 displays the circular polarization together with the total intensity spectra for this feature. The figure also shows the fit to the circular polarization profile after removing the scaled down replica of stokes I. The circular polarization fraction is measured as:

$$m_c = \frac{V_{max}}{I_{max}} \times 100 \tag{6.2}$$

Where V_{max} corresponds to the maximum of the fit to the observed stokes V spectrum (Eq. 6.1: $a \times \frac{dI}{d\nu}$). For the modest spectral resolution data (128 channels), we measure circular polarization of $m_c \sim 0.7 \pm 0.2\%$. However, due to the increased noise in individual channels in the high spectral resolution data, we can not confirm the detection. The magnetic field derived from circular
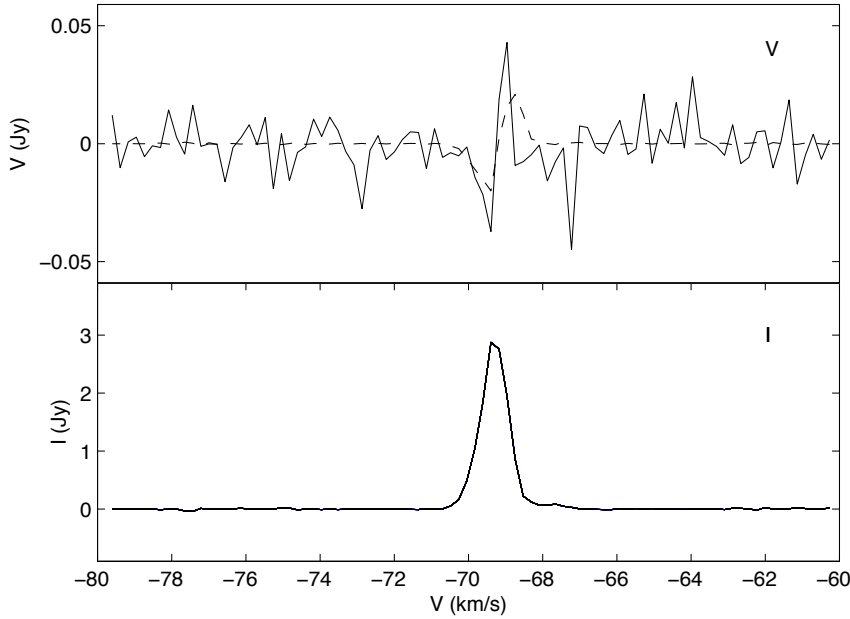
Figure 6.6 – Total power (I) and circular polarization (V) spectra of the brightest SiO maser feature
of OH 44.8-2.3 (feature 1 in Table 6.1). The dashed line is the fit to the observed V-spectrum . The
V spectrum is shown after removing the scaled down replica of stokes I.

polarization corresponds to the following equation (Kemball & Diamond 1997):

$$B = 3.2 \times m_c \times \Delta\nu_D \times \cos\theta \qquad (6.3)$$

Where m_c, $\Delta\nu_D$ and θ indicate the fractional circular polarization, the maser line width and the angle
between the magnetic field and line of sight, respectively. The full width half maximum line with
for the stokes I spectrum of feature 1 corresponds to ~ 0.8 km s^{-1}. Using the preceding relation a
magnetic field of 1.8±0.5 G is derived for feature 1.

6.4.3.1 Cross-correlation method and magnetic field strength

Alternatively, we use the cross-correlation method introduced by Modjaz et al. (2005) to measure
the magnetic field due to the Zeeman splitting. In this method the right circular polarization (RCP)
and the left circular polarization (LCP) spectra are cross-correlated to determine the velocity split-
ting. The magnetic field is determined by applying the Zeeman splitting coefficient for SiO masers.
This method can even work for complex spectra, assuming that the velocity shift is the same over
the spectrum; which means the magnetic field strength and direction is constant in the maser region.

The sensitivity of this method is comparable to the S-curve method, where the stokes V spectrum is directly used for measuring the magnetic field (e.g. Vlemmings et al. 2001, Fiebig & Guesten 1989).

The Zeeman rate for SiO is given by Nedoluha & Watson (1990) as:

$$\frac{g\Omega}{2\pi} \sim 200 \left(\frac{B}{G}\right) \, s^{-1} \tag{6.4}$$

The equation above implies the Zeeman splitting coefficient for the $J = 1 \rightarrow 0$, v=1 transition of the SiO maser as 8.7×10^{-3} km s^{-1} G^{-1}. We present the result of the cross-correlation method in Table 6.1. We measured a magnetic field of 1.5 ± 0.3 G for feature 1. However, for the other features of the SiO emission of this star we only place upper limits at 3σ level.

6.4.4 OH maser observations of OH 44.8-2.3

The VLA results on OH 1612 MHz emission from OH 44.8-2.3 were not presented directly in the scientific literature before, although the original distance determination in Herman et al. (1986) and the one we use from Van Langevelde et al. (1990) depend directly on it. We have access to the results of the original analysis in which a shell radius of 1.302" ± 0.023" was obtained (van Langevelde, private communication). The new processing we performed gave consistent images with these previous results, but we note that the OH at intermediate velocities is quite elongated (Fig. 6.2). The inferred size of the region is of course much larger than the SiO, spanning ~1471 AU compared to 5.4 AU. One should note that with typical outflow velocities of ~16 km s^{-1} and 5 km s^{-1} for OH and SiO masers, the dynamical timescales are also much different: ~440 years for the OH and ~5 years for the SiO.

6.5 Discussion

6.5.1 Linear polarization

In order to the compare the two conflicting polarization theories (a magnetic versus anisotropic pumping origin of the linear polarization implying a Zeeman or non-Zeeman origin of the circular polarization), we need to determine in which theoretical regime the masers were observed. This includes the determination of the stimulated emission rate (R), the Zeeman rate ($g\Omega$), and the collisional and radiative decay rate Γ. The radiative decay rate for the v=1, $J = 1 \rightarrow 0$ transition of the SiO molecule is estimated to be 5 s^{-1} (Kwan & Scoville 1974, Elitzur 1992). The stimulated emission rate (R) is estimated by (Kemball et al. 2009).

$$R = 23 \left(\frac{T_B}{2 \times 10^{10} \, K}\right) \left(\frac{d\Omega}{10^{-2} \, sr}\right) s^{-1} \tag{6.5}$$

Where T_B is the maser brightness temperature and $d\Omega$ is the estimated maser beaming angle. We obtained an estimate for the brightness temperature for feature 1 (Table 6.1) as 5×10^{10} K. We adapt an estimated beaming angle of 10^{-2} sr (Kemball et al. 2009). Replacing these values in eq. 6.5 results in R=57.5 s^{-1}. Substituting the value of ~1.5 G obtained for feature 1 (Table 6.1) in eq. 6.4,

implies $g\Omega \sim 1900$ s^{-1}. Therefore, we are in a regime where $g\Omega \gg R > \Gamma$. In this regime the linear polarization vectors appear either parallel or perpendicular to the projected magnetic field, depending on the angle between the magnetic field direction and the line of sight (Goldreich et al. 1973). Taking the EVPA of -50° for feature 8 which has the highest linear polarization fraction, this implies that the magnetic field direction is either parallel ($-50°$) or perpendicular ($40°$) to the linear polarization vectors. In either cases, the EVPA vectors likely indicate a large scale magnetic field in the SiO maser region of this star.

The linear polarization morphology of this star is not consistent with the dominant tangential polarization morphologies that were reported for other evolved stars (e.g. TX Cam; Kemball et al. 2009). Based on previous observations of the SiO maser region of TX Cam (Kemball & Diamond 1997, Desmurs et al. 2000), they conclude that the tangential polarization morphology could be an inter cycle property of the SiO maser emission toward this star. Instead of tangential polarization morphology, the EVPA vectors could indicate a bipolar magnetic field morphology for the SiO maser region of OH 44.8-2.3 (Fig. 6.5). However, we can not rule out the other, more complex, morphologies. Polarimetric observations of the OH and H$_2$O masers of this star are required to clarify the magnetic field morphology of this star. A dipole field morphology is reported for the supergiant VX Sgr using the polarimetric observations of high frequency SiO masers (Vlemmings et al. 2011). This morphology was consistent with the the dipole magnetic field inferred from H$_2$O and OH maser regions at much larger distances from the central star (Szymczak & Cohen 1997, Szymczak et al. 2001, Vlemmings et al. 2005).

6.5.1.1 The effects of anisotropic pumping

The SiO maser features of this star exhibit high fractional linear polarization up to 100% (Table 6.1), which likely indicates that the pumping of the masers is highly anisotropic. Such high linear polarization fractions were reported previously (Kemball & Diamond 1997, Cotton et al. 2006). The masers occur close to the central star and the infrared radiation incident on the masering region is highly anisotropic. This implies that the magnetic sub states are pumped unequally. Additionally, the medium in which they are located likely has large velocity gradients, which leads to preferred direction for the propagation of masers (Watson 2002). Western & Watson (1983) show that even for collisionally pumped SiO masers, the magnetic sub states are anisotropically pumped and high linear polarization would be expected for saturated and unsaturated masers. In the absence of magnetic fields, collisional pumping causes linear polarization along the radial direction. In contrast, radiative pumping would produce linear polarization vectors tangential to the SiO maser ring. However, our observations show that magnetic fields are present in the SiO maser ring of OH 44.8-2.3, which implies that both magnetic field and anisotropic pumping influence the linear polarization morphology. Therefore, we can not distinguish between the radiative or collisional pumping from the observations.

6.5.1.2 Maser saturation

The degree of saturation is the ratio of the rate R for stimulated emission to the loss rate Γ. From the observations we measured the stimulated emission rate for feature one as R$\sim$57.5 s^{-1} which implies $\frac{R}{\Gamma} \sim 10$. This indicates that the medium is marginally saturated. In contrast, a saturation of $\frac{R}{\Gamma} \sim 30$ is required to achieve 70% linear polarization fraction in the non-Zeeman scenario (Watson & Wyld

118

2001). In the standard Zeeman interpretation scenario proposed by Elitzur (1996) the polarization solution does not depend on the saturation level. Nedoluha & Watson (1994) show that the low level circular polarization observed for SiO masers can be due to the saturation of masers.

6.5.1.3 Jet-like features

Even though the majority of the SiO maser features of OH 44.8-2.3 are coherent and fit the ring model, features 8 and 15 do not conform with the ring pattern. A striking characteristic of feature 8 is the 100% linear polarization fraction. Additionally, the linear polarization vectors of this feature are in the perpendicular direction of the overall linear polarization morphology of this star (Fig. 6.5). Cotton et al. (2006) report structures aligned with the direction of the photosphere with magnetic field morphology along the features. They refer to them as jet-like features. They explain that these features likely form due to the masering region being dragged along the magnetic field. For the case of OH 44.8-2.3, the 100% linear polarization fraction could imply that this feature is a dynamic part of the envelope. Observations of this feature close in time to study the proper motion is necessary to understand the nature of this feature.

6.5.2 Circular polarization

We report a tentative detection of ~0.7% for the circular polarization fraction for feature 1 (Table 6.1). The measured magnetic field corresponds to 1.5±0.3 G for this feature. We note that the magnetic field measured from the circular polarization fraction (Sec. 6.4.3:1.8±0.5 G) and the one measured from the cross-correlation method (Sec. 6.4.3.1: 1.5±0.3 G) are consistent within errors. Therefore the correspondence of the field measured from the cross-correlation method with the field determination through the circular polarization fraction confirms that the cross-correlation method works properly.The non-Zeeman effect due to intensity dependent circular polarization introduced by Nedoluha & Watson (1994) is ruled out since $g\Omega \gg R$ in our observations. However, since we are in a regime where $g\Omega \gg R > \Gamma$ the non-Zeeman effect introduced by Wiebe & Watson (1998) is applicable. For the 7% linear polarization fraction measured for feature 1 (Table 6.1), the generated circular polarization due to this effect is 0.12%. This implies that the measured circular polarization for feature one is about 6 times higher than the estimated value from the non-Zeeman effect. Wiebe & Watson (1998) show that if the circular polarization is higher than the average of $\frac{m_l^2}{4}$, the circular polarization stems from other effects, probably due to the Zeeman effect. Therefore, it is likely that the circular polarization of this star originates from the Zeeman splitting. However, Wiebe & Watson (1998) explain that the average circular polarization in individual features can go up to 20%. Additionally, the determination of Zeeman or non-Zeeman effect from the observed circular polarization profile remains inconclusive, since both models predict the similar anti-symmetric S-curve profile.

6.5.3 CSE morphology and magnetic field

The SiO maser features of OH 44.8-2.3 exhibit two opposite arcs (Fig. 6.4). Additionally, the OH masers of this star show that the masers have an elongated shell morphology in the direction where there is a gap in the SiO maser emission (Fig. 6.2) . We note that the OH masers occur on much

larger scale (~1471 AU) than the SiO masers (5.4 AU) around the star. It is therefore not obvious
that both deviations from symmetry are related, but if they are, this is an indication that there is a
mechanism at work that can support the asymmetry on many scales. Similar gaps or opposite arcs
were seen recently in monitoring observations of the SiO masers of R Cas with the VLBA (Assaf
et al. 2011). Of course, only with one epoch of observations we can not determine whether the
SiO maser arcs in OH 44.8-2.3 are consistent in time since the region where SiO masers occur is
expected to be highly dynamic. Therefore, multi-epoch observations of the SiO masers of this star
is essential to probe the motion of the SiO maser features.

As mentioned earlier, the magnetic field morphology for the SiO maser region of this star is either
parallel or perpendicular to the linear polarization vectors. Interestingly, the direction of the mag-
netic field is parallel or perpendicular to the location of the gaps in the SiO maser ring and the OH
maser extent. There thus appears to be a global preferred direction of the outflow imposed by the
magnetic field in the CSE of this star. Such asymmetric outflows have already been reported for
the CSE of evolved stars. For example, collimated H_2O maser jets have been observed in a class of
post-AGB objects, the so-called water fountain sources (Imai et al. 2002, Boboltz & Marvel 2005).
Additionally, interferometric observations of the OH maser region of this class of objects revealed
aspherical morphologies with either equatorial or bi-conical distributions (Amiri et al. 2011). High
resolution observations of the SiO masers of the post-AGB object W43A indicated a biconical out-
flow (Imai et al. 2005). The bi-polar jets observed in water fountain sources are related to the onset
of asymmetric PNe (Sahai & Trauger 1998).

The high fractional linear polarization observed for the SiO masers of OH 44.8-2.3 together with the
tentative detection of circular polarization is potentially an important indication that magnetic fields
have a significant role in shaping the circumstellar environment of this star. Significant magnetic
fields are observed in different regions of the circumstellar environment of several evolved stars,
which indicate the possible role of the magnetic field in shaping the CSEs. Observations of H_2O
masers revealed significant field strength for Mira variables and supergiants in the range 0.2 G to 4
G (Vlemmings et al. 2002, 2005). In particular, H_2O maser polarimetric observations of the water
fountain source W43A showed that the jet is magnetically collimated (Vlemmings et al. 2006).
Additionally, polarimetric observations of OH masers revealed large scale magnetic field strength
in evolved stars ranging from 0.1 mG to 10 mG (e.g. Etoka & Diamond 2004, Amiri et al. 2010).

However, it should be noted that in interpreting the morphology of the maser emission in terms of
the underlying physical structure a number of aspects have been ignored. This includes sufficient
column density, velocity coherent path length along the amplification path and pumping mechanism.
Therefore, it is possible that both SiO and OH molecules exist in spherical shells but the conditions
for the masers mentioned above are not satisfied.

6.5.4   SiO emission in OH 44.8-2.3

The SiO masers of OH 44.8-2.3 exhibit a ring morphology (Fig. 6.4). Assuming a distance of
1.13±0.34 kpc, the masers are located at a distance of ~ 5.4 AU from the surface of the star. The
ring morphology is similar to the ring patterns observed previously for the SiO masers of Mira
variables (e.g. Diamond et al. 1994). Moreover, the estimated SiO maser ring radius of OH 44.8-
2.3 is similar to those measured for Mira variables (e.g.3-7 AU; Cotton et al. 2008). However, since
OH 44.8-2.3 is a high mass loss OH/IR star, the CSE and stellar radius of this star is expected to
be larger than Mira variables. The typical stellar radius for OH/IR stars corresponds to ~2.8 AU

(Herman & Habing 1985a). This implies that the SiO masers of OH 44.8-2.3 occur at ~1.9 stellar radius. This value is similar to the lower end location of SiO masers in Mira variables (2-6 stellar radius; Elitzur 1992). Therefore, even though OH 44.8-2.3 is expected to be larger, the SiO masers occur at the same distance from the stellar photosphere as Mira variables.

However, the main uncertainty for the discussion above is the distance to the star. From the 1612 MHz OH maser observations of this source using the phase lag method a distance of 1.13±0.34 kpc was measured (Van Langevelde et al. 1990). This method assumes spherical symmetry of the OH maser shell. However, the distribution of the OH masers of this star (Fig. 6.2) does not indicate spherical expansion of the OH maser shell. Therefore, accurate determination of the distance of this source using the parallax method for the SiO maser features of OH 44.8-2.3 are necessary to understand the size and location of the SiO maser region.

6.6 Conclusions

Our observations indicate a ring morphology for the SiO maser region of the OH/IR star OH 44.8-2.3. Assuming a distance of 1.13±0.34 kpc (Van Langevelde et al. 1990), the masers are located at ~ 5.4 AU from the central star. The ring pattern is similar to that observed previously for Mira variables.

The linear polarization morphology is consistent with the dipole magnetic field morphology in the SiO maser region of this star. However, we cannot rule out toroidal or solar type field morphologies. Polarimetric observations of the OH and H_2O maser regions of the CSE of this star are required to clarify the magnetic field morphology of this star.

We report a tentative detection of circular polarization at ~0.7% for the brightest SiO maser feature in the modest spectral resolution data set. However, due to the increased noise in high spectral resolution data set we can not confirm the detection. Further polarimetric VLBI observations of the SiO masers of this star with more integration time are necessary to clarify this. We note that based on polarization studies we can not distinguish between the Zeeman and non-Zeeman effects from the observations.

The SiO maser features of OH 44.8-2.3 exhibit two opposite arcs. Furthermore, the 1612 MHz OH masers of this star indicate an elongated shell morphology in the direction where there is a gap in the SiO maser emission. Additionally, the direction of the magnetic field is parallel or perpendicular to the location of the gaps in the SiO maser ring and the OH maser extent. This could be taken as a clue that there is a large scale magnetic field that imposes a preferred direction on the outflow over scales that span more than two orders of magnitude. Furthermore, the high fractional linear polarization measured for the SiO masers of this star could indicate the possible role of the magnetic field in shaping the circumstellar environment of this star. However, we can not differentiate between the radiative or collisional pumping for the SiO maser ring of OH 44.8-2.3.

Follow up monitoring of the SiO maser region of OH 44.8-2.3 can give the distance through parallax measurements and this source offers a unique opportunity to check the phase-lag distance previously obtained by Van Langevelde et al. (1990). Additionally, the future observations will enable us to check the evolution of asymmetries in the CSE of this star.

Acknowledgements

Nederlandse Samenvatting

De asymptotische reuzentak

Sterren zoals onze zon brengen het grootste deel van hun leven door op de hoofdreeks (of main sequence, zie afbeelding 1). Tijdens dit stadium wordt waterstof omgezet in helium door nucleaire verbranding. Zodra de waterstofvoorraad van de kern is uitgeput ondergaan sterren verschillende verdere evolutionaire stadia. De laatste fase van de evolutie wordt de AGB fase genoemd. De ster bevindt zich dan op de Asymptotic Giant Branch, of asymptotische reuzentak. In deze fase heeft de ster een kern van koolstof en zuurstof omringt door twee lagen van waterstof en helium waar nog steeds kernfusie plaatsvind. Meer dan 90% van alle sterren, inclusief onze zon, zullen een dergelijke AGB fase meemaken. Deze sterren stralen dan 3000 keer meer energie uit dan de zon.

Gedurende de AGB fase verliezen sterren een significante hoeveelheid van hun massa aan het interstellaire medium in de vorm van stellaire winden. Deze uitstroom van materie vormt een mantel rondom de AGB ster: de circumstellaire schil ("circumstellair envelope", CSE, zie Figuur 2). De CSEs bevatten verscheidene moleculen en in het bijzonder moleculen die maser straling produceren op verschillende frequenties in het radiogebied.

Figuur 1 – het Hertzsprung-Russell Diagram. De lijnen in het diagram laten zien hoe de evolutie van een ster verloopt als functie van temperatuur en lichtkracht.
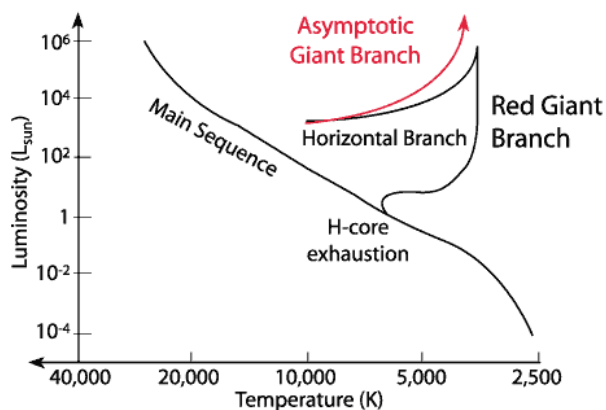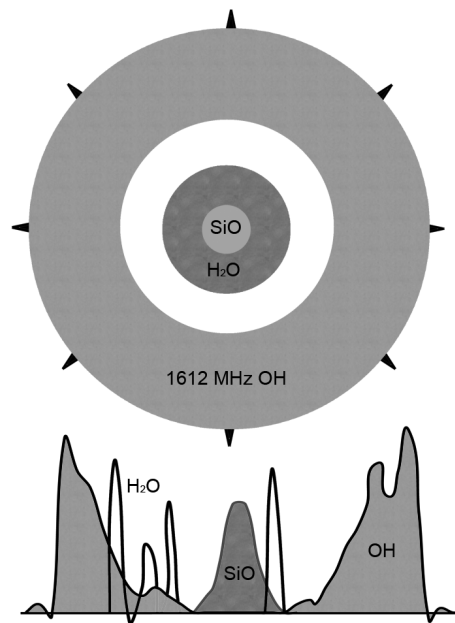
Figuur 2 – Een schematische voorstelling van de CSE van een typische zuurstofrijke AGB ster. SiO masers ontstaan dicht bij de fotosfeer. H_2O masers ontstaan op tussenliggende afstanden. De 1612 MHz OH masers opereren in het buitenste gedeelte van de CSE. Afwijkingen van sferische symmetrie ontstaan waarschijnlijk in de late AGB of de vroege post-AGB fase

Planetaire nevels

Als de nucleaire verbranding in de omringende lagen van waterstof en helium stopt, verandert de centrale AGB ster in een hete witte dwerg. De overgebleven CSE, eerder uitgestoten tijdens de AGB fase, wordt dan een planetaire nevel (PN). De meerderheid van de waargenomen PNs vertonen een verscheidenheid van complexe morfologieën, waaronder elliptische en bipolaire structuren. De non-sferische vormen van PNs kunnen erop wijzen dat de afwijking van sferische symmetrie ontstaat tijdens de overgang van de AGB fase naar de PN fase, de zogenoemde proto-planetaire fase. Om de waargenomen complexe morfologieën van PNs te begrijpen is het dus essentieel om asymmetrieen te bestuderen tijdens de eerdere fases van de CSEs rond AGB sterren. Gecollimeerde uitstromen, of straalstromen, die actief zijn tijdens het vroege proto-PN stadium, zijn voorgesteld als mogelijke oorzaak voor de vorming van bipolaire PNs. Theoretische modellen laten zien dat magnetische velden een belangrijke rol kunnen spelen in het collimeren van de uitstroom. Anderzijds kunnen snelle, gecollimeerde uitstromen worden veroorzaakt doordat de ster zich in een dubbelstersysteem bevindt.

124

Wat is een maser?

Maser staat voor "microwave amplification by stimulated emission of radiation". Dit betekent vrij vertaald: microgolf versterking door gestimuleerde emissie van straling. Een laser is het equivalent van een maser, maar dan voor hogere frequenties in het ultraviolet of het zichtbare gedeelte van het electromagnetisch spectrum. Het natuurkundige mechanisme voor maseremissie is gestimuleerde emissie. Dit is als eerste geïntroduceerd door Einstein in 1917. Figuur 3 illustreert het principe van maseremissie op een schematische wijze. Masers komen van nature in de ruimte voor en verschillende moleculaire soorten kunnen maseremissie vertonen. Dit impliceert dat er gebieden in de ruimte zijn waar de omstandigheden zodanig zijn dat afwijkingen van lokaal thermisch evenwicht (LTE) stelselmatig voorkomen.

In de CSEs van AGB sterren zijn er drie soorten masers die regelmatig voorkomen: SiO, H_2O en OH masers. Figuur 2 laat zien dat de OH masers ontstaan in het buitenste gedeelte van zuurstofrijke CSEs, in een gebied waar fotodissociatie van H_2O moleculen OH produceert. H_2O masers komen voor op tussenliggende afstanden, in een schil die een significante radiële versnelling ondervindt. SiO masers komen voor in een gebied tussen de stellaire fotosfeer en de zones waar stof wordt gemaakt. Masers zijn dus uitstekende middelen om de gasstromen dichtbij de ster te bestuderen.

Astronomische masers kunnen worden waargenomen met een hoge hoekresolutie door middel van radiointerferometrie. Bij deze techniek worden radiogolven met twee of meer radiotelescopen opgevangen die zich op een bepaalde afstand van elkaar af bevinden. De resolutie van een interferometer wordt bepaald door de afstanden tussen de radiotelescopen. Om een afbeelding van goede kwaliteit te krijgen moeten er een groot aantal afstanden tussen zoveel mogelijk verschillende telescopen zijn.

Proto-PN masers

Er is een klasse van PN kandidaten bekend, waarbij hoge snelheid H_2O maser straalstromen ($\sim$ 200 km s^{-1} of meer) zijn waargenomen. Dit is veel groter dan snelheden gemeten bij OH masers. Waarneming van deze H_2O masers (of zogenaamde proto-PN masers) met behulp van interferometrie hebben sterk gebundelde straalstromen laten zien. De waargenomen spatiële verdeling en de spectroscopische eigenschappen van deze klasse van bronnen is niet consistent met wat is waargenomen voor normale AGB sterren. Dit zou kunnen betekenen dat gedurende de post-AGB fase de uitstromen de CSEs beïnvloeden en een indruk achterlaten die zich in een later stadium van de evolutie zal manifesteren als een asymmetrische PN. Dit impliceert dat andere delen van de CSEs van deze objecten (bijvoorbeeld OH and SiO maser schillen) ook afwijkingen van sferische expansie zouden kunnen vertonen. Het bestuderen van CSEs van deze objecten met behulp van hoge resolutie waarnemingen van andere maser soorten op verschillende afstanden van de centrale AGB ster is dus essentieel om te begrijpen hoe asymmetrieen zich ontwikkelen terwijl de ster door de AGB fase evolueert.

125
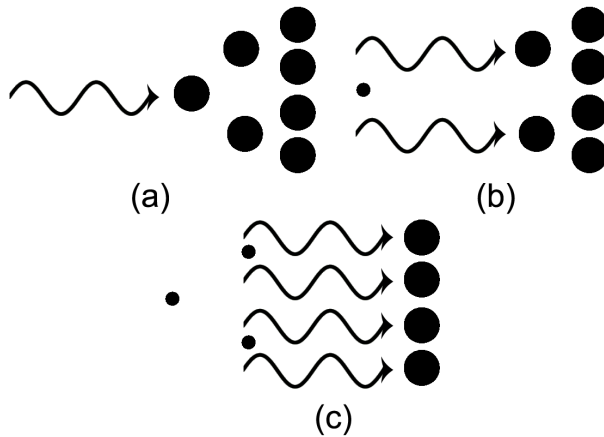
Figuur 3 – Het principe van maseremissie: In alle afbeeldingen zijn de grote cirkels moleculen geëxciteerd naar een hoger energieniveau. De kleine cirkels zijn moleculen in het lage energieniveau. Paneel (a): Het molecuul in het hoge energieniveau wordt gestimuleerd door een foton met golflengte λ. Paneel (b): Het molecuul absorbeert het foton en zendt vervolgens twee fotonen uit om terug te komen naar het lage energieniveau. Deze twee fotonen raken de volgende twee geëxciteerde moleculen wat resulteert in vier fotonen (paneel (c)). Dit proces herhaalt zich en de maser versterkt de straling met golflengte λ exponentieel terwijl de straling door het medium gaat.

Masers als gereedschap om sterevolutie te bestuderen

De circumstellaire masers die zich voordoen in de CSEs van geëvolueerde sterren zijn natuurlijke bakens in de uitstroom op verscheidene afstanden van de centrale AGB ster. Interferometrische waarnemingen van masers maken het mogelijk om de spatiele verdeling van masers in verschillende delen van de CSEs rond AGB en post-AGB sterren te bepalen. Hiermee kunnen we de asymmetrieën bestuderen die onstaan in de AGB/post-AGB fase en vervolgens zullen leiden tot non-sferische PNs. De masers hebben erg hoge helderheidstemperaturen ($\sim 10^9$ K of hoger). Dit maakt hen spectaculaire bronnen voor het doen van interferometrische waarnemingen. Gedurende mijn onderzoek heb ik verschillende interferometer telescopen gebruikt om circumstellaire masers in kaart te brengen met een resolutie tot 0.5 mas. Bovendien zijn polarimetrische waarnemingen van masers de beste methode om magnetische velden in CSEs te bestuderen. Dit kan ons helpen om te begrijpen wat de rol in van magnetische velden in de vorming van CSEs tijdens de AGB fase.

Dit proefschrift

Het onderzoek in dit proefschrift is gericht op waarnemingen van masers rond geëvolueerde sterren. De waarnemingen zijn gedaan met behulp van zowel radiointerferometers als enkelvoudige radiotelescopen. Het doel van het onderzoek is om verscheidene belangrijke vragen te behandelen:

1. Wat is de rol van het magnetisch veld bij het vormen van de circumstellaire omgeving van AGB sterren?

2. Komen sterke magnetische velden regelmatig voor in verschillende klasses van AGB sterren?

3. Komen non-sferische morfologieën regelmatig voor in de CSEs van geëvolueerde sterren?

Hoogtepunten van het proefschrift

- *Hoofdstuk 2 & 3*

  Wij hebben OH maser polarimetrische waarnemingen uitgevoerd van drie proto-PN objecten (W43A, OH 12.8-0.9 en OH 37.1-0.8) met de MERLIN interferometer in het Verenigd Koninkrijk. Het belangrijkste doel van de waarnemingen is te begrijpen of grootschalige magnetische velden bestaan in de circumstellaire omgeving van deze sterren. Wij rapporteren een gemiddeld magnetisch veld van 100, 29 and 360 μG, gemeten voor de OH maser gebieden van W43A, OH 12.8-0.9 en OH 37.1-0.8. De resultaten laten dus zien dat magnetische velden een belangrijke rol kunnen hebben in het vormen van de CSEs van deze sterren. Tevens laten de waarnemingen zien dat er aanwijzingen zijn voor asymmetrische expansie van de OH maser schillen van alle objecten bestudeerd in dit werk.

- *Hoofdstuk 4*

  In dit hoofdstuk presenteren wij H_2O maser polarimetrische waarnemingen van een groep geëvolueerde sterren. Met behulp van deze waarnemingen hebben wij een magnetisch veld gemeten van 18.9 ± 3.8 mG voor de H_2O maser van de OH/IR ster IRAS 19422+3506. Voor de andere bronnen in ons sample stellen wij bovenlimieten van 10-800 mG aan de sterkte van het magnetische veld.

- *Hoofdstuk 5*

  In dit hoofdstuk worden multi-epoch waarnemingen van de H_2O masers van een sample van post-AGB kandidaten gepresenteerd. Deze waarnemingen zijn gedaan met Effelsberg telescoop. Het doel van de waarnemingen was hoofdzakelijk om meer proto-planetaire masers te vinden. Hiermee kan een statistisch significant sample van deze belangrijke overgangsobjecten worden samengesteld. Wij hebben vijf proto-PN kandidaten gevonden. Deze kandidaten hebben opvallende dubbel-piek profielen wat erop kan wijzen dat deze masers plaatsvinden in bipolaire uitstromen.

  Daarnaast hebben wij H_2O masers gedetecteerd bij de 'dood' veronderstelde OH/IR ster IRAS 18455+0448. Dit object wordt gezien als het prototype van een 'dode' OH/IR ster na de snelle verdwijning van de 1612 MHz OH masers. Wij hebben OH maser vervolgwaarnemingen gedaan van deze ster op 1612, 1665, 1667 MHz. De waarnemingen laten zien dat de 1612 MHz OH masers niet opnieuw zijn verschenen samen met de H_2O masers en dat de 1665 en 1667 MHz masers significant zwakker zijn geworden.

- *Hoofdstuk 6* Hierin presenteren wij VLBA waarnemingen van de SiO masers van een geëvolueerde ster met een hoog massaverlies (OH 44.8-2.3). De waarnemingen laten een ring zien. Tevens laat vergelijking tussen de SiO maser ring en de OH maser morfologie van deze ster zien dat de OH masers uitgerekt zijn in de richting waar er een gat is in de SiO maser ring. Ook geeft de polarisatieanalyse een magnetisch veld van 1.5 G voor de SiO masers

127

van deze ster. Over het geheel is het waarschijnlijk dat er een mechanisme is dat asymmetrieën beïnvloed op vele schalen en dat magnetische velden een belangrijke rol spelen in het vormen van de circumstellaire omgeving van deze ster.

Conclusies

De resultaten gepresenteerd in dit proefschrift hebben laten zien dat waarnemingen op hoge resolutie van astrofysiche masers een uniek gereedschap zijn voor het bestuderen van de morfologieën van CSEs in verschillende klasses van AGB sterren. Dit heeft ons geholpen meer te begrijpen van de evolutie van asymmetrieën in CSEs gedurende de AGB fase. Onze waarnemingen hebben laten zien dat asymmetrieën voor kunnen komen in verschillende klasses van geëvolueerde sterren. In het bijzonder geven polarimetrische waarnemingen van de masers de meest directe methode om zowel de sterkte van het magnetisch veld te bepalen, alsook de morfologie op verschillende afstanden van de centrale ster. De polarisatiestudies gepresenteerd in dit proefschrift laten zien dat magnetische velden een significante rol kunnen spelen in het vormen van de circumstellaire omgeving.

References

Alcolea, J., Bujarrabal, V., Sánchez Contreras, C., Neri, R., & Zweigle, J. 2001, A&A, 373, 932

Amiri, N., Vlemmings, W., & van Langevelde, H. J. 2010, A&A, 509, A26+

Amiri, N., Vlemmings, W., & van Langevelde, H. J. 2011, A&A, 532, A149+

Assaf, K. A., Diamond, P. J., Richards, A. M. S., & Gray, M. D. 2011, ArXiv e-prints

Bains, I., Gledhill, T. M., Yates, J. A., & Richards, A. M. S. 2003, MNRAS, 338, 287

Balick, B., Preston, H. L., & Icke, V. 1987, AJ, 94, 1641

Barvainis, R., McIntosh, G., & Predmore, C. R. 1987, Nature, 329, 613

Baud, B., Habing, H. J., Matthews, H. E., & Winnberg, A. 1979, A&AS, 36, 193

Baud, B., Sargent, A. I., Werner, M. W., & Bentley, A. F. 1985, ApJ, 292, 628

Bedijn, P. J. 1987, A&A, 186, 136

Blackman, E. G., Frank, A., Markiel, J. A., Thomas, J. H., & Van Horn, H. M. 2001, Nature, 409, 485

Boboltz, D. A. & Marvel, K. B. 2005, ApJ, 627, L45

Boboltz, D. A. & Marvel, K. B. 2007, ApJ, 665, 680

Bowers, P. F. 1978, A&A, 64, 307

Bowers, P. F. 1991, ApJS, 76, 1099

Bowers, P. F., Claussen, M. J., & Johnston, K. J. 1993, AJ, 105, 284

Bowers, P. F., Johnston, K. J., & Spencer, J. H. 1983, ApJ, 274, 733

Cernicharo, J., Bujarrabal, V., & Santaren, J. L. 1993, ApJ, 407, L33

Chapman, J. M. & Cohen, R. J. 1985, MNRAS, 212, 375

Chapman, J. M. & Cohen, R. J. 1986, MNRAS, 220, 513

Chen, P. S., Szczerba, R., Kwok, S., & Volk, K. 2001, A&A, 368, 1006

Chengalur, J. N., Lewis, B. M., Eder, J., & Terzian, Y. 1993, ApJS, 89, 189

Chevalier, R. A. & Luo, D. 1994, ApJ, 421, 225

Claussen, M., Sahai, R., & Morris, M. 2004, in Astronomical Society of the Pacific Conference Series, Vol. 313, Asymmetrical Planetary Nebulae III: Winds, Structure and the Thunderbird, ed. M. Meixner, J. H. Kastner, B. Balick, & N. Soker, 331–+

Colomer, F., Reid, M. J., Menten, K. M., & Bujarrabal, V. 2000, A&A, 355, 979

Cotton, W. D., Perrin, G., & Lopez, B. 2008, A&A, 477, 853

Cotton, W. D., Vlemmings, W., Mennesson, B., et al. 2006, A&A, 456, 339

Davies, R. D. 1974, in IAU Symposium, Vol. 60, Galactic Radio Astronomy, ed. F. J. Kerr & S. C. Simonson, 275–+

de Beck, E., Decin, L., de Koter, A., et al. 2010, A&A, 523, A18+

Deacon, R. M., Chapman, J. M., Green, A. J., & Sevenster, M. N. 2007, ApJ, 658, 1096

Desmurs, J.-F., Alcolea, J., Bujarrabal, V., Sánchez Contreras, C., & Colomer, F. 2007, A&A, 468, 189

Desmurs, J. F., Bujarrabal, V., Colomer, F., & Alcolea, J. 2000, A&A, 360, 189

Destombes, J. L., Marliere, C., Baudry, A., & Brillet, J. 1977, A&A, 60, 55

References

Diamond, P. J., Kemball, A. J., Junor, W., et al. 1994, ApJ, 430, L61

Diamond, P. J., Norris, R. P., Rowland, P. R., Booth, R. S., & Nyman, L.-A. 1985, MNRAS, 212, 1

Diamond, P. J. & Nyman, L. Å. 1988, in IAU Symposium, Vol. 129, The Impact of VLBI on Astrophysics and Geophysics, ed. M. J. Reid & J. M. Moran, 249–+

Doel, R. C., Gray, M. D., Humphreys, E. M. L., Braithwaite, M. F., & Field, D. 1995, A&A, 302, 797

Elitzur, M. 1990, ApJ, 363, 628

Elitzur, M. 1992, ARA&A, 30, 75

Elitzur, M. 1996, ApJ, 457, 415

Elitzur, M., Hollenbach, D. J., & McKee, C. F. 1989, ApJ, 346, 983

Engels, D. 2002, A&A, 388, 252

Engels, D. & Jiménez-Esteban, F. 2007, A&A, 475, 941

Engels, D. & Lewis, B. M. 1996, A&AS, 116, 117

Engels, D., Schmid-Burgk, J., & Walmsley, C. M. 1986, A&A, 167, 129

Engels, D., Winnberg, A., Walmsley, C. M., & Brand, J. 1997, A&A, 322, 291

Etoka, S. & Diamond, P. 2004, MNRAS, 348, 34

Fiebig, D. & Guesten, R. 1989, A&A, 214, 333

Fish, V. L. & Reid, M. J. 2006, ApJS, 164, 99

Frank, A. & Blackman, E. G. 2004, ApJ, 614, 737

Garcia-Segura, G. 1997, ApJ, 489, L189+

García-Segura, G., López, J. A., & Franco, J. 2005, ApJ, 618, 919

Goldreich, P., Keeley, D. A., & Kwan, J. Y. 1973, ApJ, 179, 111

Griffin, E. 2004, The Observatory, 124, 393

Groenewegen, M. A. T. 1994, A&A, 290, 544

Habing, H. J. 1996, A&A Rev., 7, 97

Herman, J., Burger, J. H., & Penninx, W. H. 1986, A&A, 167, 247

Herman, J. & Habing, H. J. 1985a, Phys. Rep., 124, 255

Herman, J. & Habing, H. J. 1985b, A&AS, 59, 523

Herpin, F., Baudry, A., Thum, C., Morris, D., & Wiesemeyer, H. 2006, A&A, 450, 667

Humphreys, E. M. L., Gray, M. D., Yates, J. A., & Field, D. 1997, MNRAS, 287, 663

Icke, V. 1988, A&A, 202, 177

Icke, V. 2003, A&A, 405, L11

Imai, H., Diamond, P., Nakashima, J.-I., Kwok, S., & Deguchi, S. 2008, in The role of VLBI in the Golden Age for Radio Astronomy

Imai, H., Nakashima, J., Diamond, P. J., Miyazaki, A., & Deguchi, S. 2005, ApJ, 622, L125

Imai, H., Obara, K., Diamond, P. J., Omodaka, T., & Sasao, T. 2002, Nature, 417, 829

Imai, H., Sahai, R., & Morris, M. 2007, ApJ, 669, 424

Jewell, P. R., Dickinson, D. F., Snyder, L. E., & Clemens, D. P. 1987, ApJ, 323, 749

Kemball, A. J. & Diamond, P. J. 1997, ApJ, 481, L111+

Kemball, A. J., Diamond, P. J., Gonidakis, I., et al. 2009, ApJ, 698, 1721

Kim, J., Cho, S., Oh, C. S., & Byun, D. 2010, ApJS, 188, 209

Kwan, J. & Scoville, N. 1974, ApJ, 194, L97

Kwok, S., Purton, C. R., & Fitzgerald, P. M. 1978, ApJ, 219, L125

Lagadec, E., Verhoelst, T., Mekarnia, D., et al. 2011, ArXiv e-prints

Lai, D. 2003, ApJ, 591, L119

Lewis, B. M. 1989, ApJ, 338, 234

Lewis, B. M. 1997, ApJS, 109, 489

Lewis, B. M. 2003, in IAU Symposium, Vol. 209, Planetary Nebulae: Their Evolution and Role in the Universe, ed. S. Kwok, M. Dopita, & R. Sutherland, 71–+

Lewis, B. M., Oppenheimer, B. D., & Daubar, I. J. 2001, ApJ, 548, L77

Likkel, L., Morris, M., & Maddalena, R. J. 1992, A&A, 256, 581

Maeda, T., Imai, H., Omodaka, T., et al. 2008, PASJ, 60, 1057

Manchado, A., Villaver, E., Stanghellini, L., & Guerrero, M. A. 2000, in ASP Series, Vol. 199, Asymmetrical Planetary Nebulae II: From Origins to Microstructures, ed. J. H. Kastner, N. Soker, & S. Rappaport, 17–+

Matt, S., Balick, B., Winglee, R., & Goodson, A. 2000, ApJ, 545, 965

Miranda, L. F., Gómez, Y., Anglada, G., & Torrelles, J. M. 2001, Nature, 414, 284

Modjaz, M., Moran, J. M., Kondratko, P. T., & Greenhill, L. J. 2005, ApJ, 626, 104

Morris, M. 1987, PASP, 99, 1115

Morris, M. R., Sahai, R., & Claussen, M. 2003, in Revista Mexicana de Astronomia y Astrofisica Conference Series, Vol. 15, Revista Mexicana de Astronomia y Astrofisica Conference Series, ed. J. Arthur & W. J. Henney, 20–22

Nakashima, J. & Deguchi, S. 2007, ApJ, 669, 446

Nedoluha, G. E. & Watson, W. D. 1990, ApJ, 361, L53

Nedoluha, G. E. & Watson, W. D. 1994, ApJ, 423, 394

Nordhaus, J. & Blackman, E. G. 2006, MNRAS, 370, 2004

Nordhaus, J., Blackman, E. G., & Frank, A. 2007, MNRAS, 376, 599

Nyman, L., Hall, P. J., & Olofsson, H. 1998, A&AS, 127, 185

Nyman, L., Johansson, L. E. B., & Booth, R. S. 1986, A&A, 160, 352

Paczynski, B. 1976, in IAU Symposium, Vol. 73, Structure and Evolution of Close Binary Systems, ed. P. Eggleton, S. Mitton, & J. Whelan, 75–+

Pardo, J. R., Cernicharo, J., Gonzalez-Alfonso, E., & Bujarrabal, V. 1998, A&A, 329, 219

Pascoli, G. 1987, A&A, 180, 191

Reid, M. J., Haschick, A. D., Burke, B. F., et al. 1980, ApJ, 239, 89

Reid, M. J. & Moran, J. M. 1981, ARA&A, 19, 231

Rudnitski, G. M., Pashchenko, M. I., & Colom, P. 2010, Astronomy Reports, 54, 400

Rudnitskii, G. M. & Chuprikov, A. A. 1990, Soviet Ast., 34, 147

Sahai, R., Morris, M., Sánchez Contreras, C., & Claussen, M. 2007, AJ, 134, 2200

Sahai, R., te Lintel Hekkert, P., Morris, M., Zijlstra, A., & Likkel, L. 1999, ApJ, 514, L115

Sahai, R. & Trauger, J. T. 1998, AJ, 116, 1357

Samus, N. N., Durlevich, O. V., & et al. 2009, VizieR Online Data Catalog, 1, 2025

Sarma, A. P., Troland, T. H., & Romney, J. D. 2001, ApJ, 554, L217

Schwartz, P. R., Harvey, P. M., & Barrett, A. H. 1974, ApJ, 187, 491

Schwarz, H. E., Nyman, L., Seaquist, E. R., & Ivison, R. J. 1995, A&A, 303, 833

Sevenster, M. N. 2002, AJ, 123, 2788

Shintani, M., Imai, H., Ando, K., et al. 2008, PASJ, 60, 1077

Soker, N. 1998, MNRAS, 299, 1242

Soria-Ruiz, R., Alcolea, J., Colomer, F., Bujarrabal, V., & Desmurs, J.-F. 2007, A&A, 468, L1

References

Szymczak, M. & Cohen, R. J. 1997, MNRAS, 288, 945

Szymczak, M., Cohen, R. J., & Richards, A. M. S. 2001, A&A, 371, 1012

te Lintel Hekkert, P., Versteege-Hensel, H. A., Habing, H. J., & Wiertz, M. 1989, A&AS, 78, 399

Terman, J. L. & Taam, R. E. 1996, ApJ, 458, 692

Troland, T. H. & Heiles, C. 1982, ApJ, 252, 179

van der Veen, W. E. C. J. & Habing, H. J. 1988, A&A, 194, 125

Van Langevelde, H. J., van der Heiden, R., & van Schooneveld, C. 1990, A&A, 239, 193

Vlemmings, W., Diamond, P. J., & van Langevelde, H. J. 2001, A&A, 375, L1

Vlemmings, W. H. T. 2008, A&A, 484, 773

Vlemmings, W. H. T. & Diamond, P. J. 2006, ApJ, 648, L59

Vlemmings, W. H. T., Diamond, P. J., & Imai, H. 2006, Nature, 440, 58

Vlemmings, W. H. T., Diamond, P. J., & van Langevelde, H. J. 2002, A&A, 394, 589

Vlemmings, W. H. T., Humphreys, E. M. L., & Franco-Hernández, R. 2011, ApJ, 728, 149

Vlemmings, W. H. T., van Langevelde, H. J., & Diamond, P. J. 2005, A&A, 434, 1029

Walker, R. C. 1984, ApJ, 280, 618

Walsh, A. J., Breen, S. L., Bains, I., & Vlemmings, W. H. T. 2009, MNRAS, 394, L70

Watson, W. D. 2002, in IAU Symposium, Vol. 206, Cosmic Masers: From Proto-Stars to Black Holes, ed. V. Migenes & M. J. Reid, 464–+

Watson, W. D. & Wyld, H. W. 2001, ApJ, 558, L55

Western, L. R. & Watson, W. D. 1983, ApJ, 275, 195

Whitelock, P., Menzies, J., Feast, M., et al. 1994, MNRAS, 267, 711

Wiebe, D. S. & Watson, W. D. 1998, ApJ, 503, L71+

Wilson, T. L., Walmsley, C. M., & Baudry, A. 1990, A&A, 231, 159

Wilson, W. J. & Barrett, A. H. 1972, A&A, 17, 385

Winnberg, A., Nguyen-Quang-Rieu, Johansson, L. E. B., & Goss, W. M. 1975, A&A, 38, 145

Zell, P. & Fix, J. D. 1991, ApJ, 369, 506

Publications

Refereed Papers

1. *The magnetic field of the evolved star W43A* (Chapter 2)
   N. Amiri, W. H. T. Vlemmings, H. J. van Langevelde
   Astronomy & Astrophysics, 2010, 509, 26

2. *The kinematics and magnetic fields in water-fountain sources based on OH maser observations* (Chapter 3)
   N. Amiri, W. H. T. Vlemmings, H. J. van Langevelde
   Astronomy & Astrophysics, 2011, 532, 149

3. *Green Bank Telescope Observations of the H_2O masers of evolved stars: magnetic field and maser polarization* (Chapter 4)
   N. Amiri, W. H. T. Vlemmings, H. J. van Langevelde
   Submitted to Astronomy & Astrophysics

4. *VLBA SiO maser observations of the OH/IR star OH 44.8-2.3: magnetic field and morphology* (Chapter 6)
   N. Amiri, W. H. T. Vlemmings, A. J. Kemball, H. J. van Langevelde
   Accepted for publication in Astronomy & Astrophysics

5. *Rotten Egg Nebula: The magnetic field of a binary evolved star*
   M. L. Leal-Ferreira, W. H. T. Vlemmings, P. J. Diamond, A. Kemball, **N. Amiri**, J. -F. Desmurs.
   Submitted to Astronomy & Astrophysics

Conference Proceedings

1. *Magnetic Fields And Developing Asymmetries in Circumstellar Masers*
   N. Amiri, W. H. T. Vlemmings, H. J. van Langevelde, A. J. Kemball
   Dissertation Talk, American Astronomical Society, AAS Meeting #218, #219.04; Bulletin of the American Astronomical Society, Vol. 43, 2011

2. *W43A: magnetic field and morphology*
   N. Amiri, W. H. T. Vlemmings, H. J. van Langevelde
   Asymmetric Planetary Nebulae 5 conference, held in Bowness-on-Windermere, U.K., 20 - 25 June 2010

3. *The magnetic field of the evolved star W43A*
   N. Amiri, W. H. T. Vlemmings, H. J. van Langevelde
   Cosmic Magnetic Fields: From Planets, to Stars and Galaxies, Proceedings of the
   International Astronomical Union, IAU Symposium, Volume 259, p. 109-110

4. *The magnetic field of the evolved star W43A*
   N. Amiri, W. H. T. Vlemmings, H. J. van Langevelde
   Proceedings of the 9th European VLBI Network Symposium on The role of VLBI in the Golden
   Age for Radio Astronomy and EVN Users Meeting. September 23-26, 2008. Bologna, Italy.

4. *The magnetic field of the evolved star W43A*